NOVEL INTERCALATED NANOCOMPOSITES BASED ON VANADIUM PENTOXIDE XEROGEL AND SODIUM IRON OXIDE

A Thesis

Submitted to the Graduate Faculty

in Partial Fulfillment of the Requirements

for the Degree of Master of Science

Department of Chemistry

Faculty of Science

University of Prince Edward Island

Evans A. Monyoncho

Charlottetown, Prince Edward Island

November 2011

Library and Archives
Canada

Published Heritage
Branch

395 Wellington Street
Ottawa ON K1A 0N4
Canada

Bibliothèque et
Archives Canada

Direction du
Patrimoine de l'édition

395, rue Wellington
Ottawa ON K1A 0N4
Canada

Your file Votre référence
ISBN: 978-0-494-82237-1
Our file Notre référence
ISBN: 978-0-494-82237-1

NOTICE:

The author has granted a non-exclusive license allowing Library and Archives Canada to reproduce, publish, archive, preserve, conserve, communicate to the public by telecommunication or on the Internet, loan, distribute and sell theses worldwide, for commercial or non-commercial purposes, in microform, paper, electronic and/or any other formats.

The author retains copyright ownership and moral rights in this thesis. Neither the thesis nor substantial extracts from it may be printed or otherwise reproduced without the author's permission.

AVIS:

L'auteur a accordé une licence non exclusive permettant à la Bibliothèque et Archives Canada de reproduire, publier, archiver, sauvegarder, conserver, transmettre au public par télécommunication ou par l'Internet, prêter, distribuer et vendre des thèses partout dans le monde, à des fins commerciales ou autres, sur support microforme, papier, électronique et/ou autres formats.

L'auteur conserve la propriété du droit d'auteur et des droits moraux qui protège cette thèse. Ni la thèse ni des extraits substantiels de celle-ci ne doivent être imprimés ou autrement reproduits sans son autorisation.

In compliance with the Canadian Privacy Act some supporting forms may have been removed from this thesis.

While these forms may be included in the document page count, their removal does not represent any loss of content from the thesis.

Conformément à la loi canadienne sur la protection de la vie privée, quelques formulaires secondaires ont été enlevés de cette thèse.

Bien que ces formulaires aient inclus dans la pagination, il n'y aura aucun contenu manquant.

Canada

CONDITIONS FOR THE USE OF THE THESIS

The author has agreed that the Library, University of Prince Edward Island, may make this thesis freely available for inspection. Moreover, the author has agreed that permission for extensive copying of this thesis for scholarly purposes may be granted by the professor or professors who supervised the thesis work recorded herein or, in their absence, by the Chair of the Department or the Dean of the Faculty in which the thesis work was done. It is understood that due recognition will be given to the author of this thesis and to the University of Prince Edward Island in any use of the material in this thesis. Copying or publication or any other use of the thesis for financial gain without approval by the University of Prince Edward Island and the author's written permission is prohibited.

Requests for permission to copy or to make any other use of material in this thesis in whole or in part should be address to:

Chair of the Department of Chemistry
Faculty of Science
University of Prince Edward Island
Charlottetown, P.E.I.
Canada C1A 4P3

SIGNATURE

PAGE(S)

(iii) & (iv)

REMOVED

Abstract

Energy is a vital component of our economies and lifestyle. Unfortunately, most of the current sources of energy are not renewable or environmentally friendly. Among the efforts made to tackle this problem is the development of rechargeable batteries. Rechargeable batteries are transducers that convert chemical energy to electrical energy and vice versa. This project was designed to develop green materials that can be used in lithium/Li-ion batteries. The lithium battery chemistry is currently the most promising battery system because of its superior properties such as high voltage and energy density.

The project involved the successful intercalation of highly ionically conducting polymers Poly(oxymethylene-oxyethylene) (POMOE), Poly[oligo(ethylene glycol) oxalate] (POEGO) and Poly[bis-(methoxyethoxyethoxy)phosphazene] (MEEP) into the layered structure vanadium pentoxide xerogel ($V_2O_5nH_2O$) and the characterization of the resulting nanocomposites. Intercalation of POMOE and POEGO lead to the bilayer loading of the polymer into the gallery spaces of $V_2O_5nH_2O$. This was a significant achievement because the resulting nanocomposites have potential to intercalate more Li-ions compared to monolayer nanocomposites. Intercalation of MEEP into $V_2O_5nH_2O$ leads to nanocomposites whose interlayer expansions increased with increasing concentration of MEEP. The intercalates with higher MEEP concentration were mixed (electronic and ionic) conductors while the intercalates with lower concentration were electronic conductors.

Direct intercalation of the ionically conducting polymers into sodium iron oxide ($NaFeO_2$) was not achieved. However, the projects lead to successful de-intercalation (removal) of Na from $NaFeO_2$ *via* a hydrolysis reaction to produce $Na_{1-x}FeO_2$ (hydrolysis residue) and sodium carbonate hydrate (hydrolysis aqueous solution). The $Na_{1-x}FeO_2$ where $x \approx 1$ had been previously predicted as an ideal alternative electrode material to the currently used $LiCoO_2$ in lithium batteries but had not successfully synthesized. Therefore, this was a major breakthrough in synthesizing this material. The methodology developed here has the advantage of being easily scaled up to industrial production. It was also discovered that the sodium carbonate hydrate had a layered structure and can be intercalated with guest molecules.

The new materials reported here were characterized with powder X-ray diffraction (PXRD), thermogravimetric analysis (TGA), differential scanning calorimetry (DSC), scanning electron microscopy (SEM), Fourier transform infrared (FTIR) spectroscopy, energy-dispersive X-ray spectroscopy (EDS), X-ray photoelectron spectroscopy (XPS) and AC impedance spectroscopy.

Acknowledgments

Many people have played a great role directly and indirectly in ensuring the success of this project, but I would like to mention a few of them. First, I would like to greatly acknowledge my supervisor Dr. Rabin Bissessur for accepting me into his research group. The opportunity he provided me has enabled me to establish a good foundation for my future endeavors. I have gained research experience ranging from designing and implementing experiments, drafting manuscripts, working independently and as a team, to mentoring my juniors.

This research project involved collaboration with Dr. Douglas Dahn at University of Prince Edward Island (Physics department). Dr. Dahn spent many hours working with me while learning conductivity measurements, powder X-ray technique among other discussions. He also served in my supervisory committee. Therefore, I thank Dr. Dahn for his efforts and support. Thanks to Barry Linkletter for serving in my supervisory committee. The feedback, support, and recommendations from my supervisory committee were invaluable.

I thank all chemistry department faculty members for their support during my program. Special thanks to Dr. Christian Lacroix for his support with SEM and Dr. Nola Etkin for the Glove box training and other support as the chair of the department.

I would like thank the chemistry department staff. Dawna Lund welcomed me into this program through safety, NMR, and FTIR training. She was always available to offer support with technical issues. Thanks to Jill MacDonald for her positive discussions and help especially with General chemistry laboratory in which I was one of the instructors. I offer many thanks to Janette Paquet for her administrative assistance in the department.

I would like to thank my fellow graduate and undergraduate students both current and former who were helpful with discussions on various issues, which made my life experience at UPEI both rewarding and enriching. I give special recognition to Adam Proud and his girlfriend Jillian, Iskandar Saada, Victoria Trenton, Matthieu Hughes, and Shiv Veer Singh whom I have worked with side by side.

I acknowledge the infrastructure and financial support from the University of Prince Edward Island. I give special recognition to the Library services and staff that provided me with literature and writing skills that have made my research experience enriching.

Special thanks to my family for their support and patience during my program. I also thank Dr. Bosire Monari Mwebi from St. Francis Xavier who was a major source of encouragement prior to and after joining the program. Above all, I thank God for the life he has given me and for guiding me through many challenges.

Contents

List of Figures

List of Tables

1 Introduction

1.1 Background

Energy is a vital component of our economies and lifestyles. Although there are many forms of energy available, most of them are not directly useful to us. For example, wind and solar energy cannot directly be used to light homes or run equipments like computers, freezers, and fridges without first converting them into electrical energy. Therefore, it is fortunate that energy can be converted from one form to another and even store that energy for future use. Electricity is the only form of energy that can be conveniently utilized to meet our daily needs in homes, businesses, and institutions. Figure 1.1 shows different forms of energy and the conversion relationship to electrical energy.

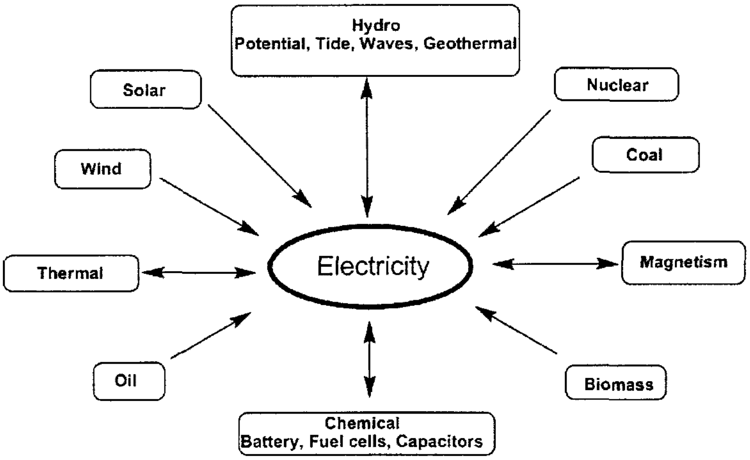

Figure 1.1: Energy sources and conversion relationships. Single and double arrows indicate non-reversible and reversible energy conversion relationships, respectively.

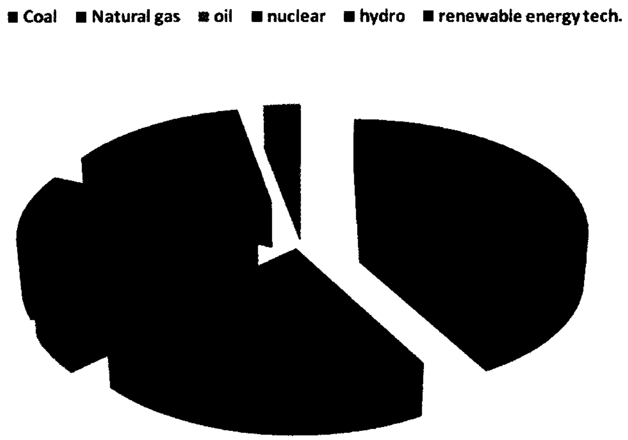

Figure 1.2: Current percentages of electrical energy sources.

The unfortunate reality is that approximately 68% of today's electrical energy is supplied from non renewable fossil fuels.[1] Figure 1.2 shows the percentages of current sources of electrical energy.

With the current high demand for electrical energy, there is need for efficient, renewable, economical, and environmental friendly ways of converting other forms of energy to electrical energy. Potential electrical energy storage (EES) technologies can be classified into two groups, depending on how the electrical energy is stored:1 direct storage or *via* conversion storage as summarized in Figure 1.3.

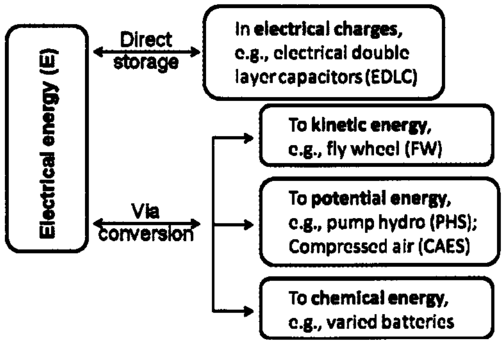

Figure 1.3: Potential electrical energy storage and conversion devices. Reproduced from reference [1].

Rechargeable (secondary) batteries are among the most successfully tried and true technologies that can repeatedly generate clean electricity from stored chemical materials and convert electric energy into chemical energy.[2]

The driving forces behind the increasing demand for rechargeable batteries are very diverse. For example, the emerging 3-Generation (3G) and 4G technologies implemented in cell phones are leading to higher demand for high-power batteries.3 Other driving forces are: i) the expanded use of renewable energy sources, such as electricity generation from solar cells and wind power and ii) the permanent peak and valley load shift program with the "smart/intelligent grids."[1, 4] These demands have motivated scientific and technological efforts dedicated to improving existing rechargeable battery systems to developing new electrode reactions and materials. The attributes for an ideal battery include long life, small size, light weight, high energy density, safety, environmental compatibility, low cost, and worldwide consumer distribution. None of the current rechargeable batteries have all these attributes.

The improvements sought in electrode materials mainly focus on i) larger capacity and higher energy and power density; ii) higher reactivity, reversibility, and structural stability during charge/discharge cycles; iii) faster ionic diffusion and electronic transfer at high discharge/charge rates; iv) lower cost, and v) higher safety features and environmental friendliness.[3, 5] In this thesis the focus will be on developing materials that can be used as electrolyte and/or cathode materials for lithium/Li-ion batteries.

1.2 Batteries

A battery is a transducer that converts chemical energy into electrical energy and vice versa.[6] It contains an anode, a cathode, and an electrolyte. The anode (negative electrode), gives up electrons to the external circuit and is oxidized during the electrochemical reaction. The cathode (positive electrode), accepts electrons from the external circuit and is reduced during the electrochemical reaction. The electrolyte (ionic conductor) provides the medium for the transfer of the charge (ions) inside the cell between the anode and cathode. Figure 1.4 is a schematic showing the battery componets and their working principle.

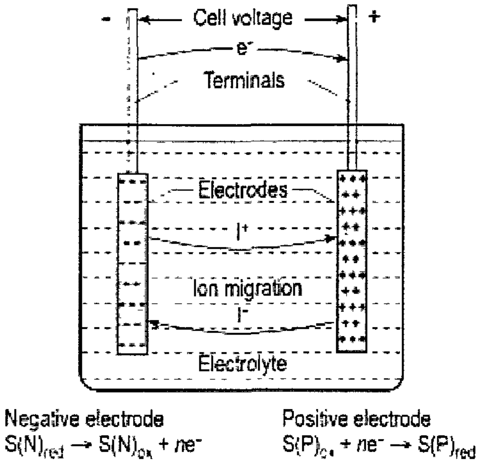

Figure 1.4: Simple schematic showing battery components and operation principle. Reproduced from reference [7].

1.2.1 Battery history and designs

The history[7] of batteries dates back to Luigi Galvani (1737-1798) who detected electrical phenomena between different metals in his famous experiments with frog legs. Allessandro Volta (1745-1827) built the first primary battery, the so-called Volta pile. It was Michael Faraday (1791-1867) who established the scientific foundation of electrochemical energy storage. The early development of secondary batteries is connected to names like Gaston Plant'e (1834-1899), Camille Alfons Faure (1840-1898), and Henry Owen Tudor (1859-1928) in the field of the lead-acid battery, while Thomas Alva Edison (1847-1931) and Valdemar Jungner (1869-1924) are the two important names in connection with nickel-iron and nickel-cadmium batteries. The lead-acid and the nickel-cadmium battery systems have undergone tremendous improvements since then; today's motor cars would be unthinkable without their reliable batteries.

Sealed nickel-cadmium batteries supply the energy for many of our portable electronic devices, and valve-regulated lead-acid batteries have gained a large share of the market for standby batteries. The nickel-metal hydride and the Li-ion battery systems are the new rechargeable systems which have appeared on the market in the last two decades.

The development of the different components of the batteries, such as electrodes and electrolytes leading to different physical designs are summarized in the charts shown in Figure 1.5.

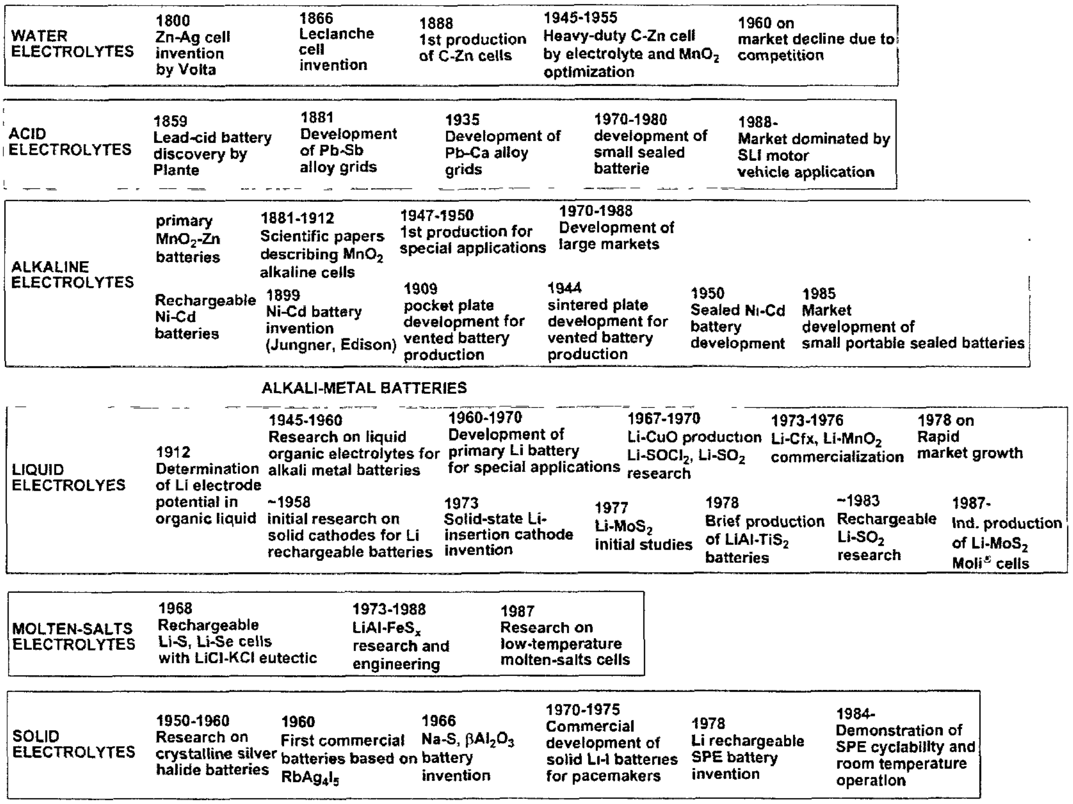

WATER ELECTROLYTES	1800 Zn-Ag cell invention by Volta	1866 Leclanche cell invention	1888 1st production of C-Zn cells	1945-1955 Heavy-duty C-Zn cell by electrolyte and MnO_2 optimization	1960 on market decline due to competition

ACID ELECTROLYTES	1859 Lead-cid battery discovery by Plante	1881 Development of Pb-Sb alloy grids	1935 Development of Pb-Ca alloy grids	1970-1980 development of small sealed batterie	1988- Market dominated by SLI motor vehicle application

ALKALINE ELECTROLYTES	primary MnO_2-Zn batteries	1881-1912 Scientific papers describing MnO_2 alkaline cells	1947-1950 1st production for special applications	1970-1988 Development of large markets		
	Rechargeable Ni-Cd batteries	1899 Ni-Cd battery invention (Jungner, Edison)	1909 pocket plate development for vented battery production	1944 sintered plate development for vented battery production	1950 Sealed Ni-Cd battery development	1985 Market development of small portable sealed batteries

ALKALI-METAL BATTERIES

LIQUID ELECTROLYES	1912 Determination of Li electrode potential in organic liquid	1945-1960 Research on liquid organic electrolytes for alkali metal batteries	1960-1970 Development of primary Li battery for special applications	1967-1970 Li-CuO production $Li-SOCl_2$, $Li-SO_2$ research	1973-1976 Li-Cfx, $Li-MnO_2$ commercialization	1978 on Rapid market growth	
		~1958 initial research on solid cathodes for Li rechargeable batteries	1973 Solid-state Li-insertion cathode invention	1977 $Li-MoS_2$ initial studies	1978 Brief production of $LiAl-TiS_2$ batteries	~1983 Rechargeable $Li-SO_2$ research	1987- Ind. production of $Li-MoS_2$ Moli® cells

MOLTEN-SALTS ELECTROLYTES	1968 Rechargeable Li-S, Li-Se cells with LiCl-KCl eutectic	1973-1988 $LiAl-FeS_x$ research and engineering	1987 Research on low-temperature molten-salts cells

SOLID ELECTROLYTES	1950-1960 Research on crystalline silver halide batteries	1960 First commercial batteries based on $RbAg_4I_5$	1966 Na-S, βAl_2O_3 battery invention	1970-1975 Commercial development of solid Li-I batteries for pacemakers	1978 Li rechargeable SPE battery invention	1984- Demonstration of SPE cyclability and room temperature operation

Figure 1.5: Principle events in the development of primary and secondary batteries. Reproduced from reference [16].

Batteries are broadly grouped into two categories; *primary* (single use) and *Secondary* (rechargeable) depending on their capability of being electrically recycled.

1.2.2 Chemistry

Direct conversion of chemical energy into electrical energy requires the split-up of the electrochemical reactions into reactions of reductants, which deliver electrons, and reactions of oxidants, which accept electrons. The cell reaction characterizes each battery system and its components. The charged and discharged states determine the amount of energy that can be stored. Therefore, the parameters of the cell reaction are of paramount importance for the battery system.[7]

There are several possible battery chemistries but only a few are in the market: lead acid, nickel metal hydride, nickel cadmium, redox flow, sodium sulphur, sodium nickel chloride, and Li-ion batteries.[3, 8] Table 1.1 provides the summary of materials chemistry of the representative rechargeable batteries.

Table 1.1: Summary of material chemistries of the representative rechargeable batteries

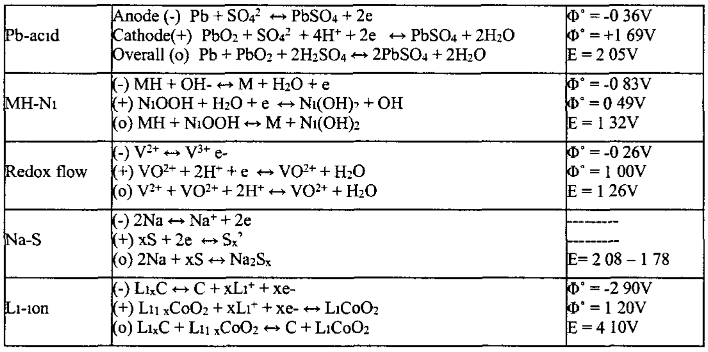

Pb-acid	Anode (-) $Pb + SO_4^{2-} \leftrightarrow PbSO_4 + 2e$ Cathode(+) $PbO_2 + SO_4^{2-} + 4H^+ + 2e \leftrightarrow PbSO_4 + 2H_2O$ Overall (o) $Pb + PbO_2 + 2H_2SO_4 \leftrightarrow 2PbSO_4 + 2H_2O$	$\Phi^\circ = -0.36V$ $\Phi^\circ = +1.69V$ $E = 2.05V$
MH-Ni	(-) $MH + OH^- \leftrightarrow M + H_2O + e$ (+) $NiOOH + H_2O + e \leftrightarrow Ni(OH)_2 + OH$ (o) $MH + NiOOH \leftrightarrow M + Ni(OH)_2$	$\Phi^\circ = -0.83V$ $\Phi^\circ = 0.49V$ $E = 1.32V$
Redox flow	(-) $V^{2+} \leftrightarrow V^{3+}$ e- (+) $VO^{2+} + 2H^+ + e \leftrightarrow VO^{2+} + H_2O$ (o) $V^{2+} + VO^{2+} + 2H^+ \leftrightarrow VO^{2+} + H_2O$	$\Phi^\circ = -0.26V$ $\Phi^\circ = 1.00V$ $E = 1.26V$
Na-S	(-) $2Na \leftrightarrow Na^+ + 2e$ (+) $xS + 2e \leftrightarrow S_x^{2-}$ (o) $2Na + xS \leftrightarrow Na_2S_x$	-------- -------- E= 2.08 – 1.78
Li-ion	(-) $Li_xC \leftrightarrow C + xLi^+ + xe^-$ (+) $Li_{1-x}CoO_2 + xLi^+ + xe^- \leftrightarrow LiCoO_2$ (o) $Li_xC + Li_{1-x}CoO_2 \leftrightarrow C + LiCoO_2$	$\Phi^\circ = -2.90V$ $\Phi^\circ = 1.20V$ $E = 4.10V$

Note: ϕ and E represent standard reduction potential of the half cell and the overall cell at 25 °C

The focus of this work will be on developing functional materials that can be used as electrolyte and/or as cathodes in Li/Li-ion batteries.

1.2.3 Lithium and Li-ion batteries

The beginning of lithium and lithium ion batteries dates back to around 1970 when it was discovered that a range of electron-donating molecules and ions could be intercalated into the layered dichalcogenides, in particular, tantalum disulfide (TaS_2).[9]

Later research expanded to trichalcogenides and related materials to oxides, especially layered oxides. Then Goodenough recognized that $LiCoO_2$ had a structure similar to the layered structures of the dichalcogenides and showed that lithium could be removed electrochemically, thus making it a viable cathode material.[10] The material was commercialized by SONY in 1990s by combining the $LiCoO_2$ cathode and a carbon anode to make the first successful Li-ion battery.6 Since then, there has been continued research to improve the Li-ion batteries and/or replace the toxic and expensive cobalt with less expensive and environmentally friendly materials.

The basic design of the Li-ion battery consists of a cathode and an anode with an open crystalline structure capable of repeatedly intercalating Li-ions, and a high-stability electrolyte and separator. The separator is typically a thin (15 μm) microporous polypropylene film. It prevents the electrodes from shorting directly or through lithium micro dendrite growth on overcharge. The separator also serves as thermal shut-down safety device. When heated above 150 °C (due to internal short circuit in a cell) the separator melts and its pores close, thus preventing current flow and thermal runaway.[11] A Li-ion battery uses an aprotic (no mobile hydrogen atoms) electrolyte, because the high cell voltage of the battery (4.2 V) exceeds the water stability region on both the cathode and the anode side.

The focus for lithium batteries research has been on insertion compounds as cathode materials and carbon or carbon-buffered alloys, or oxides as anode materials.[6] The focus of this work is on the development of intercalation nanocomposite materials that can be used as cathodes and/or electrolytes.

Cathodes

The following are the requirements for a material to be used as a cathode for Li-ion batteries.[6, 13] The material should contain a readily reducible/oxidizable transition metal ion in addition to these requirements.

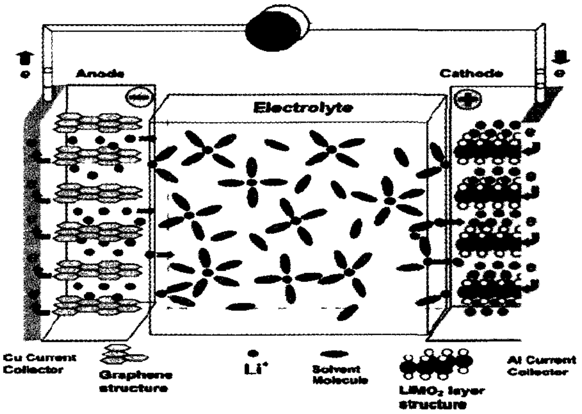

Figure 1.6: Li-ion battery components and operation principle. On discharge, oxidation of Li takes place in the anode releasing electrons, which travel through external load (A) and reduction of the Li-ions takes place in the cathode after traveling from the anode *via* the electrolyte. Reproduced from reference [12]

a) The material reacts with lithium in a reversible manner. This dictates an intercalation-type of reaction in which the host structure essentially does not change as lithium is intercalated and de-intercalated.

b) The material reacts with lithium with a high free energy of reaction.

c) The material reacts with lithium very rapidly on both intercalation and de-intercalation.

d) The material is a good electronic conductor, preferably metallic. This allows for the easy addition or removal of electrons during the electrochemical reaction. Electronic conductivity allows the reactions at all contact points between the cathode active material and the electrolyte rather than at ternary contact points between the cathode active material and the electronic conductor. Carbon black is usually used as an additive for electronic conductivity. It also minimizes the need for inactive conductive diluents, which takes away from the overall energy density.

e) The material is stable, (i.e. it does not change structurally or otherwise degrade, to over-discharge and overcharge).

f) The material has high diffusivity of Li-ions in the structure.

g) The material is insoluble in common electrolytes.

h) The material is cheap.

i) The material is environmentally benign.

There are two groups of cathode materials.[6] The first group contains layered compounds with an anion close-packed or almost close-packed lattice in which alternate layers between the anion sheets are occupied by a redox-active transition metal and Li-ion will insert itself into the essentially empty remaining layers. The cathode materials in the second group have open structures such as vanadium oxides; the tunnel compounds of manganese dioxide and transition-metal phosphates (e.g. the olivine $LiFePO_4$).

Electrolytes

The most typical electrolyte functional groups are ether (-O-), sulfide (-S-), amino (-N<), phosphino (-P<), carbonyl (>C=O), and cyano (-C≡N) groups. This is because of their lone pair of electrons available for solvating cations.[14] There are several classes of electrolytes (e.g. polymers,[15, 16] polymer composites,[17, 18] hybrids,[19, 20] gels,[21] ionic liquids,[22, 23] and ceramics/inorganic solids [24]).

The history on how polymers came into the spot light as alternative electrolytes was initiated by a series of events. In 1975, Peter V. Wright, a polymer chemist from Sheffield, first showed that polyethylene oxide (PEO) can act as a host for sodium and potassium salts, thus producing a solid electrical conductor (polymer/salt complex).[25] Then Michael Armand, who had suggested the use of graphite intercalation compounds for electrodes, immediately realized that lithium/PEO complexes could be deployed as solid electrolytes, matching perfectly with intercalation electrodes. A lithium salt could be dissolved in a solvating polymer matrix through direct interaction of the cation and electron pairs. The complex formed (because of the favorable competition between the solvation energy and the lattice energy of the salt) becomes a good conductor at 60-80 °C. Armand's suggestion met with considerable interest at the Second International Meeting on Solid Electrolytes held at St Andrews in Scotland 1978.[26] The short paper he published opened up new perspectives in the international solid-state ionic's community we see today.

Good solid polymer electrolytes (SPE) should have the following properties: i) good physical mechanical properties and high ionic conductivity (10^{-4} to 10^{-3} Scm^{-1}); ii) low electronic conductivity. iii) operate in the temperature range of -40 to 70 °C; iv) wide range of electrochemical stability (between potentials of 0.0 V to $>$ 4.0 V verses $\mathrm{Li}^{+}/\mathrm{Li}$); v) inert or not dissolve electrode materials and their intercalation products; vi) non-flammable, non-volatile, and non-toxic.[15, 17, 18, 27]

From here on the focus will be on the intercalation chemistry of selected layered structures and ionically conducting polymers.

1.3 Intercalation Chemistry

Intercalation chemistry is a versatile technique for synthesizing new materials at moderate conditions, which cannot be achieved through conventional synthesis, such as solid state synthesis. Intercalation chemistry is an important technique because layered nanomaterials containing both inorganic and organic components can be synthesized and their properties tuned accordingly.[28, 29] By definition, intercalation chemistry is the insertion of guest molecules or ions into the host material, which is normally a layered structure, while maintaining most of the original structural integrity of the host.[28] An interesting feature of intercalation reactions is that the guest and host experience some degree of perturbation along a spectrum from subtle to extreme in their geometric, chemical, electronic, and optical properties.[30] A typical intercalation reaction mechanism for intercalating polymers into layered structures reported here is shown in Figure 1.7.

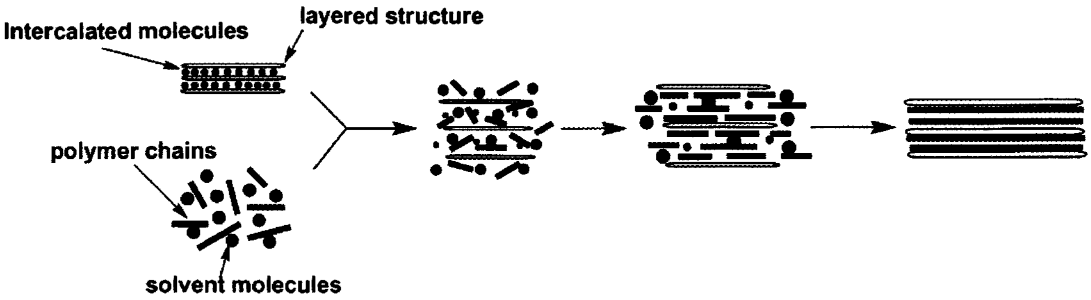

Figure 1.7: Schematic showing the intercalation reaction mechanism. The horizontal arrow indicates time progression of the reaction.

1.4 Layered metal oxides

Layered materials with specific architecture and novel properties continue to receive increasing attention for both scientific and technological interests.[31] This is because layered materials provide the opportunity to tune the interlayer composition through intercalation chemistry leading to the development of new materials with diverse applications. The layered structures under consideration in this work are vanadium pentoxide xerogel and sodium iron oxide.

1.4.1 Vanadium pentoxide xerogel($V_2O_5nH_2O$)

Vanadium pentoxide xerogel[1] ($V_2O_5nH_2O$) is a layered material that continues to receive researchers' attention because its nanocomposites have various potential applications, such as in electrochemical energy storage devices[1, 32], biosensors[33], and electrochromic devices.[34] $V_2O_5nH_2O$ is a good candidate for developing nanocomposites because of its versatile intercalation properties. This is because V_2O_5 ribbons are linked together *via* hydrogen bonded water molecules, and the basal distance (i.e. the distance between two layers) is quite large and interactions between ribbons are much weaker than in crystalline V_2O_5.[35] Intercalation may occur *via* dipole-dipole interaction, ion-exchange, acid-base, coordination, and redox reactions enabling the

---

[1] Xerogel is the solid formed from a gel after slow evaporation of water at room temperature

system to accept both neutral and charged guest species.[36,37] $V_2O_5nH_2O$ has also shown promising redox reactions that can be utilized in Li-ion batteries. For example, Passerini *et al.* demonstrated that $V_2O_5nH_2O$ could be used as a cathode material that reversibly intercalates more than 3 equivalents of lithium.[38] However, the presence of intercalated water molecules in $V_2O_5nH_2O$ is of considerable concern because of their parasitic reaction with the anode for lithium based batteries.[39] Therefore, replacing water molecules with ionically conducting polymers would improve the safety of lithium batteries employing a vanadium oxide cathode. Inclusion of ionically conducting polymers would also help maintain the structural integrity of the vanadium oxide framework and promote the facile movement of Li-ions through the interlayer spaces.

Vanadium pentoxide gels were first reported by Ditte in 1885.[40] Since then, several synthetic methodologies have been reported and reviewed.[41] Ditte heated ammonium vanadate in a platinum crucible, then reacted the residue with hot nitric acid and poured the mixture into water, which lead to the formation of a dark red gel ($V_2O_5nH_2O$). Biltz did a similar experiment using hydrochloric acid.[42] Wegelin reported the synthesis of the gel through thermo-hydrolysis of aqueous solutions of $VOCl_3$.[43] The hydrolysis and condensation processes of vanadium alkoxides $VO(OR)_3$ (R=Et, n-Bu, t-Am,n-Pr, i-Pr) was reported in 1913.[44] The synthesis of the gel by the reaction of hydrogen peroxide with crystalline V_2O_5 (a vigorous reaction) was reported by Ostermann *et al.* [45] The synthesis of the gel by pouring molten V_2O_5 (heated to around 800°C) into water (a method used by industries to prepare large scale quantities) was reported in 1911.[46] The hydration of amorphous V_2O_5 (obtained by splat-cooling) also leads to the formation of vanadium pentoxide gels as reported by Gharbi *et al.* [47]

The most commonly used synthetic methods in the laboratory are protonation of vanadates in aqueous solutions and hydrolysis of vanadate alkoxides.[41] Protonation is usually performed by adding an acid to an aqueous solution of vanadate salts.[40,42] This is better performed through a proton exchange resin so that the counter anions or cations are removed from the solution. Therefore, this method was adapted for the materials reported in this work. The sodium metavanadate aqueous solution ($NaVO_{3(aq)}$) was passed through the acidic resin ($RSO\text{-}H_{(s)}$) . A pale yellow clear solution of polyvanadic acid ($HVO_{3(aq)}$) was obtained. The polyvanadic acid spontaneously polymerized as the excess water was evaporated at room temperature. The polymerized material was a viscous dark red gel.[48,49] The synthetic reaction can be summarized as follows

$$RSO\text{-}H_{(s)} + NaVO_{3(aq)} \rightarrow HVO_{3(aq)} + RSONa_{(s)}.$$

Structure

The structure of vanadium pentoxide xerogels ($V_2O_5nH_2O$) was determined by Petkov *et al.* [50] They used atomic Pair Distribution Function (PDF) analysis of X-ray scattering data for $V_2O_5nH_2O$ xerogel. The structure of the xerogel consists of bilayers (slabs) of V_2O_5 stacked along the c-axis of a monoclinic unit cell composed of square pyramidal VO_5 units. These slabs are separated by water molecules and stack along the z-axis of a monoclinic unit cell (space group *C2/m*, a =11.722(3) Å, b = 3.570(3) Å, c = 11.520(3) Å, and β = 88.65°).

The oxygen coordination of V atoms in $V_2O_5nH_2O$ is similar to that in crystalline V_2O_5. The coordination of V and O atoms resemble a square pyramid with four oxygens at distances between 1.79Åto 2.10 Å making the base of the pyramid and an oxygen atom at $\sim$ 1.6 Å capping the pyramid. The latter coordination is due to a V=O double bond, the existence of which is confirmed from infrared spectroscopy. The structure of $V_2O_5nH_2O$ is shown in Figure 1.8.

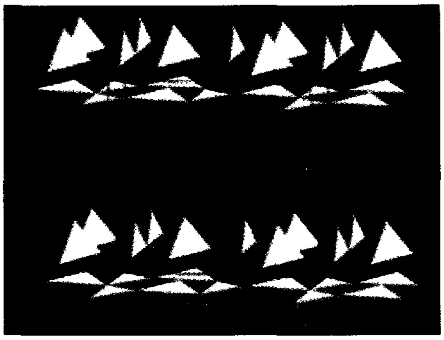

Figure 1.8: Structure of vanadium pentoxide xerogel. The yellow pyramids represent V and O coordination where Os are at the apexes and V is body centered. The blues spheres in the green plane represent the intercalated water molecules. Reproduced with permission from (ACS) see paper 4 caption information

1.4.2 Sodium iron oxide

Iron has been considered a great potential metal for battery applications because it is cheap and non toxic. The layered $Na_{1-x}FeO_2$ containing cheap iron instead of cobalt has been proposed as an ideal alternative electrode material for secondary batteries.[51]

Iron oxide is mainly synthesized through solid state reactions.[51-53] Takeda *et al.* synthesized $NaFeO_2$ based on different starting materials: α-Fe_2O_3, γ-Fe_2O_3, Na_2CO_3 and Na_2O_2. Alternative synthesis technique using iron powder and sodium hydroxide solution has also been reported.[54, 55] The synthetic reaction can be summarized as follows

$$Fe_2O_{3(s)} + Na_2O_{2(s)} \xrightarrow{700^oC} NaFeO_{2(s)}.$$

Structure

It is well known that the compound $NaFeO_2$ has different structural modifications, called α, β and γ.[52] The rhombohedra structure of α-$NaFeO_2$ (space group: $R-3m(166)$, a = 3.0221 Å, b = 3.0221 Å, c = 16.0817 Å, $\alpha = \beta = 90°$ and $\gamma = 120°$ ICDD card No. 82-1495)) is based on hexagonal cubic closest packed oxygen layers in which Fe and Na ions are located in octahedral holes. Fe layers are separated by O^{2-}

- Na^+ - O^{2-} sandwiches. β-$NaFeO_2$ has a wrutzite-like structure, where oxygens form hexagonal closest packing and both Fe and Na ions occupy a half of tetrahedral sites randomly. γ-$NaFeO_2$ has almost the same structure as β-$NaFeO_2$, but the symmetry is raised to tetragonal from orthorhombic. However, its detailed crystal structure is not yet known because of the reversible transition between β- and γ-$NaFeO_2$. Figure 1.9 is the general crystal structure for the layered structure of alkali transition metal oxides AMO_2 (A = Na, K, Li and M = Fe, Co etc) which represents α-$NaFeO_2$.

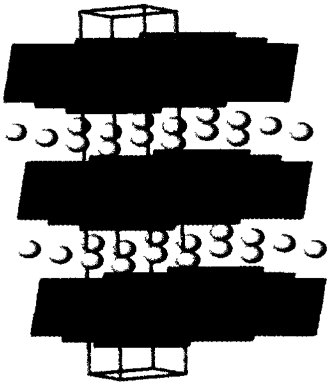

Figure 1.9: Crystal structure for α-$NaFeO_2$.The blue cubes represent the cubic closest packed O layers with Fe in the octahedral holes and the yellow spheres represent intercalated Na. The unit cell is rhombohedra (not shown in the picture). Reproduced from reference [6].

1.5 Ionically conducting polymers

The discovery of ionic conductivity in complexes of poly(ethylene oxide) (PEO) containing alkali metal salts[56] and the suggestion that such ionic conductors could be used as polymer electrolytes in electrochemical devices by Armand *et al.* in 1978 has triggered a lot of research and development in ionically conducting polymers. The ion transport in these polymers is generally agreed to be by segmental motion shown in Figure 1.10. This calls for the host polymers to be flexible, amorphous and with low glass transition temperature.[57] Many polymers have been designed to optimize these properties and improve the ionic conductivity.

1.5.1 Approaches used to improve ionic conductivity

The following strategies have been used to improve ionic conductivity of PEO. The first approach was the incorporation of propylene oxide (PO) units into PEO backbone.[16] While crystallization was suppressed, the Li-ion conductivity was not substantially improved. It was thought that the nonpolar methyl groups reduced the solubility of Li-ions in the polyelectrolyte and thus the mobile charge carriers.[15]

The second approach proposed is the grafting of oligo(ethylene oxide) units to other flexible polymers, resulting in comb-branched type architectures that will solvate Li-ions.[15,58] The swelling of polyether polymers with small polar molecules such as propylene carbonate has also been proposed.[16,59] While effective at improving ionic conductivity, these gel-type systems still exhibit safety issues related to the leakage of liquid additives.

Another proposed approach, is the synthesis of hyperbrached PEO polymers (*hb*PEO).[60] Lee *et al.* [61] reported a study of Li-ion conductivity and its correlation with the polymer segmental dynamics of these hyperbranched PEO by varying the branch content. They showed that polar glycerol moiety of ca. 8 mol% effectively prevents crystallization in blends with Li-salts and leads to approximately a 100-fold increase in the Li-ion conductivity below 50°C in comparison with linear PEO. However, the Li-ion conductivity decreases in these melts due to the development of hydrogen-bonded network, which lowers the molecular dynamics.

A final, yet another important approach is to increase ionic dissociation by placing polar subunits such as acrylamide, acrylonitrile, maleic anhydride, and carbonate along the chains to increase the polymer host dielectric constant.[62,63]

1.5.2 Li-ion transport mechanism in PEO electrolytes

The hopping mechanism for Li-ion transport was first suggested by Grotthus.[64] In this proposal, it is suggested that Li-ions move through PEO from one associated site to the next *via* a catch-and-release process. The association/dissociation of Li-ion is accomplished by the PEO segments. Therefore, the mechanism is strongly coupled to the segmental reorganization dynamics of the polymer involving the Li-ion. Strong evidence that the transport of Li-ions indeed is closely coupled to the local segmental dynamics of polymer chains was provided by Lee *et al.* [61] They demonstrated that one should be able to increase the Li-ion conductivity of polymer electrolytes by enabling faster segmental dynamics. Figure 1.10 illustrates the Li-ion conduction mechanism in PEO electrolytes.

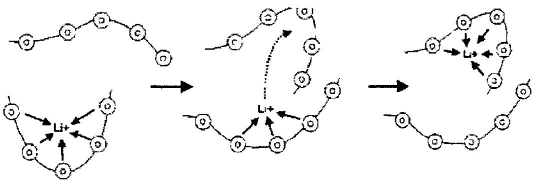

Figure 1.10: Mechanism of Li-ion conduction in PEO electrolytes. The circles represent the ether oxygens of PEO. Reproduced from reference[65].

1.5.3 Poly(oxymethylene-oxyethylene) (POMOE)

POMOE was designed on the premise of reducing crystallinity of poly(oxyethylene) by inserting a methylene group between the oxyethylene sequences leading to increased ionic conductivity.[66] The reduction of crystallinity is essential because crystal boundaries are known to hinder charge transport. The synthesis and structure of POMOE are shown in the reaction schematic in Figure 1.11.

$$\mathrm{2KOH_{(s)} + HO(CH_2CH_2O)_9H \rightarrow KO(CH_2CH_2O)_9K + 2\ H_2O}$$

$$\mathrm{KO(CH_2CH_2O)_9K + nCH_2Cl_2 \rightarrow [(OCH_2CH_2)_9OCH_2]}_n \mathrm{+ 2nKCl}$$

Significant work has been done in our group aimed at improving the mechanical properties of POMOE through intercalation into layered structures. For example, POMOE has been successfully intercalated into molybdenum disulfide (MoS_2)[67,68],

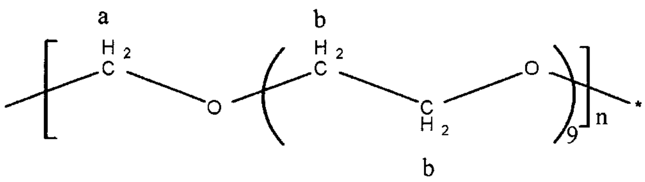

Figure 1.11: Synthetic reaction and structure of POMOE where n is degree of polymerization.

graphite oxide (GO)[69], hectorite[70], tin disulfide (SnS_2)[72], and molybdenum diselenide ($MoSe_2$).[71]

1.5.4 Poly[oligo(ethylene glycol)oxalate](POEGO)

POEGO was developed based on the last approach mentioned above. In POEGO, an oxalate group was introduced into the poly(ethylene glycol) chain by the reaction between poly(ethylene glycol) and oxalic acid.[57] The schematic in Figure 1.12 shows the synthetic reaction and structure of POEGO.

$$mHO\text{-}(CH_2CH_2O)_n\text{-}H + mHOOCCOOH \rightarrow \text{-}[COCO\text{-}(OCH_2CH_2)_n\text{-}O\text{-}]_m\text{-} + 2mH_2O$$

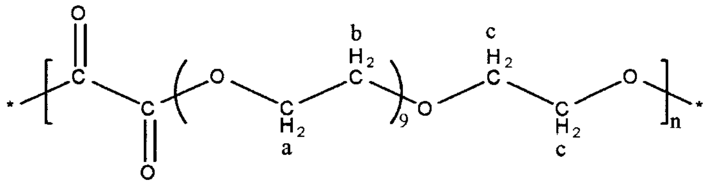

Figure 1.12: Synthetic reaction and structure of POEGO where n is the degree of polymerization.

In previous work, POEGO has been successfully intercalated into molybdenum disulfide (MoS_2)[67], hectorite[70], graphite oxide (GO)[69], and tin disulfide (SnS_2).[72]

1.5.5 Poly[bis-(2-methoxyethoxyethoxy)phosphazene](MEEP)

The motivation behind the development MEEP was the ability to readily convert the poly(dichlorophosphazene) precursor to ionically conductive polymers (stable alkoxy derivatives) *via* nucleophilic substitution reactions. An aliphatic or aromatic R group in RONa can be produced by reacting R-OH with Na metal. The schematic in Figure 1.13 shows the synthetic reaction pathway and structure of MEEP.

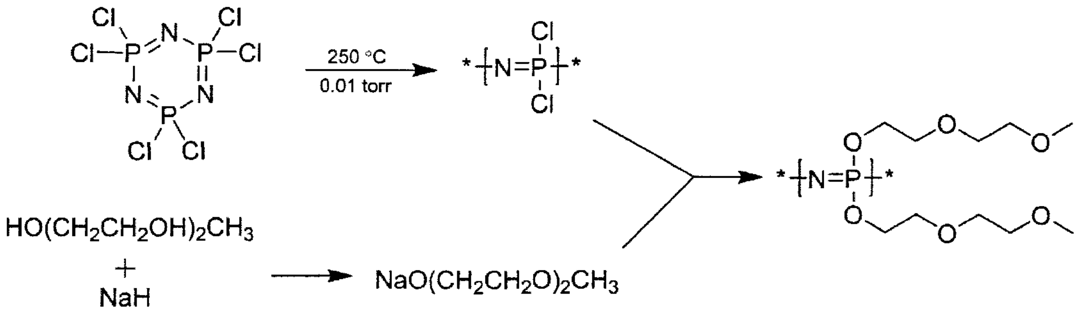

Figure 1.13: Synthetic reaction and structure of MEEP

A lot of research is being done to improve the mechanical stability of MEEP to facilitate its application in Li-ion batteries. For example, the polymer has been exposed to gamma[73] and UV[74] radiations, which result in cross-linked MEEP. Layer by layer (LbL) assembly method to create homogeneous blends of MEEP (as a hydrogen bonding acceptor) and poly(acrylic acid) (PAA) (as a hydrogen-bonding donor) resulting into controlled film growth with high ionic conductivity and excellent hydrolytic stability has been reported.[75] Chemical vapor deposition of MEEP films as an alternative to solution casting to get films with good adhesion to the substrate has been attempted.[76] Blending MEEP with other PEO based polymers has been explored.[77] None of these techniques have been successful but they have increased the fundamental understanding of the MEEP system. One of the current promising and versatile technique of enhancing the mechanical properties of MEEP is *via* intercalation into layered structures. For example, successful intercalation of MEEP into molybdenum disulfide (MoS_2)[67], hectorite[70], tin disulfide (SnS_2)[72], molybdenum diselenide ($MoSe_2$)[71] and graphite oxide (GO)[78] have been reported.

1.6 Objectives of this research project

The project objectives were to build on and extend knowledge of intercalating highly ionically conducting polymers (POMOE, POEGO, and MEEP) into the layered structures ($V_2O_5nH_2O$ and $NaFeO_2$) and to characterize the resulting nanocomposites. The successful intercalation of polymers into layered structures will be investigated by powder X-ray diffraction technique (PXRD). Thermal stability and phase transitions of the new materials will be studied by Thermogravimetric analysis (TGA) and differential scanning calorimetry (DSC), respectively. Fourier transform infrared (FTIR) spectroscopy will be used to study the nature of chemical bonds in the nanocomposites in comparison to pure polymers and pristine layered structures. Elemental analysis of the materials will be done using energy-dispersive X-ray spectroscopy (EDS) and X-ray photoelectron spectroscopy (XPS). Scanning electron microscopy (SEM) will be used to look at the morphology of the new materials. Impedance spectroscopy will be used to determine the conductivity (electrical or ionic) properties of the new materials. The new materials will be evaluated for their potential to be used in lithium/Li-ion battery based on their structural and conductivity properties.

2 Characterization Techniques

2.1 Powder X-ray Diffraction (PXRD)

Powder X-ray diffraction is an important tool in materials characterization especially if they are crystalline. What is observed in X-ray diffraction is the interaction of the electromagnetic waves with the atoms of the crystal. When X-rays pass through a crystal, each atom in the structure scatters the waves uniformly in space. The interference of all these scattered waves in large crystals leads to extinction in most of the directions (destructive interference) because for every wave scattered a second wave in the crystal exists with a phase shift of $\lambda/2(\lambda$ = wave length). Only in certain directions do all the waves combine in an additive manner (optimal), leading to enhanced intensity (constructive interference).These directions are related to the distances between atomic planes (the d-values) and the angle θ of the sample plane at which the X-rays enter and leave a crystal.[79] The relationship for the wavelength of X-rays used, the d-values, and the angle of incident/reflection can be described by the Bragg equation:

$$n\lambda = 2dsin\theta \tag{2.1}$$

where λ = wavelength of the X-ray used, θ = angle of the sample substrate plane at which the X-rays strike the crystal and for which the maximum interference intensity is observed, d = distance between the set of *hkl* planes in the crystal (lattice spacing's) and n = order of the reflection.

The X-ray diffraction pattern of a sample is a plot of the observed diffracted intensity against 2θ, where θ is the Bragg angle. From this pattern, the d-values are calculated. Usually the X-ray diffraction pattern is recorded as a diffractogram using a goniometer equipped with a proportional/scintillation counter and a registration unit.

The diffraction pattern provides important information. The information is used for sample identification, purity/quality control, crystallite size calculations, and determination of structural parameters (unit cell and dimensions) of the material. For illustration, the peak positions are used for sample identification, the peak intensities are used for quantification, and the peak widths are used to determine crystallite size and strain. Structural parameters are obtained from the unit cell edge lengths after fitting followed with correction of the peak position using peaks of internal standard. Finally, and most important information from the diffraction pattern especially in this work is the peak shift. The peak shift, provides information about the isomorphism substitution or intercalation of guest molecules into a layered structure.

2.1.1 Instrumentation

A powder X-ray diffractometer consists of an X-ray source (X-ray tube). a sample stage, a detector, and a mechanism to vary the angle θ. The X-ray radiation is focused on the sample at some angle θ while the detector opposite the source reads the intensity of the X-rays it receives at 2θ away from the source path. The incident angle is then increased over time while the detector angle always remains 2θ above the source path as shown in Figure 2.1.

Crystallite size determination is one of the most important applications in powder diffractometry for materials characterization.[80] Unfortunately, it cannot be measured directly. Furthermore, there is enormous confusion in literature concerning the definition of particle size, crystal size, and domain size. A particle (secondary grain) may consist of one or more crystals (primary grain). Particle size is not accessible

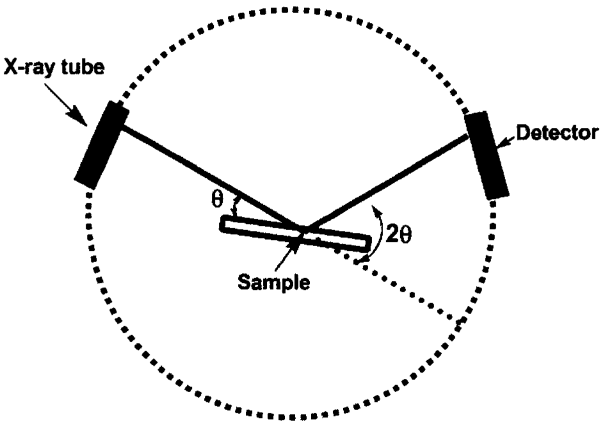

Figure 2.1: PXRD schematic showing the main components and the working principle. A monochromatic X-ray enters the sample at angle θ and reflects and the intensity is detected by a detector positioned at 2θ from substrate plane

by powder diffraction but by light microscopy, laser size analysis, sieving and other techniques. Similarly, crystal size is not accessible by powder diffraction. The agglomeration effects can also hamper crystal size analysis by particle size techniques. Each crystal may contain one or more crystallites. Hence, the crystallite size is in general equal or less than the crystal size. Each crystallite may consist of one or more coherently reflecting domains, which need not to be connected. Figure 2.2 shows the shapes representing this terminologies.

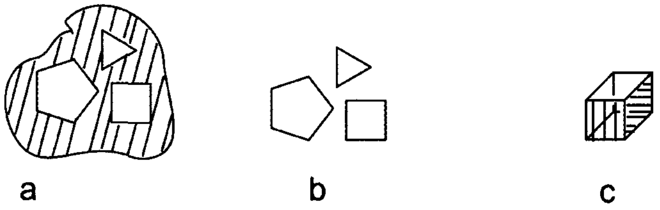

Figure 2.2: Schematic representation of terms a) particle or grain size, b) crystal size, and c) crystallite size.

The crystallite size is determined by means of powder diffraction technique using Scherrer equation. The Scherrer equation is

$$D_{hkl} = \frac{K\lambda 57.3}{\beta \cos\theta} \tag{2.2}$$

where D_{hkl} = average crystallite size (Å), λ = the wavelength of the Cu (Kα) radiation used (λ=1.524 Å), β = peak width at half-height (2θ) and θ = position of the peak in degrees. The constant 57.3, is the conversion factor from radians to degrees. K is a constant depending on the shape of the crystallites. The crystallite shape of these materials is not known but because the primary interest is in trends, not the actual values, K = 0.9 (for spheres) is used for all samples.

2.2 Nuclear Magnetic Resonance (NMR) Spectroscopy

NMR is a powerful tool, which allows chemists to determine the structure of molecules based on the absorption of energy by magnetic nuclei such as ^{1}H, ^{13}C, ^{19}F, and ^{31}P. The important features of an NMR spectrum are the *chemical shifts*, *peak area* (integration curves), and *signal splitting*. The working principle of NMR is based on the fact that the nuclei of certain elements (^{1}H, ^{13}C, ^{19}F, and ^{31}P) and isotopes behave as though they were magnets spinning about an axis.[81] When compounds containing such atoms are placed in a very strong magnetic field and simultaneously irradiated with electromagnetic energy, the magnetic nuclei absorb energy through a process called *magnetic resonance*. Magnetic resonance is quantized and produces characteristic spectrum for the compound. The absorption of the energy does not occur unless the magnetic field and the frequency of the electromagnetic radiation match. The actual field strength at which absorption occur (chemical shift) is highly dependent on the magnetic environment of each atom. The two factors, which determine this magnetic environment, are the magnetic fields generated by circulating electrons, and the magnetic fields that result from the nearby atoms (or other magnetic nuclei).

The main value of NMR spectroscopy (especially ^{13}C and ^{1}H) lies in the provision of information on skeletal structure (e.g. aliphatic straight or branched chain, aromatic, heterocyclic). The confirmatory evidence on the nature of the functional group is deduced from the consideration of the chemical shift values and from the definitive information in the case of groups having replaceable hydrogens or groups with highly de-shielded protons.[82] The chemical shifts (the peak position in an NMR spectrum), are measured along the bottom of the spectrum on a delta (δ) scale as a fraction of un-shifted frequency $(\omega - \omega_o)/\omega_o = 10^{-6}$, where ω is the angular frequency and 10^{-6} = parts per million (ppm) units. The peak areas are important in assigning signals to particular groups of hydrogen atoms and are automatically measured by the instrument and plotted as the integral curves over each signal. These areas are in the same ratio as the number of hydrogen atoms causing each signal. Therefore, the heights of the integral curves are proportional to the areas under the signal. Signal splitting is a phenomenon that arises from magnetic influence of hydrogens on adjacent atoms to those bearing the hydrogen atoms causing the signal being considered. Signal splitting provides important information about the structure of the compound.

2.3 Fourier Transform Infrared(FTIR) Spectroscopy

Infrared spectroscopy is the study of how compounds absorb infrared radiation and the structural information obtained from the resulting spectrum of those compounds. Different types of bonds in the compound absorb different frequencies of radiation as the bonds stretch and bend. Through Fourier transform the instrument produces a spectrum that plots the amount of infrared radiation absorbed by the sample as a function of frequency, usually expressed as wavenumbers (cm^{-1}). An infrared spectrum of a compound is very much like a fingerprint of a molecule. If the structure of the molecule is already known or partially known, then the spectrum can be predicted before running the scan and working backwards.

The main value of infrared spectra features is the detection of functional groups (chemical bonds), although the information on skeletal structure can also be obtained. For example, infrared spectra can be used to distinguish between functional isomers, such as alcohols and ethers, or aromatic and aliphatic compounds.[82] It is important to note that the absence of an absorption band can often provide more information about the structure of a compound than its presence. Therefore, care should be taken to avoid focusing on selected absorption bands and overlooking others.

2.4 Thermal Analysis

Thermal analysis is a group of techniques in which a property of the sample is monitored against time or temperature while the temperature of the sample, in a specified atmosphere, is programmed. The program may involve heating or cooling at a fixed (or variable) rate of temperature change, holding the temperature constant, or any sequence of these.[83]

2.4.1 Thermogravimetric Analysis (TGA)

In TGA, the sample mass is recorded continuously in a controlled atmosphere as a function of temperature or time. Usually, the temperature of the sample is increased linearly with time.[84] The plot obtained is called a thermogram or a thermal decomposition curve. Because TGA monitors the mass of the analyte with temperature, the information provided is quantitative, but limited to the decomposition and oxidation reactions and to such physical processes as vaporization, sublimation, and desorption.

TGA offers potential for characterizing thermal stability and stoichiometric composition of materials. The stoichiometry of a sample can be calculated using TGA given that three conditions are met: a) the starting weight of the sample, b) the identity of each mass loss and c) the final phase are known.

2.4.2 Differential scanning calorimetry (DSC)

DSC is a technique used to study what happens to samples when they are heated/cooled (i.e. thermal phase transitions). Therefore, DSC helps to evaluate exothermic and endothermic events that occur to the sample usually in the temperature range of -180 °C to 725 °C. Thermal phase transitions include glass transition, crystallization, melting, and decomposition.

Instrumentation

There are three types of DSC instruments: *power-compensated DSC, heat-flux DSC, and modulated DSC.*[83,84] For this work *heat-flux* DSC system was used. In heat-flux DSC the sample and reference cells are heated at the same rate to maintain the same temperature (horizontal baseline). When the phase transition takes place in the sample, the temperature of the sample changes by laging behind (endothermic transition) or shooting higher (exothermic transition). To maintain the same temperature during the phase transition, the computer is programmed to provide the extra heat required (for endothermic phase transition) or take away the extra heat produced (exothermic phase transition) from the sample. This differential heat flow is measured and recorded. The phase transitions are obtained from the baseline changes of the plot, which represents the phase transitions taking place in the sample. Figure 2.3 shows a schematic and operating principle of heat-flux DSC. There are two pans: the sample pan and the reference pan. Each pan sits on top of a heater. The computer is programmed to heat the pans at a specific heating rate.

The general equation that describes the resultant heat flow at any point in a DSC experiment is

$$\frac{dQ}{dt} = C_p\beta + f(T,t) \tag{2.3}$$

where dQ/dt = total heat flow, C_p= specific heat capacity ($JK^{-1}mol^{-1}$), β = heating rate, and $f(T,t)$ = heat flow from kinetic (absolute temperature and time dependent) processes ($Jmol^{-1}$). Note that there are two component of the total heat flow: i) reversing heat flow, $C_p\beta$, which is a function of the sample's heat capacity and rate of temperature change and ii) non-reversing heat flow, $f(T,t)$ which is a function of absolute temperature and time.

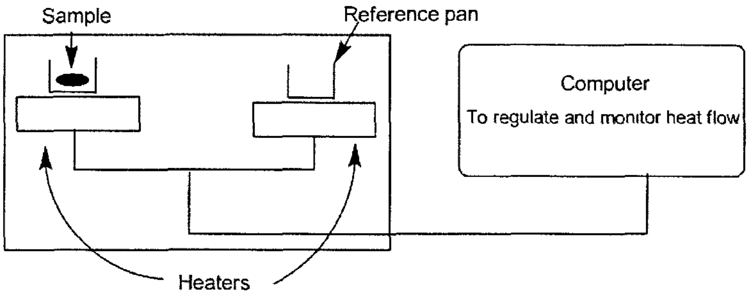

Figure 2.3: The DSC components and operating principle.

2.5 Scanning Electron Microscopy (SEM)

SEM is a type of electron microscope that images a sample by scanning it with a high-energy beam of electrons in a raster scan pattern. When a finely focused electron beam is scanned across the surface of the sample, it generates secondary electrons, backscattered electrons, and characteristic X-rays. These signals are collected by detectors to form images of the sample's surface topography.

Instrumentation

The SEM components and working operating principle are shown in Figure 2.4.

In a typical experiment, the sample is loaded into the instrument. The sample chamber and the column are evacuated. Then an electron gun (at the top of the column) emits a beam of high-energy electrons. This beam travels downward through a series of magnetic lenses designed to focus the electrons to a very fine spot. Near the bottom, a set of scanning coils moves the focused beam back and forth across the specimen, row by row. As the electron beam hits each spot on the sample, secondary electrons are knocked loose from its surface. A detector counts these electrons, sends the signals to an amplifier and then an image is processed.

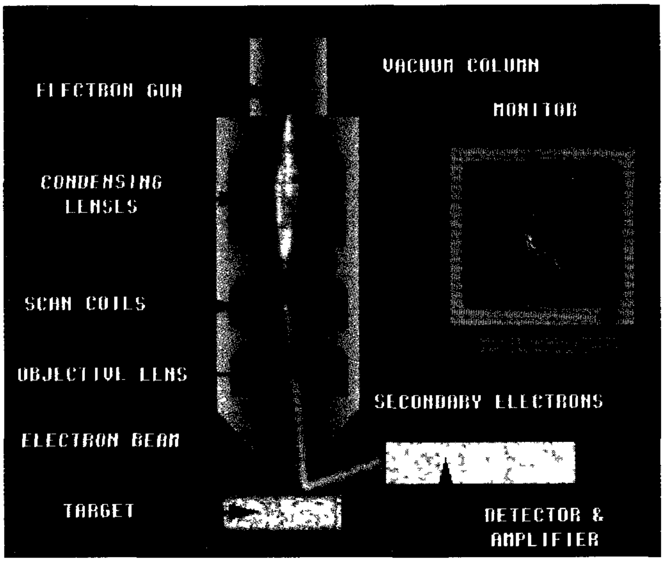

Figure 2.4: The SEM components and working principle.

2.6 Energy-Dispersive X-ray Spectroscopy (EDS)

EDS is an analytical technique used for the elemental analysis of samples. Its fundamental principle is based on the fact that when an electron beam interacts with a sample target a variety of emissions is produced, including X-rays that are characteristic of the emitting element's atomic structure. This is because at rest, an atom within the sample contains unexcited electrons in discrete energy levels bound to the nucleus. The incident beam excites an electron in an inner shell, ejecting it from the shell while creating an electron hole where the electron was. An electron from an outer, higher-energy shell then fills the hole, and the difference in energy between the higher-energy shell and the lower energy shell is released in the form of X-rays.

Instrumentation

Energy-dispersive detector is used (in addition to SEM components shown in Figure 2.4) to separate the characteristic X-rays of different elements into an energy spectrum. This energy spectrum is analyzed with an EDS system software to separate and quantify atomic X-rays from each element present in the sample.[85] The detector contains a crystal that absorbs the energy of incoming X-rays by ionization, yielding free electrons in the crystal that become conductive and produce an electrical charge bias. The X-ray absorption thus converts the energy of individual X-rays into electrical voltages of proportional size; the electrical pulses correspond to the characteristic X-rays of the elements. The EDS data is typically compared with either known or computer-generated standards to produce a full quantitative analysis showing the sample atomic composition.

2.7 Impedance Spectroscopy (IS)

IS is a significant analytical tool for probing many of the electrical properties of materials and their interfaces with electronically conducting electrodes. The theory, experimental and applications of IS have been reviewed.[11] Only principles applicable to solid-electrolyte conductivity measurements are presented here. IS may be used to investigate the dynamics of bound or mobile charge in the bulk or interfacial regions of any kind of solid or liquid material: ionic, semiconducting, mixed electronic-ionic and even insulators (dielectrics)

In a typical IS experiment, a sample is sandwiched between two electrochemically inert electrodes and electrical stimulus (a known voltage or current), is applied to the sample and the response of the sample is measured. It is assumed that the properties of the electrode-material system are independent, and it is one of the basic purposes of IS to determine these properties, their interrelations, and their dependences on such controllable variables as temperature, oxygen partial pressure, applied hydrostatic pressure, and applied static voltage or current.[11]

There are three types of electrical stimulus used in IS.[11] In one type, a step function of voltage [$V(t) = V_0$ for $t > 0$, $V(t) = 0$ for $t < 0$] may be applied at $t = 0$ to the system and the resulting time-varying current $i(t)$ measured. The ratio $V_0/i(t)$, often called the indicial impedance or the time-varying resistance, measures the impedance resulting from the step function voltage perturbation at the electrochemical interface. The advantage of this type of stimuli is that it is easily accomplished experimentally and the independent variable (voltage) controls the rate of the electrochemical reaction at the interface. The stimulus' disadvantage is the need to perform integral transformation of the data and the fact that the signal-to-noise ratio differs between different frequencies, so the impedance may not be well determined over the desired frequency range.

The second type of stimulus is applying a voltage $V(t)$ composed of random (white) noise to the interface and measuring the resulting current. The advantage of this type of stimulus is the fast data collection because only one signal is applied to the interface for a short time. The disadvantage of this stimulus is that it requires true noise and then the need to carry out a Fourier analysis.

The third type of stimulus is applying a single-frequency sinusoidal voltage or current to the interface and measuring the phase shift and amplitude, or real and imaginary parts, of the resulting current at that frequency using either analog circuit or fast Fourier transform (FFT) analysis of the response. This type of stimulus is the most common and standard one used to measure impedance and was the one used in this work. The advantages of this type of stimulus are the commercial availability of instruments to analyze the frequency signal and better signal-to-noise ratio in the frequency range of most interest.

Instrumentation

The IS components and working principle are shown in Figure 2.5. An oscilloscope is used to monitor successful generation of voltage signal (V_{gen}) from the function generator. The sample voltage (V_s) is proportional to the current (I). The signal from the function generator to the sample and to the analyzer input is analog, but it is converted to a digital signal before output to the computer. The signal output is the ratio of V_s/V_{gen}.

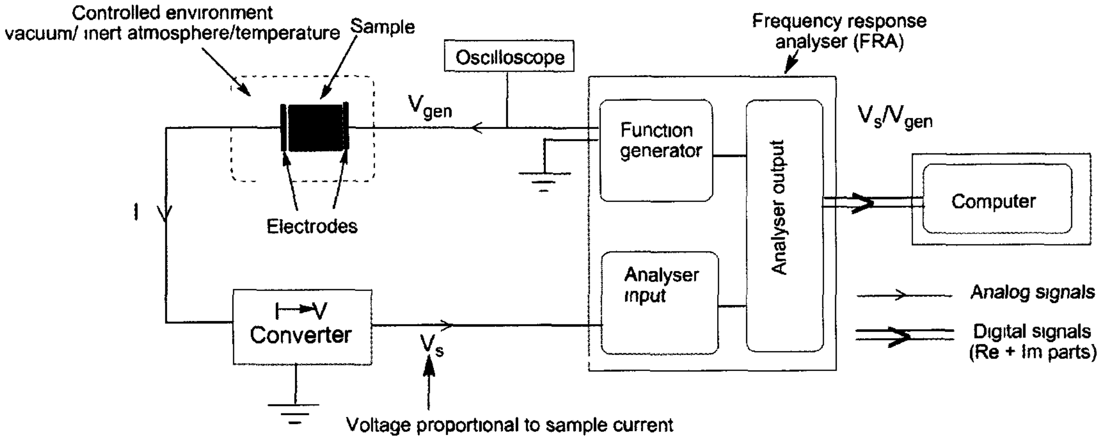

Figure 2.5: Schematic of our AC impedance spectroscopy showing components and working principle.

Any intrinsic property that influences the conductivity of an electrode-materials system, or an external stimulus, can be studied by IS. The properties quantified from an IS spectrum fall generally into two categories.[11] The first category are those pertinent only to the material itself, such as conductivity, dielectric constant, mobility of charges, equilibrium concentrations of the charged species and bulk generation-recombination rates. The second category, includes those properties pertinent to an electrode-material interface such as adsorption-reaction rate constants, capacitance of the interface region, and diffusion coefficient of neutral species in the electrode itself.

Experimental IS data may be analyzed using an exact mathematical model based on a plausible physical theory that predicts theoretical impedance $Z_t(\omega)$, or using a relatively empirical equivalent circuit whose impedance prediction may be denoted by $Z_{ec}(\omega)$ as shown in Figure 2.6. In either one, the case of the relatively empirical equivalent circuit or of the exact mathematical model, the parameters can be estimated and the experimental $Z_e(\omega)$ data compared to either the predicted equivalent circuit impedance $Z_{ec}(\omega)$ or to the theoretical impedance $Z_t(\omega)$. Such fitting is most accurately accomplished by the Complex nonlinear least squares fitting (CNLS) method.

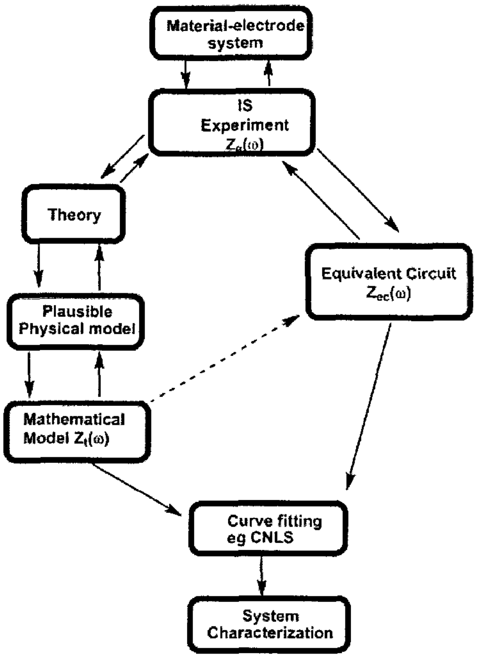

Figure 2.6: Flow diagram for the measurement and characterization of a material-electrode system.xxx. Reproduced from reference [11].

The equivalent circuit to represent the impedance from an electric conductor is a simple R-C parallel circuit composed of a capacitor in parallel with a resistor. With an additional component, the equivalent circuit to represent an ionic conductor is a capacitor in parallel with a resistor and a constant phase element (CPE).[11,86] In both circuits, the resistor represents the impedance of the sample and the capacitor represents the impedance of the cables. The CPE is an equivalent circuit component that represents the impedance behaviour of the blocking electrodes/sample interfaces of an ionic conductor. The CPE represents diffusion effects near blocking electrode. The CPE is a distributed impedance element that aids in adequately describing the electrical response that cannot be well approximated by a finite number of ideal circuit elements.[11] The CPE produces impedance having a constant phase angle in the complex plane given by

$$Z_{CPE} = \frac{1}{\tau(i\omega)^{\phi}} \quad . \tag{2.4}$$

where ϕ determines this angle, which is $\frac{\pi}{2}\phi$, with-1$\leq \phi \leq$1 . In the special case of $\phi = 1$, the CPE acts like a capacitor with ϕ equal to the capacitance C. The CPE can also yield an inductance with $\phi = -1$ or a resistance with $\phi = 0$.

A software program "LEVM" is used in fitting experimental data and uses a type of CNLS fitting called Levenburg-Marquart algorithm.[86]

The impedance spectrum (Nyquist or complex plot), is a plot of the real part of the impedance (Z') against the imaginary part (Z'') of the data collected from a series of frequencies (low to high). The bulk resistance of the sample (R_b) is one of the quantities that can be derived from such a plot. Using the resistance value of the sample (R_b), the sample thickness, and the sample cross-section area the resistivity (ρ) of the sample is calculated. The inverse of resistivity (ρ) is the conductivity (σ) of the sample. The following relationship is used to calculate conductivity.

$$R = \frac{\rho L}{tw} = \frac{L}{\sigma tw} \quad \text{or} \quad \sigma = \frac{L}{Rtw} \tag{2.5}$$

where R = resistance of the sample, ρ = resistivity of the sample, σ = conductivity of the sample and L, t, and w are sample dimensions as shown in Figure 2.7.

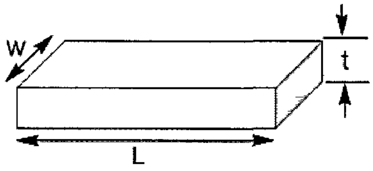

Figure 2.7: Sample dimensions. L=length, w=width and t=thickness.

2.8 Materials characterization

2.8.1 X-ray diffraction

X-ray diffraction studies were carried out on a Bruker AXS D8 Advance instrument equipped with a graphite monochromator, variable divergence slit, variable anti-scatter slit, and a scintillation detector. Cu (Kα) radiation (λ= 1.5406 Å) was used. Samples were prepared at room temperature in air as dry thin films or powders on a glass/silicon substrates.

2.8.2 Nuclei magnetic resonance

The ^{1}H, ^{13}C, and ^{31}P NMR spectra of samples were recorded on a Bruker Advance 300MHz NMR spectrometer. The samples were run at ambient conditions as solutions in deuterium solvents.

2.8.3 Fourier transform infrared spectroscopy

Two kinds of infrared spectrometers were used in this work. In one, the FT-IR spectra were recorded using Brukers's Equinox 55 series spectrometer. The resolution of the instrument was 0.5 cm^{-1} and 64 scans were used. The samples for this technique were dispersed in KBr and pressed into pellets at 25 °C. In the second technique, a Bruker ALPHA FT-IR spectrometer equipped with attenuated total reflectance (ATR) sampling unit was used. The resolution of the instrument was 0.9 cm^{-1}and 128 scans were used. The samples were run without any further preparation for this technique. The spectra were obtained in the range 4000-400 cm^{-1}.

2.8.4 Thermogravimetric analysis

Thermogravimetric Analysis (TGA) was investigated using a TA 500 instrument. The samples were run in dry air or nitrogen purge using a heating rate of 10 °C/min. Nanocomposite samples for TGA analysis were freeze-dried and left in a dessicator overnight, prior to running them.

2.8.5 Differential scanning calorimetry

The TA Q100 instrument was used for DSC analysis. The samples were analyzed under dry nitrogen atmosphere. Variable heating and cooling rates were used to investigate thermal transitions. The nanocomposite were freeze-dried and left in a desiccator overnight prior to analysis. The dry samples were sealed into aluminum pans.

The TGA/DSC data was processed using the TA's Universal Analysis 2000 software.

2.8.6 Impedance spectroscopy

The conductivities of the samples were investigated by AC impedance spectroscopy, using a Solartron 1250 frequency response analyzer and a home-built accessory circuit. The amplitude of the sign wave perturbation was 50 mV and a frequency range of 10 kHz to 0.01 Hz was used. The samples were run as cast films on rectangular glass substrates. Silver paste/paint was placed on the two ends of the films as electrodes. Prior to conductivity measurements, samples were held in vacuum for at least 20 hours at room temperature to remove any moisture and adsorbed volatile materials. The current flow was along the film, parallel to the substrate in a vacuum chamber.

2.8.7 X-ray photoectron spectroscopy

The experiment was performed with a Multilab 2000 XPS system manufactured by Thermo VG Scientific. The XPS data were collected with a dual anode X-ray source using Mg K-alpha irradiation with the energy of 1253.6 eV. Binding energies are measured using a hemispherical energy analyzer with fixed pass energy of 50 eV that gives an energy resolution of approximately 1.1 eV. The spectra collected over 600 μm in diameter sample area. The data were analyzed using an XPS data analysis software, Avantage, version 3.99 developed by Thermo VG Scientific. Fittings of the peaks were performed using the Gaussian-Lorentzian product function and the Shirley background algorithm.

2.8.8 Scanning electron microscopy/energy dispersive X-ray spectroscopy

Scanning electron microscopy (SEM) and energy-dispersive X-ray spectroscopy (EDS) were performed with a Hitachi Tabletop Scanning Electron Microscope TM 3000 equipped with a Bruker Quantax 50 EDS system. A 15 kV accelerating voltage was used. The samples were mounted on a black carbon tape for analysis.

3 Experimental and characterization

3.1 Polymers

3.1.1 Materials

Poly(ethylene glycol) (PEG400) [*Aldrich*] dried with molecular sieve 3 Å under nitrogen before use, methylene chloride (CH_2Cl_2)[*Caledon*] refluxed in calcium hydride (CaH_2) under nitrogen before use, potassium hydroxide (KOH) 85% [*Aldrich*] ground to powder before use, oxalic acid dihydrate ($HOCOCOOH.2H_2O$) 101.3% [*Baker*], methanol (CH_3OH) HPLC grade [Caledon] and benzene 99.9% [*Aldrich*] both used as received.

3.1.2 Poly(oxymethylene-oxyethylene) synthesis

POMOE was synthesized as reported in the literature.[66] Potassium hydroxide (50.0 g, 0.891 mol) powder was introduced into a three neck flask connected to a mechanical stirrer under nitrogen purge from a Schlenk line. Dichloromethane (283.5 g, 180.0 mL) was syringed into the reaction vessel. Polyethylene glycol 400 (PEG 400) (49.3 g, 50.0 mL) was added slowly by means of a dropping funnel to the reaction mixture. The reaction vessel was protected from direct light with aluminum foil. After three days, the excess potassium hydroxide was washed off the thick rubbery product. The thick rubbery product was dissolved in water (500 mL) and purified *via* dialysis for several days. After dialysis, the solution was filtered to remove any suspended particles then it was freeze-dried. A clear colorless rubbery mass of the polymer was obtained. The yield was over 90%.

A complex of POMOE with lithium salt, $LiCF_3SO_3$, was prepared using the optimum ionic conductivity ratio of $[EO]/[Li^+] = 25$ as reported in literature.[66] From here on lithium salt and the polymer lithium complex will be abbreviated as LiX (X= CF_3SO_3) and Li-POMOE, respectively.

3.1.3 Poly[oligo(ethylene glycol)oxalate] synthesis

POEGO was synthesized as reported in the literature.[57] In a typical experiment, PEG 400 (15.0 g, 0.0375 mol) was added to oxalic acid dihydrate (5.0 g, 0.0397 mol) in benzene (100 mL), and the mixture was refluxed for 4 days in a 250 mL round bottom flask while stirring. Benzene was then removed under reduced pressure. Then the product was heated in a vacuum oven at 120°C until a viscous clear product was obtained.

A Li-POEGO complex was prepared using the optimum ionic conductivity ratio of $[EO]/Li^+ = 16$ as reported in literature.[57]

3.1.4 Poly[bis-(2-methoxyethoxyethoxy)phosphazene] synthesis

MEEP was synthesized as reported in the literature [87, 88] with minimal modifications. In a typical reaction, phosphonitrilic chloride trimer (4.00 g, 1.15×10^{-2} mol) was heated at 250 °C for 4 hours in a vacuum sealed glass tube. The resultant products (un-polymerized trimer, linear and cross-linked poly(dichlorophosphazene) $[NPCl_2]_n$) were transferred into a sublimator in a nitrogen atmosphere glove box, and then sublimed under vacuum at 40 °C to remove un-polymerized trimer. The clear rubbery product ($[NPCl_2]_n$) (1.68 g, 1.45×10^{-2} mol), was mixed with THF (79 mL). Meanwhile, sodium hydride (0.72 g. 0.030 mol) was refluxed in THF (100 mL) for 30 minutes under nitrogen purge, prior to the addition of MEEOH (5.0 mL). On adding MEEOH, the reaction mixture turned from a white suspension to a clear yellow solution (the alkoxide). The alkoxide was refluxed for 2.5 hours. The $[NPCl_2]_n$ solution was then slowly syringed into the alkoxide solution while lowering the temperature. The transfer was completed at 50 °C. The resulting mixture turned to dark brownish with cloudy-suspensions (due to precipitation of NaCl). After 18 hours, most of the THF evaporated, and the reaction was stopped and cooled down to room temperature. The product was precipitated by adding n-heptane. After decanting the solvents, the product was vacuum-dried for 30 minutes. The brown-colored product was then dissolved in water and purified *via* dialysis for seven days to remove the NaCl by-product. The excess water was then removed by freeze-drying, and a light-brown sticky product (yield $< 30\%$) was obtained.

A Li-MEEP complex was prepared using the optimum ionic conductivity ratio of $[EO]/Li^+ = 4$ as reported in the literature.[87]

3.2 Layered structures

3.2.1 Materials

Sodium metavanadate ($NaVO_3$) 98% [*Fluka*], Dowex 50W-X8, 20-50 mesh [*Baker*], iron (III) oxide (Fe_2O_3) 99+% [*Aldrich*], and sodium peroxide (Na_2O_2) [*Fisher*] all used as received.

3.2.2 Vanadium pentoxide xerogel ($V_2O_5nH_2O$) synthesis

The synthesis of $V_2O_5nH_2O$ xerogel was adapted from the literature.[89] For this work, sodium metavanadate (4.0 g, 0.033 mol) was dissolved in deionized water (150 mL). The resulting colorless solution was then passed through an acidic ion exchange column (510 meq capacity) made from Dowex 50W-X8, 20-50 mesh resin. The collected eluate, (200 mL), was the yellow-brownish polyvanadic acid (HVO_3). The excess water was evaporated from the HVO_3 at room temperature for two weeks and the solution polymerized to the dark-red xerogel ($V_2O_5nH_2O$). The $V_2O_5nH_2O$ solution was used without further dilution in the intercalation reactions.

3.2.3 Sodiun iron oxide ($NaFeO_2$) synthesis

Sodium iron oxide was prepared as reported in the literature[52] with minimal modifications. In a typical experiment, sodium peroxide (8.5 g, 0.109 mol) was mixed with iron (III) oxide (15.4 g, 0.096 mol) and ground together in the glove box under nitrogen atmosphere. The resulting solid-solution was heated in the furnace in two steps. First, it was heated at 500 °C for 12 hours, cooled to room temperature and reground. Then it was heated again to 700 °C for another 12 hours. A granular brown product ($NaFeO_2$) was obtained.

Hydrolysis of $NaFeO_2$ and identification of its products

A portion of the product (6.0 g, 0.054 mol) was mixed with deionized water (60.0 mL) and stirred for about five minutes, then left for solids to settle down before decanting the top clear solution. Note that if excess Na_2O_2 is used during the synthesis of $NaFeO_2$, a green[1] solution is obtained. This is because some of the Fe (III) get reduced to Fe (II). The higher the concentration of Fe (II), the darker the green colour. Otherwise, the extract solution is colourless. In this article, the terms "extract" and "residue" will be referred to the aqueous solution and the sediment solids, respectively, after hydrolysis of α-$NaFeO_2$. The physical identification of the hydrolysis products is provided in Figure 3.1.

---

[1] The green colour of the extract comes from hexaaquairon (II) complex ion. The hexaaquairon (II) complex is unstable as it readily oxidizes to hexaaquairon (III) leading to the fading of the green color and deposition of brown particles.

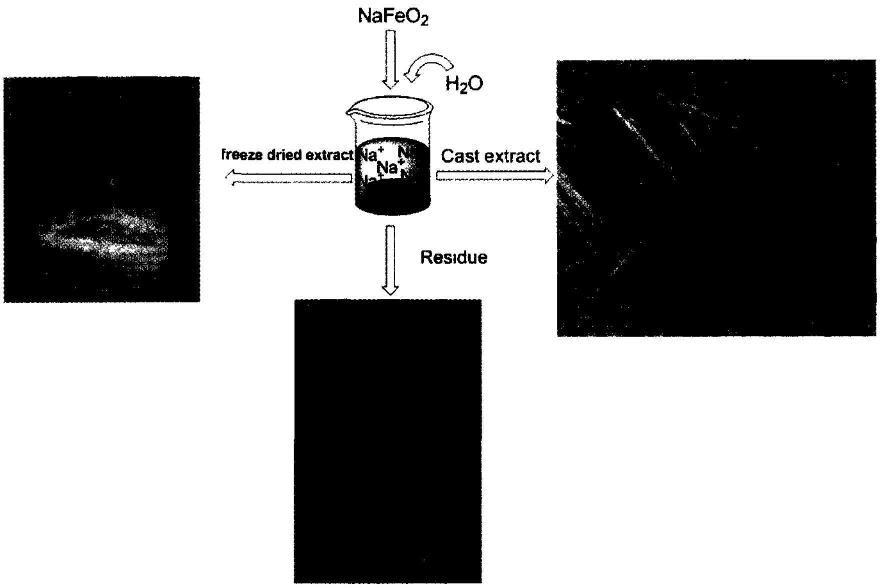

Figure 3.1: TA schematic showing the hydrolysis products of $NaFeO_2$. The cast extract crystallizes into needle-like crystals, the freeze dried extract yields a white powder, and the sediment solids are brown like pristine $NaFeO_2$.

Intercalation of guest molecules

In a typical intercalation reaction, the extract (10.0 mL) was mixed with the guest solution (5.0 mL), and stirred for 30 minutes. For carbon monoxide capture, the gas was bubbled into the extract solution for 30 minutes.

3.3 Intercalated nanocomposites

3.3.1 $V_2O_5nH_2O$/POMOE/POEGO/MEEP

The nanocomposites were prepared by adding the solution of the polymer into an aqueous solution of $V_2O_5nH_2O$, and stirring magnetically for 30 minutes at room temperature in air. For POMOE a typical experimental procedure for mole ratio 1:1 is as follows: 7.8 mL of the xerogel (95.9 mg, 4.44×10^{-4} mol) was mixed with 2.0 mL of POMOE solution in methanol (1.47×10^{-4} mol). The following mole ratios were prepared 1:0.5, 1:1, 1:2, 1:3, and 1:4.

For POEGO a typical experimental procedure for mole ratio 1:1 is as follows: 13.0 mL of the xerogel (0.160 g, 7.40 x 10^{-4} mol) was mixed with 1.0 mL of POEGO solution in methanol (1.25 x 10^{-4} mol). The following mole ratios were prepared 1:0.5, 1:1, 1:2, 1:3, and 1:4.

For MEEP a typical experimental procedure for mole ratio 1:1 is as follows: 10.0 mL of the xerogel (0.123 g, 5.69 x 10^{-4} mol) was mixed with 6.0 mL of aqueous solution of MEEP (1.2 x 10^{-4} mol). The following mole ratios were prepared 1:0.5, 1:1, 1:2, and 1:3. The mole ratios were calculated based on moles of $V_2O_51.9H_2O$ and moles of the polymers' repeat units. From here on the nanocomposites will be referred to as V_2O_5POLYMER followed by the mole ratio e.g V_2O_5POMOE 1:3 for the mole ratio of one to three.

To confirm that the polymer chains were actually intercalated into $V_2O_5nH_2O$, a control sample was prepared and characterized. The control sample was prepared by adding methanol (5.0 mL) (the solvent) into an aqueous solution of $V_2O_5nH_2O$ xerogel (10.0 mL) and stirred for 30 minutes. From here on this control sample will be denoted as V_2O_5MeOH.

3.4 Characterization

3.4.1 Polymers

The successful synthesis of the polymers was confirmed by FTIR, TGA, DSC, and NMR. FTIR of the three polymers (POMOE, POEGO and MEEP) are shown in Figure 3.2-3.4. The characteristic infrared bands of the polymers were as follows: POMOE $\nu_{\text{max}}/\text{cm}^{-1}$ 2870, 949, 850 (CH),and 1113 (C-O-C); POEGO $\nu_{\text{max}}/\text{cm}^{-1}$ 2872w, 952 and 861 (CH), 1770s and 1745s (COCO) and 1115s (C-O-C); MEEP $\nu_{\text{max}}/\text{cm}^{-1}$ 2877, 847 (CH), 1237, 799, and 755 (PNP), 1198, 1041, and 962 (P-O-C), 1107 (C-O-C).

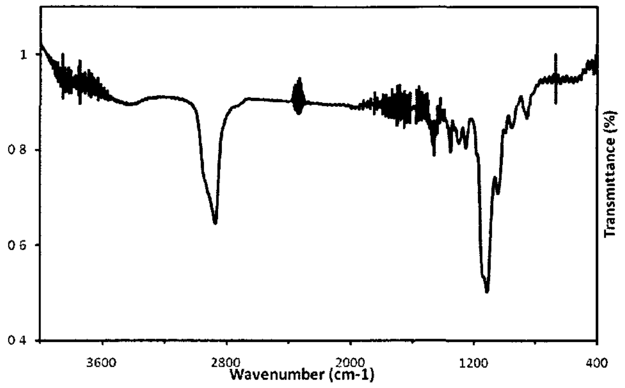

Figure 3.2: FTIR spectrum of POMOE.

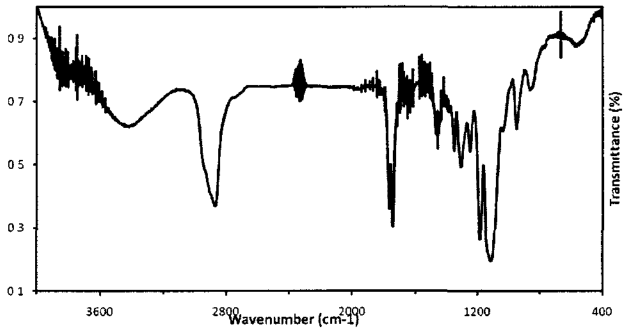

Figure 3.3: FTIR spectrum of POEGO.

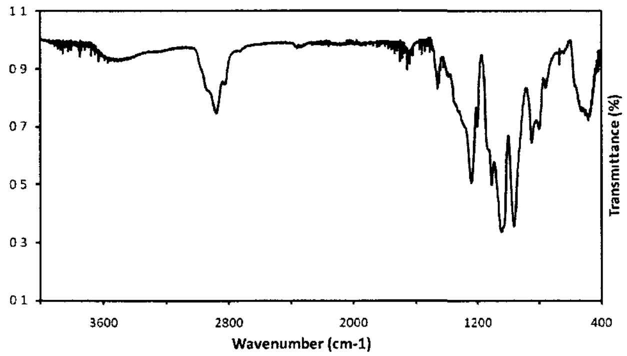

Figure 3.4: FTIR spectrum of MEEP.

The TGAs of the polymers are shown in Figure 3.5. POMOE and POEGO had same decomposition profile. They are stable up to around 200 °C. Then they decompose completely in one weight loss step. On the other hand, MEEP is stable

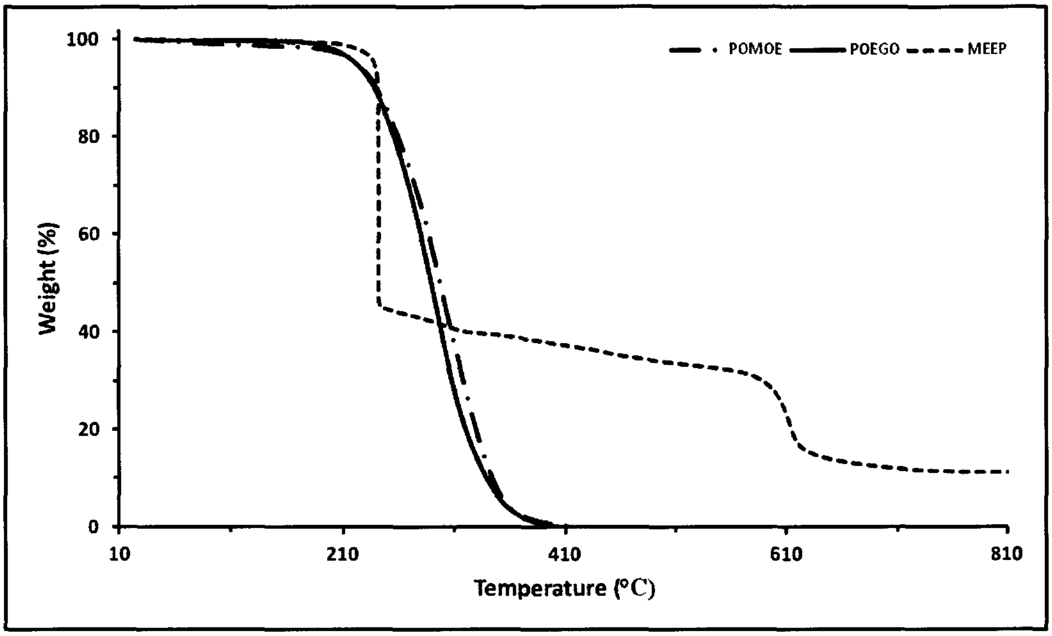

Figure 3.5: TGAs of POMOE, POEGO and MEEP.

to around 220 °C and decomposes in two weight loss steps: one step at 220 °C and another step at around 600 °C. MEEP does not decompose completely in air and has a residue of about 11% (wt). The residue is from the inorganic (phosphorus) part of the polymer.

The DSC of the polymers was found to be very interesting and different from each other. MEEP is a sticky and completely amorphous polymer: it does not show any crystallization or melting phase transitions. Its glassy transition is below -80 °C. POMOE is a viscous polymer and shows three phase transitions, the glass transition (-65 °C), crystallization (-9 °C) and melting (14 °C) phase transitions. The DSC spectra for POMOE and MEEP are shown in Figure 3.6.

POEGO's DSC was unique in that it was dependent on the cooling rate. If the sample was cooled at the standard rate of 5 °C/minute, you do not see the crystallization transition on cooling but rather when heating the sample. When the observation was first made, it was intriguing to find out what caused the shift of the crystallization phenomenon. The finding was that POEGO is fluid and cooling it fast does not

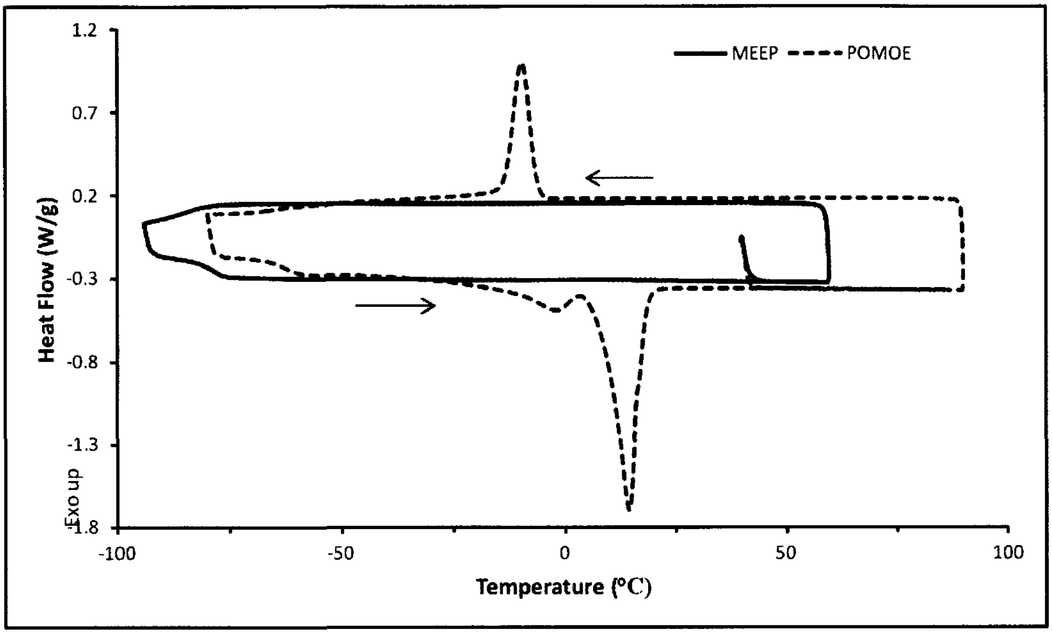

Figure 3.6: DSC curves for POMOE and MEEP.

allow the polymer chains to reorganize themselves. Therefore, an amorphous phase is obtained. After the glass transition, a super cooled liquid is obtained which then crystallizes before melting hence causing the observed crystallization shift. Figure 3.7 shows the DSC with the cooling rates of 5 °C/minute and 2 °C/minute.

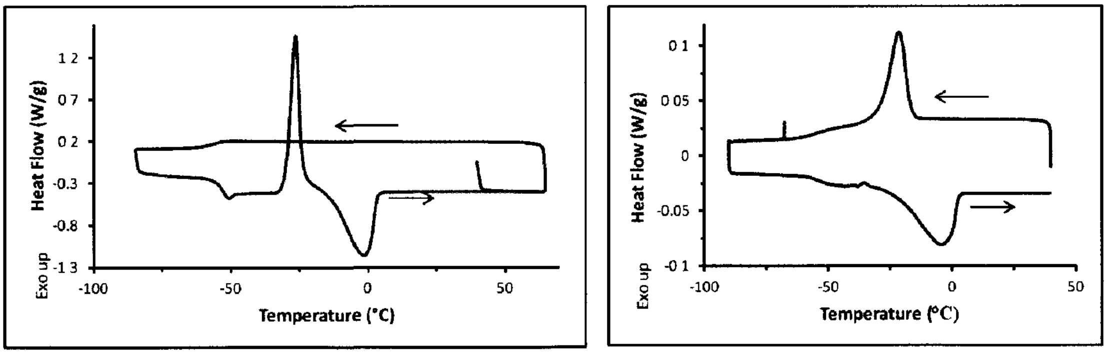

Figure 3.7: DSC of POEGO cooled at rates of 5 °C/minute (left) and 2 °C/minute (right).

NMR spectroscopy was especially useful in the confirmation of successful synthesis of MEEP. ^{31}P NMR was used to probe the reactions and confirmation of the final product. The ^{31}P NMR of MEEP had a chemical shift of -7.1 ppm and that of its intermediate polydichlorophosphazene $[NPCl_2]_n$ had a chemical shift of -17.0 ppm.

The ^1H NMR of the polymers and their interpretations are shown in the Figures 3.8 and 3.9.

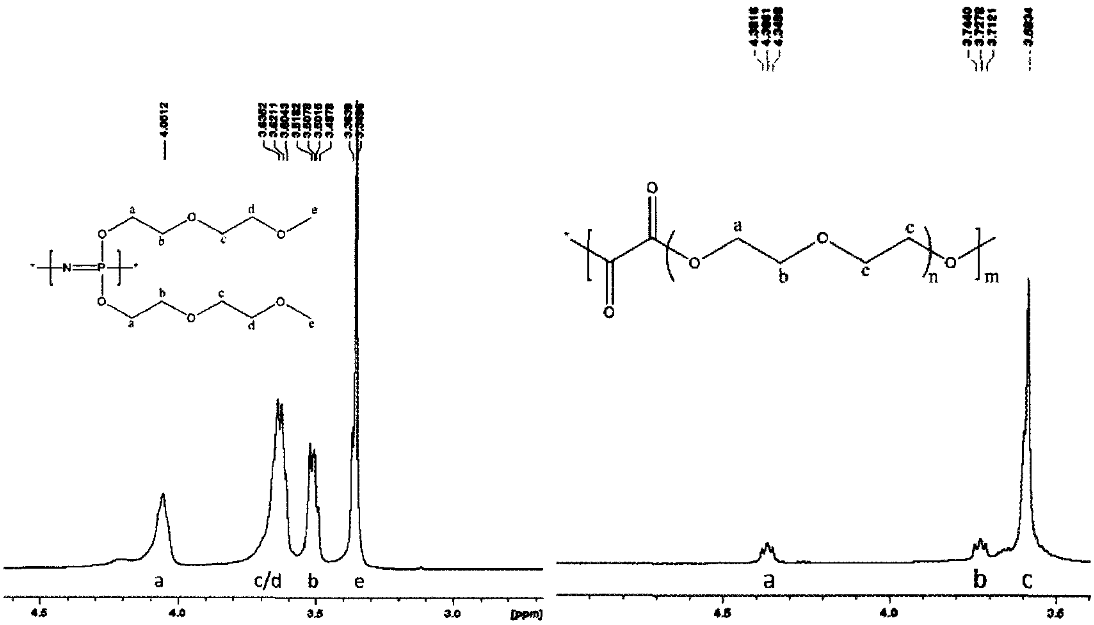

Figure 3.8: ^1H NMR and chemical shift assignments for A) MEEP, B) POEGO.

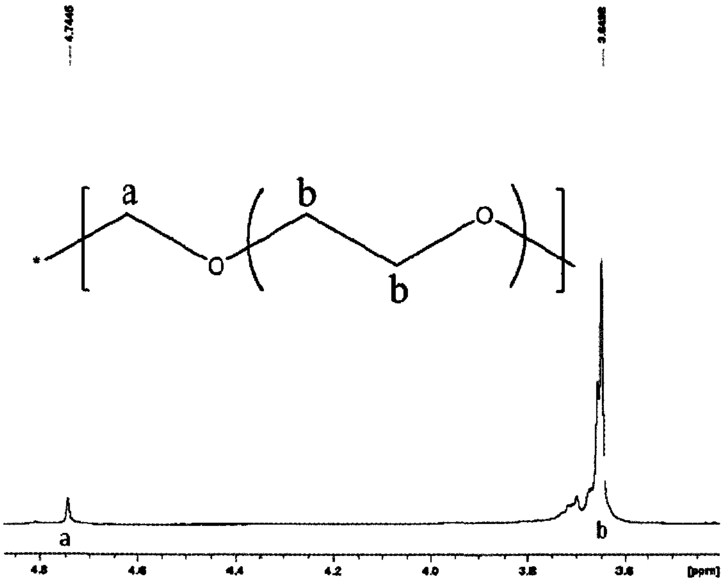

Figure 3.9: ^1H NMR and chemical shift assignments for POMOE.

3.4.2 Layered structures

The successful synthesis of the layered structures was confirmed by PXRD and TGA. The XRD pattern for $V_2O_5nH_2O$ is shown in Figure 3.10. The d-spacing was 11.9 Å. The n value was determined by TGA[2] to be 1.9 (lit.[35]n = 1.8 and d = 11.6 Å).

The successful synthesis of $NaFeO_2$ was confirmed by PXRD. The diffraction pattern was searched in the ICDD database and matched well with the indexed pattern ICDD card number. The XRD and the indexing patterns from the databased are displayed in Figure 3.11.

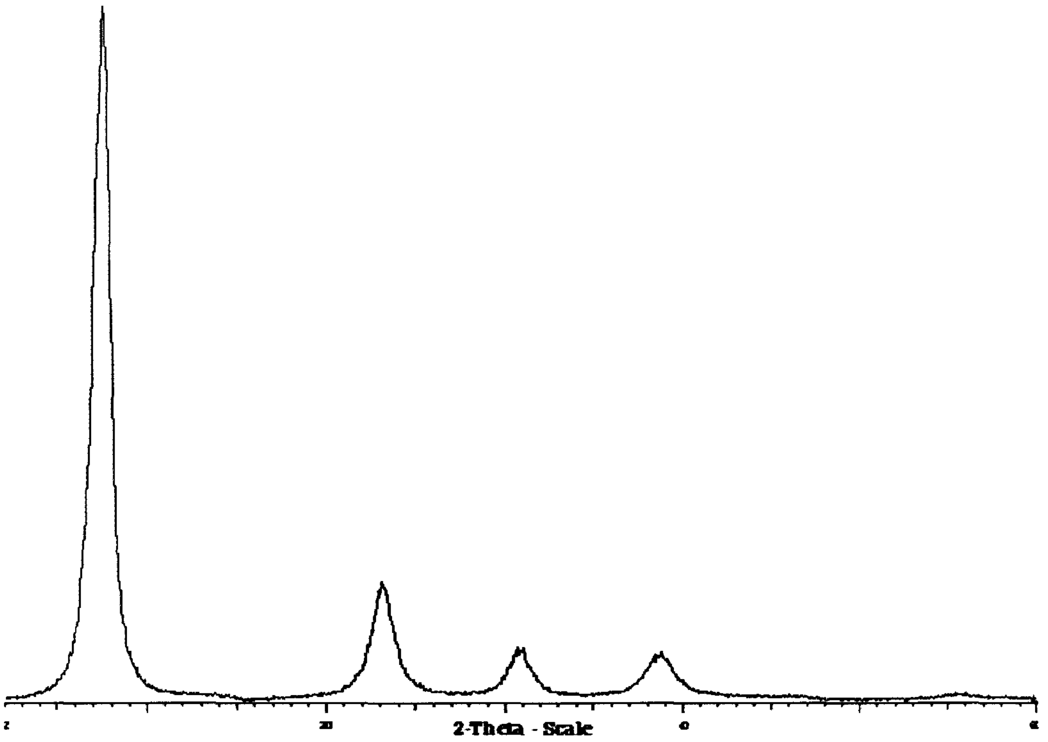

Figure 3.10: a) XRD of $V_2O_5nH_2O$

---

[2] Moles of water present was calculated from the mass loss, and expresed with respect to the moles of the V_2O_5 (residue). More detailed explanation provided in chapter 4

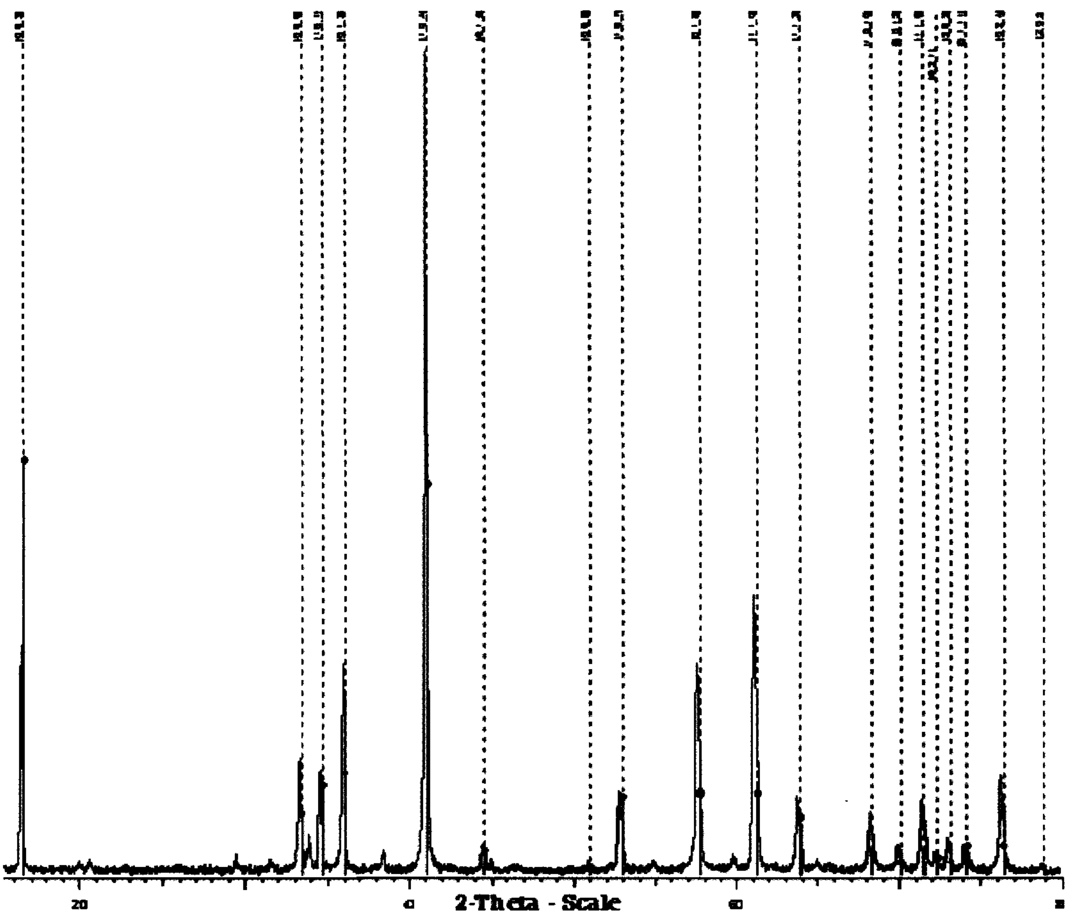

Figure 3.11: The XRD and Indexing pattern for $NaFeO_2$.

3.4.3 Nanocomposites

The nanocomposites were characterized by PXRD, TGA, DSC, FTIR, SEM, EDS, and AC impedance spectroscopy. The results and discussion are presented in the following chapters.

4 Vanadium Pentoxide Xerogel-Poly(oxymethylene-oxyethylene)

4.1 Results and discussion

A room temperature method for intercalating poly(oxymethylene-oxyethylene) (POMOE) and $LiCF_3SO_3$-POMOE complex into $V_2O_5nH_2O$ xerogel leading to a bilayer arrangement of the POMOE-chains within the gallery spaces is reported. This is a significant step towards developing electrolyte/cathode materials capable of intercalating more Li-ions in comparison to monolayers, hence improving the energy and power density of lithium/Li-ion batteries. A series of intercalates were prepared to study the effect of changing the polymer concentration on the interlayer expansion of the layered host, and to determine the optimal (maximum polymer loading) intercalation ratio. An intercalation reaction mechanism is proposed. A hydrogen-bonding network between the polymer and the V_2O_5 framework contributes significantly to the formation of the nanocomposites. The nanocomposites showed a reversible color change from red to green when subjected to electrical stimuli, thus making them good candidates for electrochromic devices. The materials were characterized by powder X-ray diffraction, thermogravimetric analysis, differential scanning calorimetry, Fourier transform infrared spectroscopy, and alternating current impedance spectroscopy.

4.1.1 X-ray diffraction

X-ray diffraction technique was used to confirm the successful intercalation of POMOE into $V_2O_5nH_2O$ and the identity of the as synthesized $V_2O_5nH_2O$ xerogel. The nanocomposites showed complete intercalation of the polymer into the gallery spaces based on the absence of pristine $V_2O_5nH_2O$ diffraction peaks. The XRD patterns for $V_2O_5nH_2O$, V_2O_5MeOH and V_2O_5POMOE1:1 are shown in Figure 4.1. Figure 4.1 curve *c* shows the XRD pattern for V_2O_5POMOE1:1. The XRD pattern shows a d-space increase to 20.6 Å, which corresponds to an interlayer expansion of 8.7 Å with respect to $V_2O_5nH_2O$ (d=11.9 Å). Other intercalates showed similar features. A complete summary of XRD data is summarized in Table 4.1.

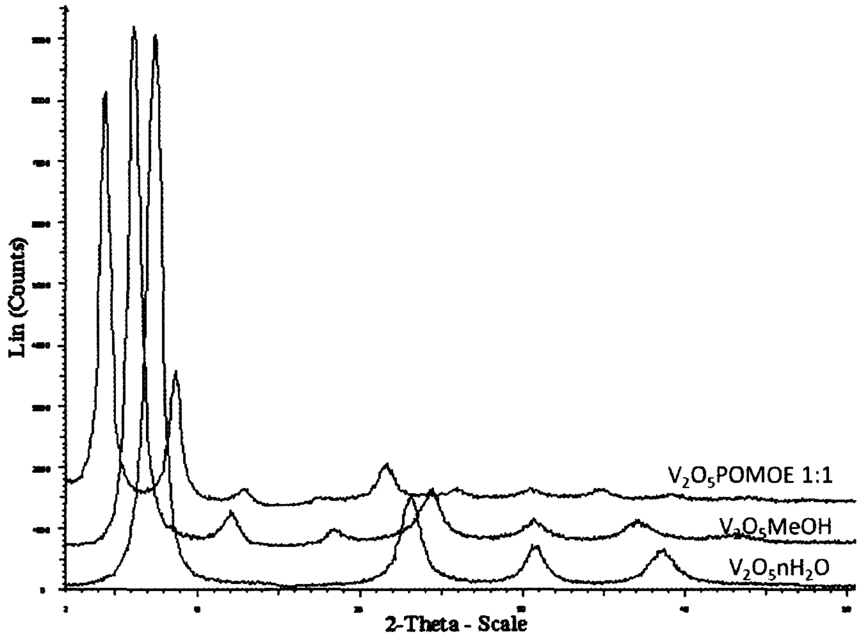

Figure 4.1: XRD for a) $V_2O_5nH_2O$, b)V_2O_5MeOH, and c) V_2O_5POMOE 1:1.

The interlayer spacing (d) for the as prepared $V_2O_5nH_2O$ film was 11.9 Å, and n was thermogravimetrically determined to be 1.9 (lit.[35] n = 1.8, d = 11.5 Å). The d value is depended on the amount of intercalated water molecules (n). The XRD of the nanocomposites shows only (*00l*) reflections, which is indicative of highly oriented materials. From Table 4.1 it is clear that there is no significant increase in d-spacing as the amount of POMOE is increased, an indication that the average net expansion of 8.7 Å corresponds to the optimum loading of POMOE chains within the $V_2O_5nH_2O$

Table 4.1: Summary of interlayer expansions and average crystallite sizes for the materials.

Material	Observed d-spacing (Å)	Expansion Δd-spacing (Å)	Average Crystallite size (Å)
$V_2O_5nH_2O$	11.9	-----	73
V_2O_5 MeOH	14.5	2.6	89
V_2O_5POMOE 1:0.5	20.2	8.3	119
V_2O_5POMOE 1:1	20.6	8.7	114
V_2O_5POMOE 1:2	20.6	8.7	104
V_2O_5POMOE 1:3	20.5	8.6	90
V_2O_5POMOE 1:4	20.6	8.7	79

ribbons.

Here is how this work relates to other similar work in the literature. Kloster *et al.* using water as solvent intercalated POMOE into $V_2O_5nH_2O$, reported a d-space increase of 4.5 Å and proposed a monolayer of the POMOE-chain within the gallery space.[90] Since POMOE is a derivative of PEO, this interpretation was consistent with Kanatzidis *et al.* 's work on the intercalation of PEO into $V_2O_5nH_2O$. In fact, Kanatzidis *et al.* were the first to report on the intercalation of PEO into $V_2O_5nH_2O$ with a d-space increase of 4.5 Å.[91] Later, Kanatzidis *et al.* [92] and Guerra *et al.* [89] using aqueous solutions of PEO with slow evaporation of water were able to report an interlayer expansion of 8 Å or higher and they suggested a bilayer loading of the PEO-chains within the V_2O_5 framework. Guerra *et al.* also observed that the interlayer expansion was independent on the molecular weight of the PEO. 1-D (one dimension) electron density (ED) calculations performed by Kanatzidis *et al.* provide supporting evidence for a bilayer loading of the PEO chains in the V_2O_5 framework.[20] Liu *et al.* calculated ED maps along the c axis and reported that a bilayer loading of PEO-chains fully extended (i.e. zigzag conformation) parallel to each other was the most likely conformation for an interlayer expansion of about

8 Å. Similarly, intercalation of POMOE into tin disulfide[72] was reported with an interlayer expansion of 8.7 Å and a bilayer conformation was proposed. With all of the above evidence and arguments the average interlayer expansion of 8.7 Å observed here was assigned to a bilayer conformation of the POMOE-chains within the V_2O_5 ribbons in a parallel arrangement to each other. A schematic showing the lamellar representation of the nanocomposites is shown in Fig. 4.2.

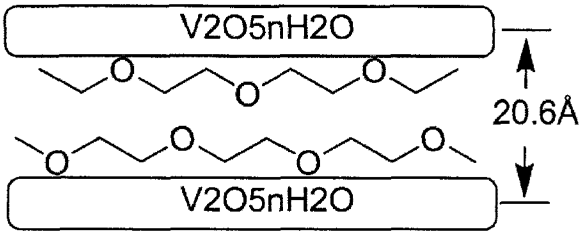

Figure 4.2: Schematic representation of the nanocomposites.

The difference between the monolayer loading reported by Kloster *et al.* and the bilayer arrangement reported in this work could be due to two factors. The first factor was the solvent used. While Kloster *et al.* used water, we used methanol as the solvent. The second factor could be the ageing period of $V_2O_5nH_2O$ xerogel. In our case, we used a two week aged $V_2O_5nH_2O$ gel (dark red) without any dilution.

The intercalation mechanism and the success of the reaction can be explained based on the following findings. Ruiz-Hitzky *et al.* [93] reported that the presence of water in the reaction assures a well controlled swelling of the V_2O_5 layers, allowing the penetration of the polymer chains. The absence of water strongly limits the intercalation process, whereas the absence of organic solvents provokes a complete colloidal dispersion of the vanadium pentoxide, thereby destroying the ribbons and making it difficult to obtain well-defined intercalated phases. Based on this report we decided to use $V_2O_5nH_2O$ gel without allowing it to dry completely to ensure its homogeneity and the presence of water in the reaction mixture. The polymer was dissolved in methanol to ensure the presence of organic solvent in the reaction.

Another advantage of using methanol is that it can be easily removed to facilitate the drying process of the nanocomposite films. The intercalation mechanism can be summarized as shown in Figure 4.3.

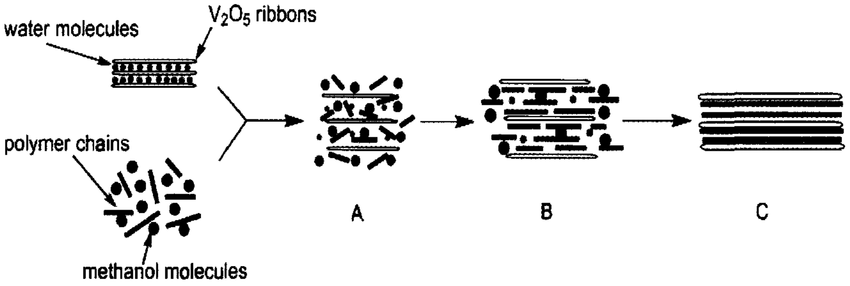

Figure 4.3: Schematic of the intercalation reaction mechanism. A) shows the swelling of the ribbons and penetration of methanol and polymer molecules, B) shows alignment of the polymer chains as the excess solvent is removed and excess polymer chains flows out of the interlayer spaces, and C) shows the dry cast film of the intercalated vanadium pentoxide ribbons. Horizontal arrows represent time progression.

During intercalation, the $V_2O_5nH_2O$ ribbons are swelled by methanol allowing penetration of the POMOE chains and methanol molecules (Figure 4.3 A). Then, as the methanol is removed or evaporated the hydrogen atoms of POMOE interacts with oxygen atoms (V=O) of $V_2O_5nH_2O$ ribbons leading to the formation of hydrogen bonds (Figure 4.3 B). The formation of hydrogen bonds was confirmed by the presence of an infrared band at 3445 cm^{-1} in the IR spectrum of the intercalated product. When the excess solvent is removed by slow evaporation of the cast solution, the vanadium oxide ribbons oriented in the *ab* plane coated with POMOE chains on both sides re-stack, resulting in a bilayer loading of the polymer chains (Figure 4.3 C). The observation that even higher polymer ratios yield a bilayer loading means that when the V_2O_5POMOE solution is cast to form films, any excess POMOE that enters the gallery space actually flows out. This interpretation is supported by the XRD pattern of the films which show only (*00l*) reflections. The presence of (*00l*) diffraction peaks in the XRD patterns of the nanocomposites show that the lamellar structure of the $V_2O_5nH_2O$ xerogel is maintained as shown in Figure 4.1. Other evidence to support the flow of the excess polymer during the formation of the cast films was an observation made from the dry cast films obtained after casting nanocomposite solutions with higher polymer ratios. These dry cast films showed shiny regions around the edges, which could be from the excess polymer.

The peak widths in the XRD patterns were found to decrease when small amounts of POMOE were used. This was thought to be due to changes in crystallite size. The average crystallite size of the nanocomposites was calculated using the Scherrer equation (2.2), and the values are shown in Table 4.1. The average crystallite size of pristine $V_2O_5nH_2O$ is 73 Å, and its crystallite size increases to 119 Å upon formation of the intercalated phase V_2O_5POMOE1:0.5. Subsequent increase of the POMOE content in the nanocomposite leads to a decrease in crystallinity. Therefore, the presence of small amounts of the polymer improves the uniform stacking of the $V_2O_5nH_2O$ ribbons.

4.1.2 Thermogravimetric analysis

Thermogravimetric analysis was used to further characterize the materials. Figure 4 shows the thermogram in air for POMOE, V_2O_5POMOE1:1, and V_2O_5POMOE1:4. Pure POMOE (Figure 4.4 curve *a*) is stable up to 298 °C, thereafter decomposing completely in a single weight loss step of 98.9%. V_2O_5POMOE1:1 (Figure 4.4 curve *b*) is stable up to 173 °C, and then decomposed in a one-step weight loss of 41.8%, producing a constant weight percentage residue of 45.6%. However, V_2O_5POMOE1:4 (Figure 4.4 curve *c*) showed a two-step weight loss of 54.3% and 13.8% around 253 °C and 440 °C, respectively. The first weight loss is due to the intercalated polymer and the second weight loss corresponds to externally lying polymer.

It is worthy to note that the nanocomposites decompose at lower temperatures compared to pure POMOE. The lower decomposition temperatures indicates that the presence of the V_2O_5 in the nanocomposites catalyses the thermal decomposition of the polymer. This interpretation is supported by the observation that with higher V_2O_5 ratio (such as in V_2O_5POMOE1:1) the decomposition is faster leading to a sharp drop in weight loss as shown in Figure 4.4 curve *b*.

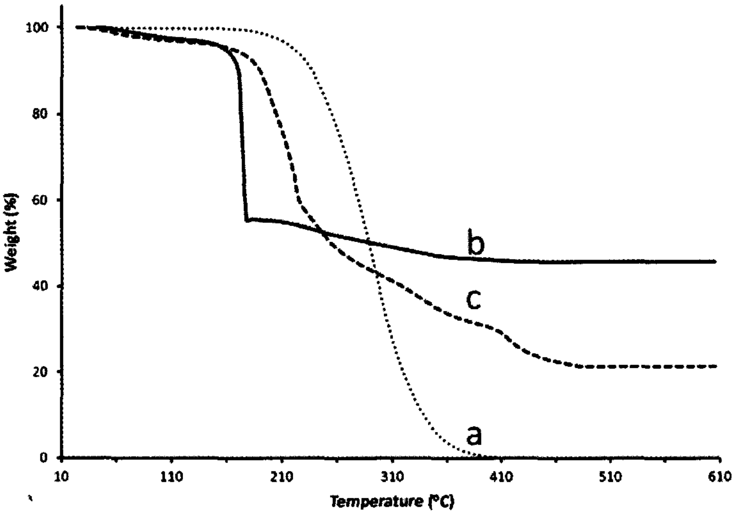

Figure 4.4: TGA of a) POMOE, b) V_2O_5POMOE1:1, and c) V_2O_5POMOE1:4.

For comparison, the decomposition profile of $V_2O_5nH_2O$ in both air and nitrogen, as well as that of V_2O_5MeOH in air are shown in Figure 4.5. It was found that the weight loss due to evaporation of water from $V_2O_5nH_2O$ (Figures 4.5 curve *a* and *b*) was independent of the atmosphere used. This is strong evidence that the weight loss was due to an evaporation process and therefore, was not facilitated through an oxidation reaction.

Figures 4.5 curve *a* and *b*, show a two-step weight loss process. The initial weight loss step corresponds to the evaporation of adsorbed and loosely bound water molecules from the xerogel. The second weight loss step corresponds to the removal of coordinated and/or strongly bound water molecules to the vanadium centers. The rising mass of the residue is due to oxidation reaction. From the TGA data, the amount of loosely bound water (H_2O_{LB}) and tightly bound water (H_2O_{TB}) were calculated. The exact composition of vanadium pentoxide xerogel could, in fact, be written as $V_2O_5(H_2O_{LB})_{1.6}(H_2O_{TB})_{0.3}$. However, for convenience the loosely bound

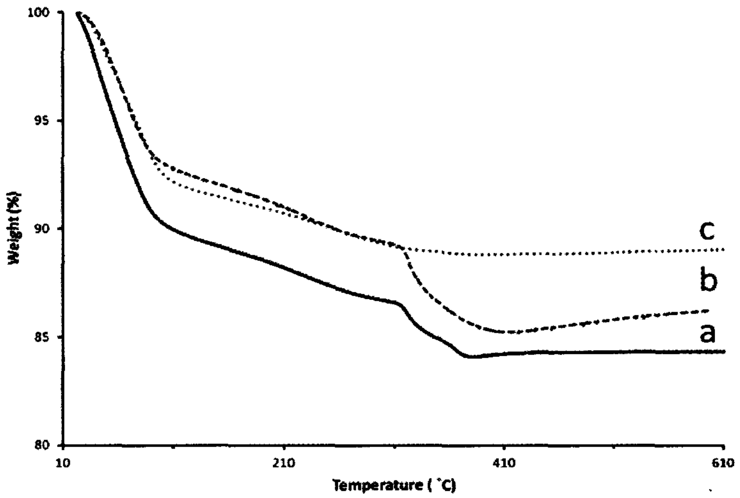

Figure 4.5: TGA of a) $V_2O_5nH_2O$ in air, b) $V_2O_5nH_2O$ in nitrogen and c) V_2O_5MeOH in air.

and tightly bound water are combined together and the chemical formula is written as $V_2O_5(H_2O)_{1.9}$. The decomposition profile for V_2O_5MeOH (Figure 4.5 curve *c*) shows a one step weight loss below 100 °C. The absence of a weight loss above 300 °C in V_2O_5MeOH provides strong evidence that the strongly bound interlayer water molecules in $V_2O_5nH_2O$ are displaced by methanol upon intercalation. For simplicity, the removal of water can be expressed as follows.

$$V_2O_5(H_2O)_{1.9} \xrightarrow{110^oC} V_2O_5(H_2O)_{0.3} \xrightarrow{320^oC} V_2O_5$$

$$V_2O_5(MeOH)_{0.7} \xrightarrow{110^oC} V_2O_5$$

A complete list of the decomposition profile of the nanocomposites is shown in Table 4.2.

It is clear (from Table 4.2) that increasing the amount of POMOE decreased the residue percentage. This is expected because increasing the amount of POMOE decreases the concentration of $V_2O_5nH_2O$ from which the residue is derived. The thermal stability of the nanocomposites increases from around 186 °C to around 253 °C as the mole ratio of POMOE is increased from 0.5 to 4, respectively. This is due to reduced catalytic combustion effect of V_2O_5 at higher polymer ratio.

The stoichiometric compositions of the nanocomposites were calculated from the

Table 4.2: Summary of TGAs for POMOE, $V_2O_5nH_2O$, and V_2O_5POMOE nanocomposites in air.

Material		Decompositions in air		Residue (wt %)
Mole ratios	TGA Stoichiometry	Weight (%)	Temp.(^{0}C)	
POMOE	--------------	98.9	298	0.2
$V_2O_5nH_2O$	$V_2O_5(H_2O)_{1.9}$	10.3 , 2.5	49 , (321 , 364)	84.3
V_2O_5MeOH	$V_2O_5(MeOH)_{0.7}$	8.4	80	88.8
V_2O_5POMOE (1:0.5)	$V_2O_5(POMOE)_{0.2}(H_2O)_{1.3}$	28.0	186	60.1
V_2O_5POMOE (1:1)	$V_2O_5(POMOE)_{0.5}(H_2O)_{0.7}$	41.8	173	45.6
V_2O_5POMOE (1:2)	$V_2O_5(POMOE)_{1}(H_2O)_{1.1}$	54.9	181	29.6
V_2O_5POMOE (1:3)	$V_2O_5(POMOE)_{1.5}(H_2O)_{1.6}$	53.8 , 10.1	223 , 416	21.3
V_2O_5POMOE (1:4)	$V_2O_5(POMOE)_{1.8}(H_2O)_{1.5}$	54.3 , 13.8	253 , 440	18.7

decomposition profiles. The weight loss steps are grouped into four stages: stage I (<120 °C), stage II (121-390 °C), stage III (391-500 °C) and residue (>500 °C) as stage IV.In stage I solvent/water is removed. Stage I is observed in all nanocomposites, as well as in the control sample (V_2O_5MeOH). Stage II corresponds to the decomposition of the intercalated polymer. Stage III, which is present in samples with higher polymer content (>1:9), is assigned to the un-intercalated POMOE-chains. Increasing the polymer mole ratio from 1:3 to 1:4 increases the stage III weight loss percentage by 4%. The reported stoichiometric ratios (in Table 4.2) for the samples showing stage II and III (V_2O_5POMOE1:1 and 1:4) represent a combined POMOE ratio. The residue phase (yellow in colour) was identified by XRD to be orthorhombic V_2O_5. Table 4.2 provides a complete list of the calculated stoichiometric ratios. Although the composition ratios (by TGA) of the nanocomposites show lower polymer ratio than the experimental mole ratios used, the trends are very consistent with each other.

4.1.3 Differential scanning calorimetry

DSC was used to investigate any phase transitions occurring in the nanocomposites. The nanocomposites exhibit a glass transition temperature (T_g), crystallization temperature (T_c), melting temperature (T_m) and a blending temperature (T_e). A glass transition is a reversible transition in amorphous regions within semicrystalline materials (or amorphous materials) from a hard and relatively brittle state into a molten or rubber-like state. Figure 4.6 shows the thermal transitions for V_2O_5POMOE1:1 and V_2O_5POMOE1:4. A cold crystallization is observed for V_2O_5POMOE1:1 (Figure 4.6 curve *b*) which is absent in the nanocomposites with higher molar ratios. Other intercalates showed features similar to V_2O_5POMOE1:4 (Figure 4.6 curve *b*) but with changes in the peak positions. All the thermal transition temperatures observed are summarized in Table 4.3.

Table 4.3: Summary of nanocomposites phase transitions and melting heat of fusion

Material	**Thermal Phase transitions**				
	T_g (^{0}C)	T_c (^{0}C)	T_m (^{0}C)	$\Delta_{fusion}H$(J g^{-1})	T_e (^{0}C)
POMOE	-62.9	-9.7	14.5	47.3	-------
V_2O_5POMOE (1:0.5)	-23.3	-----	----	27.3	197.2
V_2O_5POMOE (1:1)	-65.5	-46.9	-5.4	10.1	110.9
V_2O_5POMOE (1:2)	-68.1	----	-3.1	28.2	115.9
V_2O_5POMOE (1:3)	-67.6	----	-1.6	38.1	116.8
V_2O_5POMOE (1:4)	-72.3	----	-0.4	40.5	127.3

The nanocomposites glass transition temperatures (Table 4.3) were found to be lower than that of POMOE, and it decreases with increasing amount of POMOE. The phase transition temperatures for V_2O_5POMOE1:0.5 was reproducible, but inconsistent with the trends observed in the other samples. Possible interpretation for this observation is that in V_2O_5POMOE1:0.5 all of POMOE chains are intercalated within the layered structure forming a rigid compound. The nanocomposites with higher molar ratios contain excess (un-intercalated) polymer, which contributes to the lowering of the glass transition temperature. The melting temperatures of the nanocomposites were lower than that of POMOE, and they increase with increasing amount of POMOE. The melting heat of fusion ($\Delta_{\text{fusion}}H$) is also shown to increase

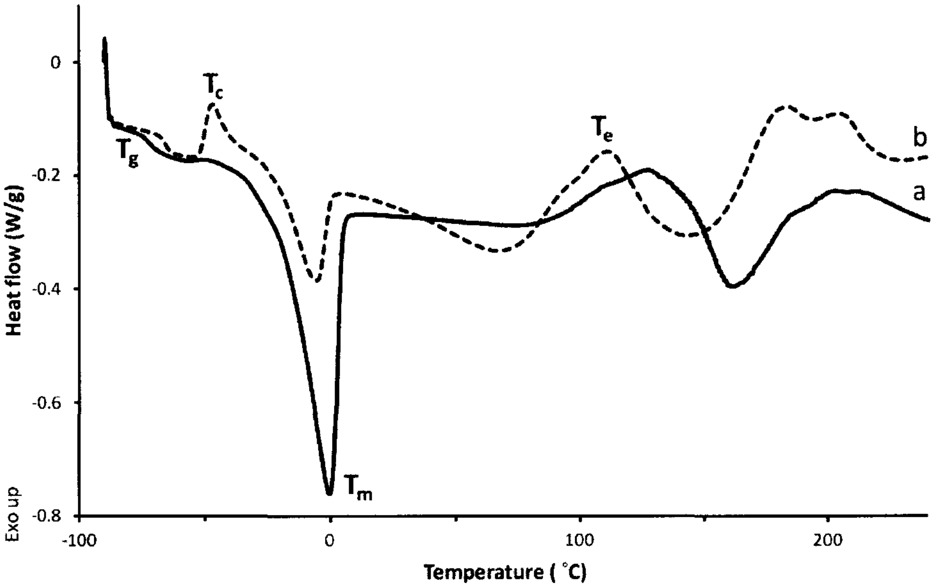

Figure 4.6: DSC of a) V_2O_5POMOE1:4 and b) V_2O_5POMOE1:1.

with increasing POMOE content and the values approach that of the pure polymer, 47 Jg^{-1}.

All nanocomposites show an exothermic phase transition above 110 °C. This phase transition is referred to as the blending temperature (T_e) i.e. the temperature when the POMOE-chains thermally blend with $V_2O_5nH_2O$ ribbons to form mechanically stable film. This interpretation was based on the fact that T_e is below the major decomposition temperatures, which is above 173 °C for all nanocomposites, and the materials obtained just above the T_e are mechanically stable films. The sharp endothermic peaks with well-defined baselines after the glass transition temperatures (Figure 4.6), confirms the presence of the polymer in the nanocomposites in comparison with the control samples (see Figure 4.7). The DSC control samples were a cast film of $V_2O_5nH_2O$, freeze-dried $V_2O_5nH_2O$, and freeze-dried V_2O_5MeOH. Figures 4.7 curve *a* and *b* show two broad endothermic overlapping peaks for the freeze-dried and the cast film of $V_2O_5nH_2O$, respectively. The broad peaks indicate the evaporation of the solvent/volatiles from the samples. The first peak corresponds to the evaporation

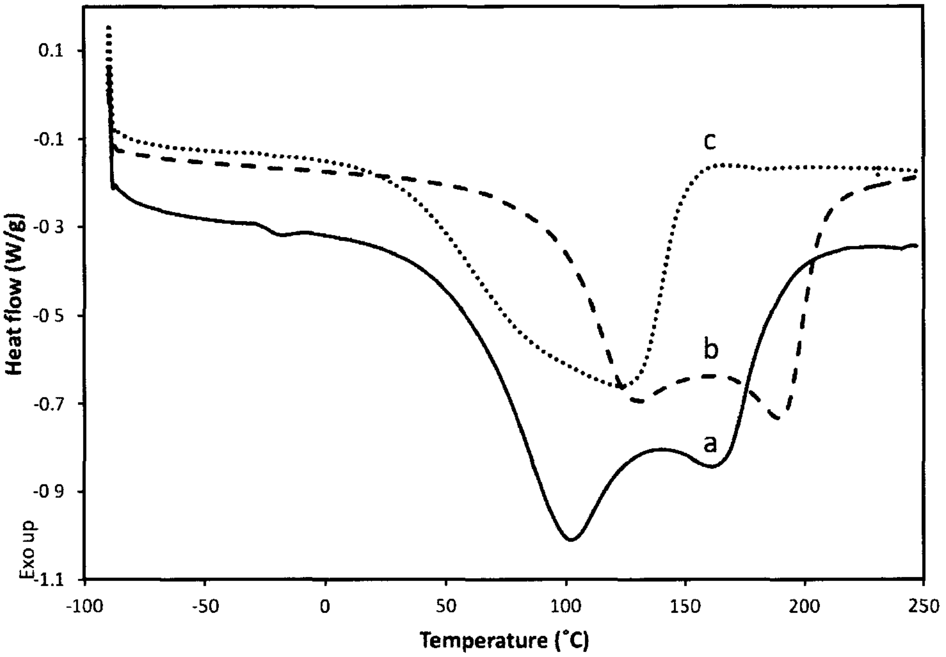

Figure 4.7: DSC of a) freeze-dried $V_2O_5nH_2O$, b) cast film $V_2O_5nH_2O$ and c) freeze-dried V_2O_5MeOH.

of loosely bound water molecules in $V_2O_5nH_2O$, while the second peak corresponds to the removal of the strongly bound water molecules.

It is important to note that for highly oriented samples (the cast films), the peaks are observed at higher temperatures compared to the randomly oriented (freeze-dried) samples. Therefore, higher orientation was associated to a compact packing of water molecules within the layers, hence needing more energy to evaporate from the samples. On the other hand, the DSC of V_2O_5MeOH (Figure 4.7 curve *c*) shows only one endothermic peak, which corresponds to the loss of methanol molecules. Figure 4.7 curve *c* also indicates that when methanol is added to $V_2O_5nH_2O$ it displaces the interlayer water molecules. This conclusion is supported by thermogravimetric analysis, Figure 4.5 curve *c*, which shows a one step weight loss process. X-ray diffraction also provides supporting evidence, which shows an interlayer expansion of 2.6 Å due to the intercalation of methanol.

The disparity in the decomposition temperatures between the DSC and TGA is due to the difference in the experimental set up. In TGA, the samples were placed on a platinum holder under direct gas (air or nitrogen) purge, whereas in DSC, the samples were sealed in aluminum cells and the measurements were performed under a nitrogen atmosphere.

4.1.4 Fourier transform infrared spectroscopy

Infrared spectroscopy was further used to characterize the nanocomposites. The IR spectra of the nanocomposite exhibited similar features. The absorption bands for POMOE, $V_2O_5nH_2O$, and V_2O_5POMOE1:2 and the major bond group assignments [89,93] are summarized in Table 4.4. The nanocomposites show all the diagnostic and finger-print vibrations for POMOE (e.g. C-H, C-O-C stretching and CH_2 rocking vibrations) in addition to a broad band at 3445 cm^{-1} due to OH bonds. The appearance of the broad band at 3445 cm^{-1} indicates the presence of OH bonds formed upon intercalation. This implies that the hydrogen atoms of POMOE are bonding with the oxygen atoms in $V_2O_5nH_2O$ *via* hydrogen bonds. The formation of hydrogen-bond networks improves the mechanical stability of POMOE and $V_2O_5nH_2O$. Mechanical stability was demonstrated by the formation of free standing films. The cast films can be easily peeled off the glass substrates by dipping in water (the peeling was facilitated by the use of soapy water).

It is also interesting to note that the C-H stretching vibration peak in pure POMOE occurs at 2870 cm^{-1}. However, this peak is split into two vibrations (2912 cm^{-1} and 2876 cm^{-1}), when the polymer is intercalated into the layered structure, consistent with the polymer being in a constrained environment. The V=O and C-O-C stretching vibrations overlap in the region (1010-1115) cm^{-1}. The presence of POMOE and $V_2O_5nH_2O$ diagnostic bands in the nanocomposites indicates that no significant structural disruptions to the polymer chains and the V_2O_5 layers upon

Table 4.4: A summary of FTIR bands for POMOE, $V_2O_5nH_2O$ and V_2O_5POMOE1:2.

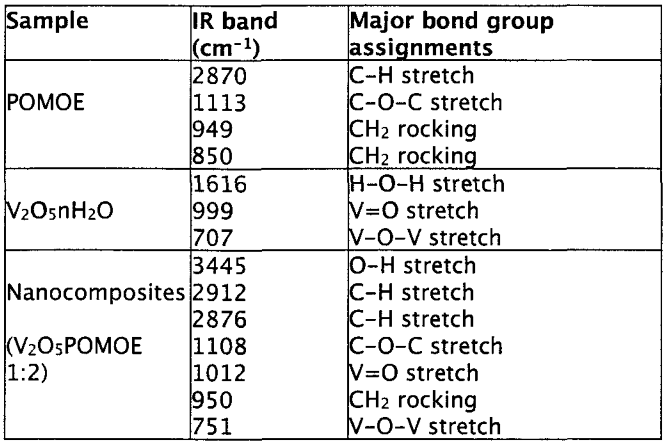

Sample	IR band (cm^{-1})	Major bond group assignments
POMOE	2870 1113 949 850	C-H stretch C-O-C stretch CH_2 rocking CH_2 rocking
$V_2O_5nH_2O$	1616 999 707	H-O-H stretch V=O stretch V-O-V stretch
Nanocomposites (V_2O_5POMOE 1:2)	3445 2912 2876 1108 1012 950 751	O-H stretch C-H stretch C-H stretch C-O-C stretch V=O stretch CH_2 rocking V-O-V stretch

intercalation. The vibrations band shifts observed in the nanocomposites suggest a geometric distortion of POMOE due to confinement within the V_2O_5 framework.[89,92]

4.1.5 Impedance spectroscopy

The impedance experiment involved applying an AC to the sample and measuring the real (Re Z) and imaginary (-Im Z) parts, of the resulting current. The impedance complex plane plots were semicircles for all samples, similar to plots for a simple parallel RC circuit. This model was used to fit the plots, with R being the resistance of an electrically conducting sample and C being the cable capacitance in parallel with it. As electrical conductors, the resistance is the real part of the curve when "-Im Z" part is zero at the lower frequency of the complex plot.[11] The resistance values from the impedance plots and the measured sample dimensions were used to calculate resistivity (ρ). The conductivity (σ) of the sample is the reciprocal of resistivity (ρ).

The calculated electrical conductivity results are shown in Figure 4.8. The straight lines on this graph of log(σ) as a function of inverse temperature are indicative of a thermally-activated conduction process, described by an equation of the form

$$\sigma(T) = \sigma_0 e^{-E/kT)} \tag{4.1}$$

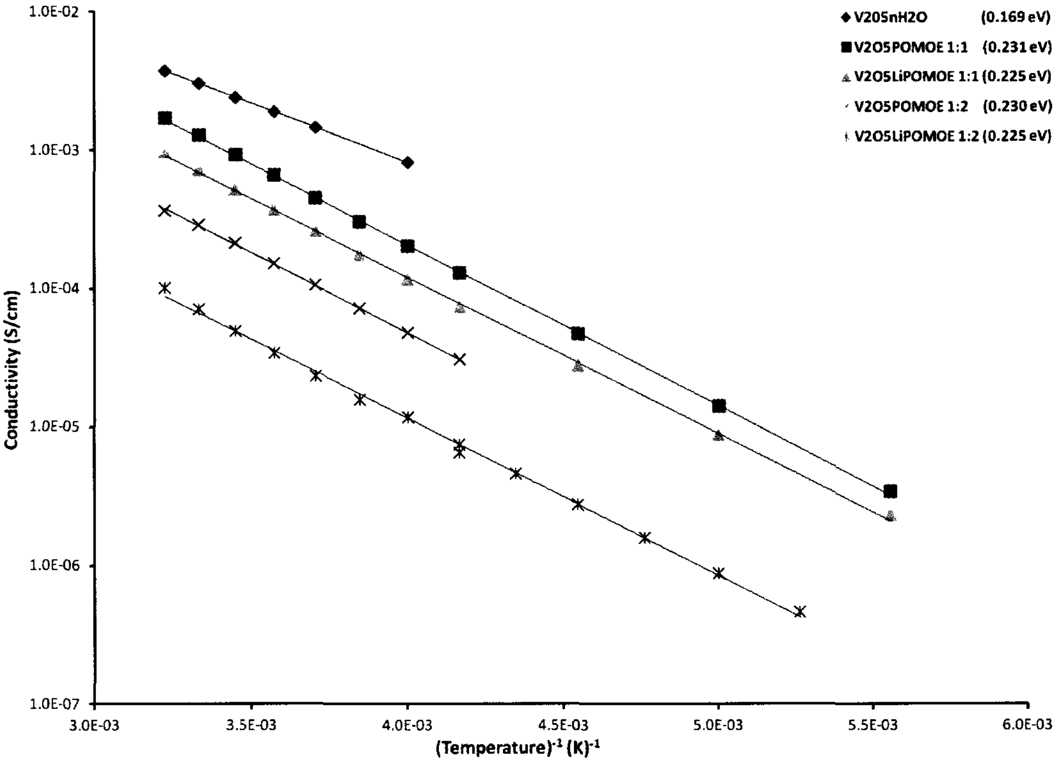

Figure 4.8: Conductivity-temperature relationship for $V_2O_5nH_2O$ and for nanocomposites with and without LiX.

where σ_0 is the pre-exponential constant and E is the activation energy or band gap for conduction (semiconductor band gap).

The activation energies were estimated from the slopes of the curves and the values are shown in Figure 4.8. The activation energy for the $V_2O_5nH_2O$ film was ≈ 0.17 eV, close to what was reported by Livage [41] (0.2 to 0.4 eV) and De *et al.* [94] (0.13 eV). The activation energies for nanocomposites with and without LiX were ≈ 0.22 eV and 0.23 eV, respectively. It is interesting to note that the polymer ratio used did not affect the activation energy, E, but changed the conductivity values. Increasing the amount of POMOE lowered the electrical conductivity of the nanocomposites. The decreased electronic conductivity upon intercalation of POMOE into $V_2O_5nH_2O$ would be due to the strong hydrogen-bonding within the nanocomposites, as well as the electrical insulating property of POMOE. Pristine $V_2O_5nH_2O$ film has the highest conductivity as shown in Figure 4.8. Although there were large systematic uncertainties (typically 40%) in the conductivity values due to difficulty in measuring the film thickness, the trends provide a clear relationship of conductivities as a function of temperature.

This Arrhenius-type behavior is typical for semiconducting materials. It was expected that by doping the nanocomposites with lithium salts, ions might replace electrons as the dominant charge carriers. That change would make these nanocomposites suitable for use as solid electrolytes in lithium ion batteries. However, the electrical conductivity was still large enough that the ionic conductivity could not be detected by our measurement technique. Studies are underway to investigate the effect of changing the LiX ratio.

A unique colour change was observed for some of these nanocomposites. This observation might be contributing to the conductivity properties of these materials. For example, before impedance testing V_2O_5POMOE cast films were red. Immediately after impedance measurements and dismounting the samples from the vacuum chamber they were observed to be completely green. After exposing the samples to the laboratory atmosphere for a few days the colour changed back to red. However, it was noticed that the sample-part which was trapped underneath the silver electrodes remained green. This is more likely because the trapped sample-part did not have direct exposure to air. This colour change phenomenon indicates that a chemical reaction occurred in the sample as a result of current flow during the impedance measurements. The green colour corroborates with the work done by Livage's group.[41] This evidence means that the conductivity (ionic and electronic) of the nanocomposites was compromised. It was noticed that dipping V_2O_5POMOE films in water changed their colour to green, but it was irreversible to red even after several days.

5 Vanadium Pentoxide Xerogel-Poly[oligo(ethylene glycol)oxalate]

5.1 Results and discussion

Intercalation of poly[oligo(ethylene glycol) oxalate] (POEGO) and POEGO-$LiCF_3SO_3$ complex into vanadium pentoxide xerogel ($V_2O_5nH_2O$) are reported for the first time. The effect of changing the polymer concentration on the interlayer expansion of the layered host was studied, and the optimal intercalation ratio was determined to be 1:2. The intercalates were characterized by powder X-ray diffraction, thermogravimetric analysis, differential scanning calorimetry, Fourier transform infrared spectroscopy techniques, and AC impedance spectroscopy.

5.1.1 X-ray diffraction

Successful intercalation of POEGO and Li-POEGO into $V_2O_5nH_2O$ and the identity of the as synthesized $V_2O_5nH_2O$ were confirmed by powder X-ray diffraction patterns. Figure 5.1 shows the diffraction patterns for $V_2O_5nH_2O$, V_2O_5MeOH, and V_2O_5POEGO1:1.

The interlayer spacing (d) for as synthesized $V_2O_5nH_2O$ was calculated to be 11.9 Å and n was determined from TGA to be 1.9 (lit.[35] d = 11.5 Å, n = 1.8).The d-space is depended on the amount of intercalated water molecules. The diffraction pattern for V_2O_5POEGO1:1 (Figure 5.1 curve *c*) showed a d-space of 20.4 Å, which corresponds to an interlayer expansion of 8.5 Å with respect to $V_2O_51.9H_2O$ (d = 11.9 Å). Other intercalates show similar features and their interlayer expansions are

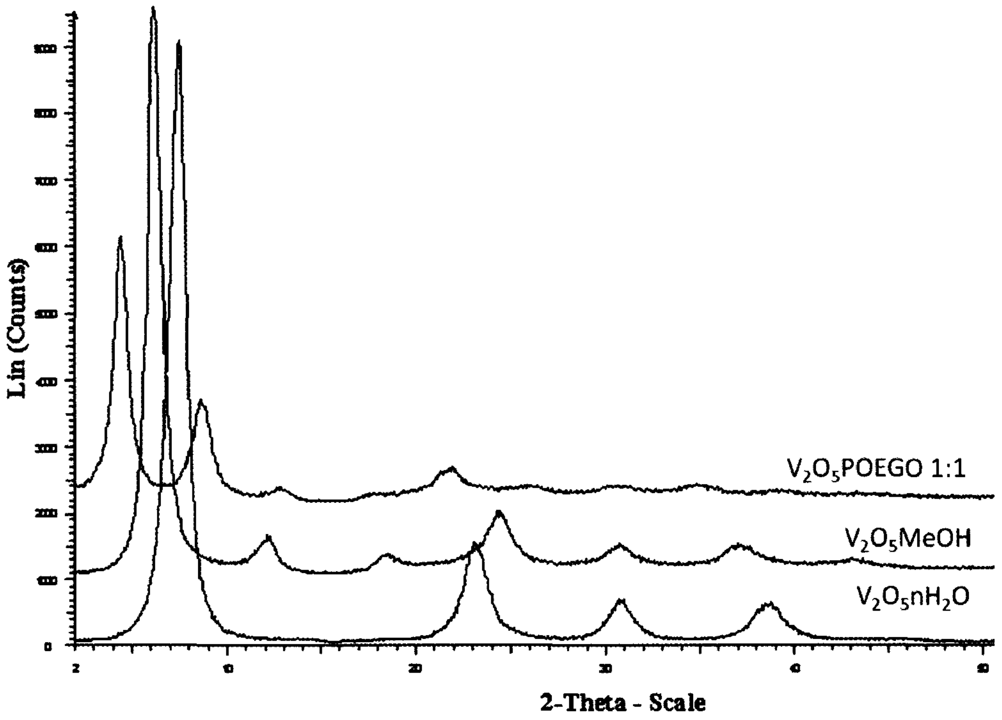

Figure 5.1: XRD of a) $V_2O_5nH_2O$, b) V_2O_5MeOH and c) V_2O_5POEGO1:1.

summarized in Table 5.1.'

The X-ray diffraction patterns of the nanocomposites show a complete intercalation of POEGO into the gallery space based on the absence of pristine $V_2O_5nH_2O$ phase. Further evidence of POEGO intercalation into $V_2O_5nH_2O$ is obtained through

Table 5.1: List of interlayer expansions and average crystallite size of the nanocomposites.

Materials (ratios)	Observed d-spacing (Å)	Expansion Δd-spacing (Å)	Average Crystallite size (Å)
$V_2O_5 1.9H_2O$	11.9	-----	73
V_2O_5MeOH	14.5	2.6	89
V_2O_5POEGO (1:0.5)	17.9	6.0	79
V_2O_5POEGO (1:1)	20.4	8.5	96
V_2O_5POEGO (1:2)	20.8	8.9	85
V_2O_5POEGO (1:3)	20.6	8.7	97
V_2O_5POEGO (1:4)	21.0	9.1	70

Note: f shows the fine powder phase and s shows the sticky mass phase.

comparison of the X-ray diffraction patterns to the control sample (V_2O_5MeOH), which show d-space increase. For example, V_2O_5POEGO1:1 has a d-space of 5.9 Å higher than V_2O_5MeOH. These observations are strong evidence that POEGO was actually intercalated into $V_2O_5nH_2O$. However, it is difficult to say whether methanol is co-intercalated with POEGO from the X-ray diffraction pattern alone. The X-ray diffraction patterns of the nanocomposites show only *(00l)* reflections, which is indicative of highly oriented materials.

Table 5.1 show that there was no significant increase in d-spacing as the amount of POEGO was increased. This observation means that the average interlayer expansion of 8.7 Å corresponds to the optimum loading of POEGO-chains into $V_2O_5nH_2O$. This finding corroborates with previous work where POEGO has been intercalated into other layered structures. For example, intercalation of POEGO into tin disulfide[72], and molybdenum disulfide[95] were reported with interlayer expansions of 8.7 Å and 8.6 Å, respectively. From these literature reports, the interlayer expansion was ascribed to a bilayer arrangement of POEGO-chains sandwiched between the host layers. Using similar arguments, the average interlayer expansion of 8.7 Å in this work corresponds to a bilayer conformation of POEGO-chains between the V_2O_5 ribbons.

For further information from X-ray diffraction patterns, the average crystallite size of the nanomaterials was calculated using the Scherrer equation (2.2). As shown in Table 5.1, there is no clear trend of the crystallite size with the amount of POEGO present in the nanocomposite. For example, the nanocomposite with mole ratio 1:3 shows the highest crystallite size while that with mole ratio 1:4 shows the least value.

All the nanocomposite mole ratios prepared, formed homogeneous solutions that were cast into thin films for X-ray diffraction studies. However, upon freeze-drying the solutions from mole ratio 1:3 and 1:4 separated into two solid-phases. One phase was a fine powder and the other phase was a sticky-mass. The two phases were characterized separately with the other techniques (TGA, DSC, and FTIR).

5.1.2 Thermogravimetric analysis

The thermo stability and stoichiometric composition of the nanocomposites was determined using TGA data. Figure 5.2 shows the decomposition profile (in air) for POEGO, V_2O_5MeOH, V_2O_5POEGO1:4 (the fine powder and the sticky mass). POEGO decomposes completely in air as shown in Figure 5.2 curve *d*. The control sample (V_2O_5MeOH) has the highest residue percentage of 89%, shown in Figure 5.2 curve *a*. The nanocomposites have a weight residue percentage that corresponds to the amount of $V_2O_5nH_2O$ present. A complete summary of thermogravimetric analysis of the nanocomposites in air is provided in Table 5.2

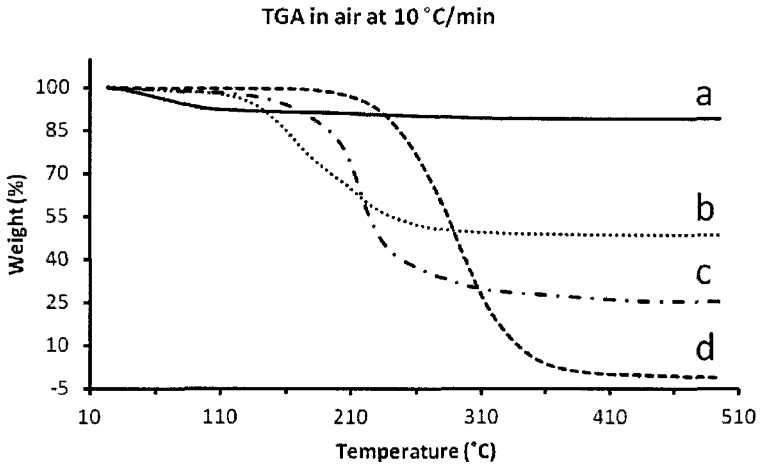

Figure 5.2: TGA of a) V_2O_5MeOH, b) V_2O_5POEGO1:4 fine powder c) V_2O_5POEGO1:4 sticky mass, and d) POEGO.

The thermogram of the control sample (Figure 5.2 curve *a*), shows a constant weight residue above 100 °C i.e. after the evaporation of methanol. Therefore, the weight loss processes above 100 °C for the nanocomposites is associated with the polymer decomposition. Increasing the amount of POEGO in the nanocomposites decreases the residue percentage due to the decreased concentration of $V_2O_5nH_2O$ as shown in Table 5.2.

Table 5.2: TGA profiles for POEGO, $V_2O_5nH_2O$, V_2O_5MeOH, and the nanocomposites.

Material		Decompositions in air		Residue (wt %)
Mole ratios used	Composition ratios	Weight (%)	Temp.(^oC)	
POEGO	--------------	100	291	0
$V_2O_5nH_2O$	$V_2O_5(H_2O)1.9$	10.3 , 2.5	49 , (321 , 364)	84.3
V_2O_5MeOH	$V_2O_5(MeOH)_{0.7}$	8.4	80	88.8
V_2O_5POEGO (1:0.5)	$V_2O_5(POEGO)_{0.1}(H_2O)_{0.8}$	22.3	285	72.2
V_2O_5POEGO (1:1)	$V_2O_5(POEGO)_{0.3}(H_2O)_{1.8}$	36.8	248	53.5
V_2O_5POEGO (1:2)	$V_2O_5(POEGO)_{0.6}(H_2O)_1$	55.7	204	40.2
V_2O_5POEGO (1:3) f	$V_2O_5(POEGO)_{0.6}(H_2O)_{0.7}$	59.0	(205, 254)	38.1
V_2O_5POEGO (1:3) s	$V_2O_5(POEGO)_{1.1}(H_2O)_{3.2}$	68.2	209	24.1
V_2O_5POEGO (1:4) f	$V_2O_5(POEGO)_{0.4}(H_2O)_{0.3}$	49.6	(195, 245)	48.6
V_2O_5POEGO (1:4) s	$V_2O_5(POEGO)_{1.2}(H_2O)_{0.6}$	72.9	260	25.5

Note: f shows the fine powder phase and s shows the sticky mass phase.

For the nanocomposites, which separated into two solid-phases, the fine powder phases (Figure 5.2 curve *b*) yielded a higher residue percentage compared to the corresponding sticky-mass phases (Figure 5.2 curve *c*). This data means that the sticky phases have higher polymer component than the fine powder. Interestingly, the residue percentages of the sticky phases are similar having weight percentages of 24.1% and 25.5% for $V_2O_5POEGO1:3$ and $V_2O_5POEGO1:4$, respectively. On the other hand, the corresponding residue percentages of the fine powders are significantly different, having a difference of more than 10%. This observation means that during the phase separation, the composition of the sticky-phase is independent of the amount of $V_2O_5nH_2O$ or POEGO used.

The decomposition profiles can be divided into three stages. In stage I (<120 °C), the weight loss corresponds to the evaporation of water/solvent. The weight loss in stage I vary randomly with no correlation to the amount of polymer used. In stage II (120 - 400 °C), the weight loss corresponds to the decomposition of the polymer. At this stage, the percentage weight loss is directly proportional to the amount of the polymer present in the nanocomposite. And finally, stage III (>400 °C) corresponds to the residue which has a constant weight percentage. The residue (yellow in colour) was identified with XRD to be orthorhombic V_2O_5 crystals.

The composition ratios were calculated based on the mass loss at each of the first two stages, the mass of the residue, and the corresponding molecular weight of the compound.[1] A complete list of calculated compositions for all nanocomposites is provided in Table 5.2. There is no clear correlation (from Table 5.2) between the experimental mole ratios and the calculated composition ratios from TGA. A possible explanation for this observation is due to the solid-phase separations, which were not experimentally controllable hence; the homogeneity of the samples was affected.

5.1.3 Differential scanning calorimetry

DSC study provides important information on thermal transitions occurring in the nanocomposites. The significant transitions observed for these nanocomposites were the glass transition temperature (T_g) and the blending temperature (T_e). Figure 5.3 illustrates the results found for V_2O_5POEGO1:1, V_2O_5POEGO1:4 sticky-phase, and V_2O_5POEGO1:4 fine powder-phases, respectively. Other nanocomposites showed similar thermal transitions. A complete list of glass transitions and blending temperatures are summarized in Table 5.3.

All samples showed negative sloping baselines after the glass transition temperature similar to Figure 5.3 curve *a* and *b*, except for the sticky-phases, which have a horizontal baselines similar to Figure 5.3 curve *c*. The negative sloping baseline indicates the slow heat flow to the sample, which may correspond to the energy used to vaporize volatiles from the samples evaporation. The horizontal baseline displayed by the sticky-phase means that the sample and the reference cell are in thermodynamic

---

[1] For illustration, the mass loss at stage I, stage II, and the mass of the residue (stage III) were assumed to correspond to water, POEGO, and V_2O_5, respectively. The moles of water, POEGO and V_2O_5 were calculated for each sample. Then the mole ratios were expressed with respect to the moles of V_2O_5 (e.g. the composition for V_2O_5POEGO1:1 was determined to be $V_2O_5(POEGO)_{0.3}(H_2O)_{1.8}$).

Table 5.3: DSC thermal transitions for POEGO and the nanocomposites.

Materials (mole ratio)	Phase transitions		ΔT (T_e-T_g)
	T_g (°C)	T_e (°C)	
POEGO	-52.2	----	----
V_2O_5POEGO (1:1)	-25.9	99	124.9
V_2O_5POEGO (1:2)	-25.2	108	133.2
V_2O_5POEGO (1:3)f	-30.4	115	145.4
V_2O_5POEGO (1:3)s	-35.3	113	148.3
V_2O_5POEGO (1:4)f	-30.0	115	145.0
V_2O_5POEGO (1:4)s	-31.6	116	147.6

equilibrium. This observation is characteristic for amorphous and flexible materials.[83] The blending temperature being below the decomposition temperature (<200 °C) means that thin films can be obtained by hot pressing the fine powder or the sticky-mass up to 100 °C, without any decomposition or damage.

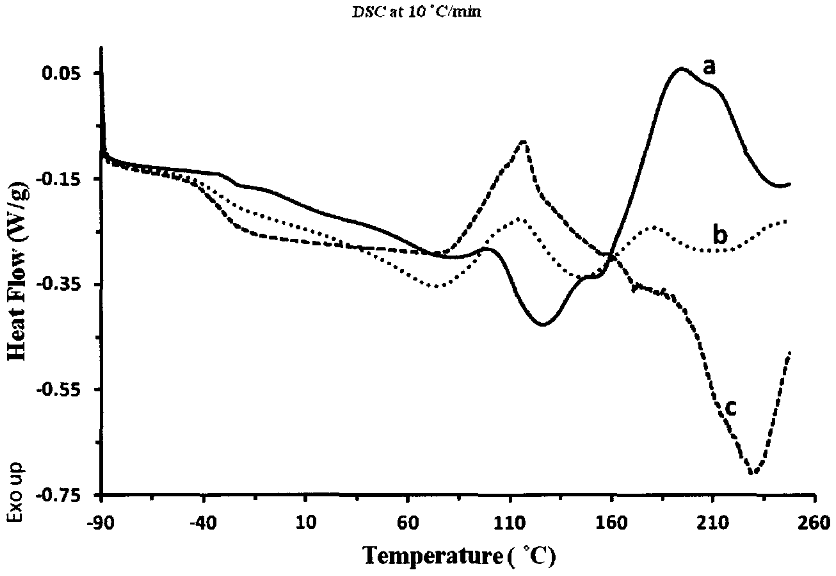

Figure 5.3: DSC of a) V_2O_5POEGO1:1, b) V_2O_5POEGO1:4 fine powder and c) V_2O_5POEGO1:4 sticky mass.

The DSC comparison between POEGO and V_2O_5POEGO1:4 sticky-mass phases under similar conditions are shown in Figure 5.4. It is important to note that the sticky-phases did not show any crystallization or melting thermal transitions between the glass transition and the blending temperatures. This observation means that the sticky-mass phases are amorphous and flexible between the glass transition and the blending temperatures. This is a significant finding because amorphous solids are known to be good ionic conductors than crystalline solids. In addition, the stickiness improves the binding ability of the materials, making the nanocomposites good candidates for solid-electrolyte and/or cathode materials for lithium/Li-ion batteries.

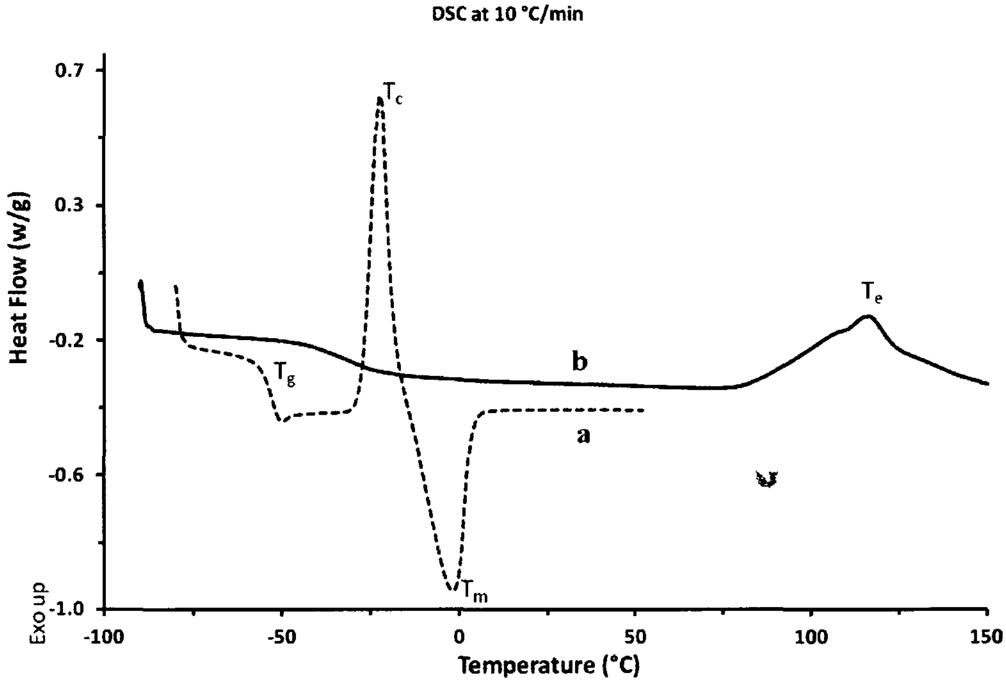

Figure 5.4: DSC comparison for a) POEGO and b) V_2O_5POEGO1:4 sticky phase.

The temperature gap (ΔT) between T_g and T_e was calculated for each sample and is shown in Table 5.3. The glass transition temperatures of the nanocomposites are higher than that of pure POEGO (Table 5.3) because the nanocomposites are more rigid than POEGO hence are easily turned into the glassy state.

5.1.4 Fourier transform infrared spectroscopy

Fourier transform infrared spectroscopy was used to investigate the type of chemical bonds present in the nanocomposites in comparison to POEGO and pristine $V_2O_5nH_2O$. Infrared spectra for all nanocomposites exhibit similar features as shown in Figure 5.5. The infrared band assignments were as follows: POEGO ν_{max}/cm^{-1} 2872w, 952 and 861 (CH), 1770s and 1745s (COCO) and 1115s (C-O-C); $V_2O_5nH_2O$ ν_{max}/cm^{-1} 1616 (HOH), 999 (V=O) and 707 (V-O-V); and a typical nanocomposite V_2O_5POEGO1:1 ν_{max}/cm^{-1} 2867 and 941 (CH), 1623 (COCO), 1082, 1021 and 986 (C-O-C and V=O).

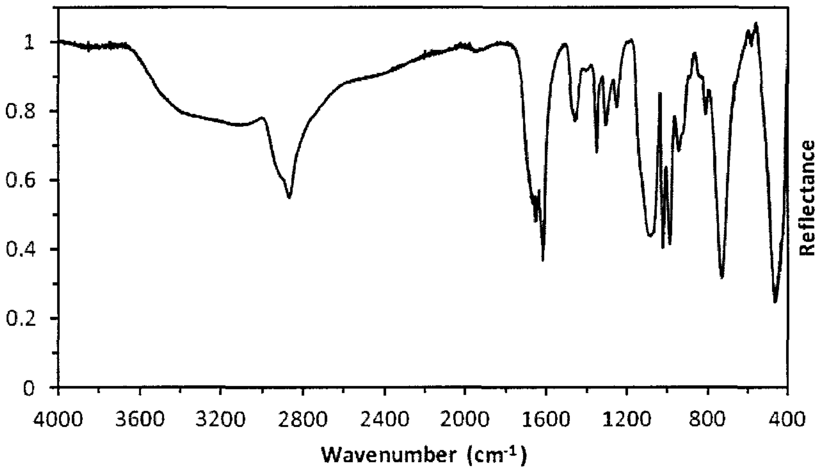

Figure 5.5: FTIR spectra for a typical V_2O_5POEGO (1:1) nanocomposite.

It is important to note that comparison of the infrared spectra for $V_2O_5nH_2O$ among various literature reports is complicated due to the distinct structural differences associated with the methods of $V_2O_5nH_2O$ preparation, and the aging period of the precursor solutions. In general[96], the characteristic V=O stretching absorption bands are found within the 950-1020 cm^{-1} range; while the bridging V-O-V stretching absorption bands usually occur between 700 and 900 cm^{-1}. The IR bands below 600 cm^{-1} correspond to either edge sharing V-O stretching or bridging V-O-V deformation vibrations.

The absorption bands for C=O and V=O were significantly perturbed in the nanocomposites, an indication for a chemical reaction between POEGO and $V_2O_5nH_2O$ during intercalation. However, the presence of bands at 2867 cm^{-1}, 1082 cm^{-1}, 986 cm^{-1}, and 1021 cm^{-1} confirms that the structure of the parent polymer and that of the layered structure are retained to some degree in the nanocomposites. It is not conclusive as to what kind of new chemical bonds are formed. The C-H stretching vibrations for POEGO shifted from 2872 cm^{-1} to between 2867 cm^{-1} and 2845 cm^{-1} in the nanocomposites. This band shift provides the evidence of an interaction between the polymer and the layered structure.

5.1.5 Impedance spectroscopy

The impedance experiment involved applying an AC to the sample and measuring the real and imaginary parts, of the resulting current. The impedance complex plots for Li-POEGO, V_2O_5POEGO1:1 and the equivalent circuit fitting curve for Li-POEGO (an ionic conductor) are shown in Figure 5.6. Ionic conductivity was observed only in the Li-POEGO sample. The plots for all nanocomposites were semicircles, similar to plots for a simple parallel RC circuit (electronic conductors). This model was used to fit the plots, with R being the resistance of an electrically conducting sample and C being the cable capacitance in parallel with it. For electrical conductors, the resistance of the sample is the real part of the impedance curve when the imaginary part is zero at the lower frequency (frequency decreases a long the x-axis from left to right) of the complex plot.[11] Therefore, the resistance of the samples was obtained directly from the impedance plots then combined with the sample dimensions to determine the resistivity (ρ), conductivity (σ) is the inverse of resistivity (ρ).

The calculated conductivity values at different temperatures were graphed as shown in Figure 5.7. The electrical conductivity of $V_2O_5nH_2O$ xerogel decreased

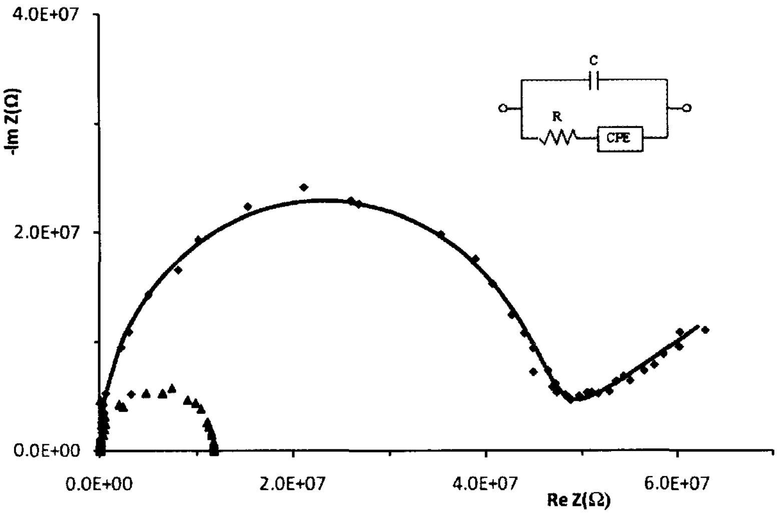

Figure 5.6: Complex plot at 310 K of Li-POEGO (blue diamonds) and V_2O_5POEGO1:1 (black triangles). The equivalent circuit fitting model (insert) was used to fit the ionic conductivity (the curve) for Li-POEGO data.

upon intercalation of POEGO. This is consistent with the fact that POEGO is an electrical insulator. Intercalation of Li-POEGO did not result in any measurable ionic conductivity. With the impedance technique used in this work, if the ionic conductivity is much smaller than the electrical conductivity, it will not be detected. Therefore, if these materials have any ionic conductivity at all, it must be well below 10^{-5} S/cm at 310 K. The electrical conductivity increases with increasing temperature, a trend known for semiconductors. A semiconductor is a material with conductivity between that of a conductor and an insulator. Semiconductors are known to have no free electrons in the crystalline state, and in principle are expected to be insulators, but as the temperature is increased, some of the bonded electrons are liberated and become free to move through the crystal lattice and thus conduct electricity.[11] The temperature dependence of conductivity satisfies an Arrhenius type of conduction(equation 4.1).[94]

The poor precision of the conductivity measurement values for $V_2O_5nH_2O$ among various literature reports and in comparison to those reported in this work are due

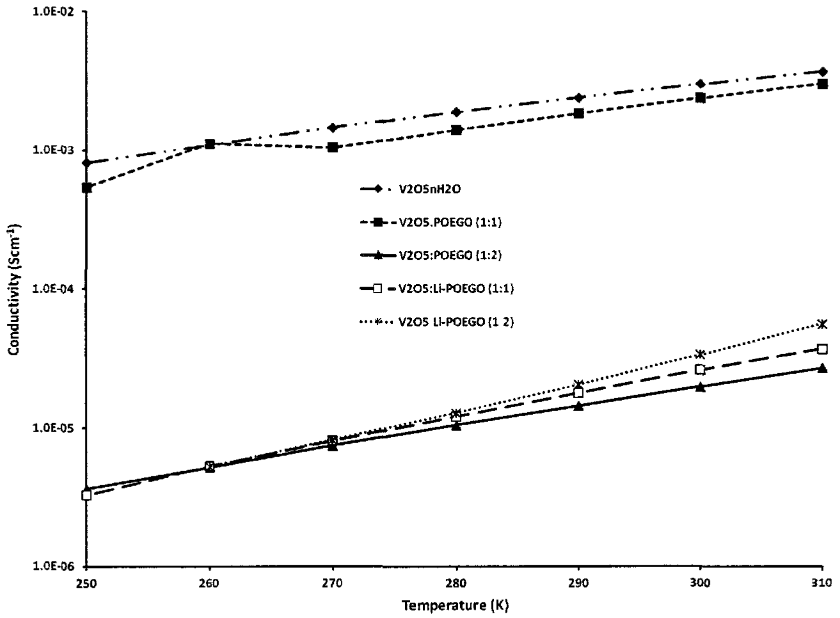

Figure 5.7: Conductivities of $V_2O_5nH_2O$, V_2O_5POEGO1:1, and V_2O_5POEGO1:2 (with and without LiX).

to many variable experimental parameters, such as the state of vanadium reduction, the relative humidity of the atmosphere, the age of the gel, the sample film dimensions and the direction of conductivity measurements. All these parameters affect the conductivity of $V_2O_5nH_2O$. For example, due to the layered structure of the $V_2O_5nH_2O$, its conductivity can be four orders of magnitude larger when measurements are performed in a direction parallel to the ribbons rather than perpendicular to the ribbons.[41] The conductivities reported in this work were measured parallel to the ribbons, i.e. the current flow was along the film, parallel to the substrate.

6 Vanadium Pentoxide Xerogel-Poly[bis-(2-methoxyethoxyethoxy)phosphazene]

6.1 Results and discussion

The intercalation of poly[bis-(2-methoxyethoxyethoxy)phosphazene] (MEEP) and $LiCF_3SO_3$-MEEP (Li-MEEP) complex into $V_2O_5nH_2O$ xerogel at room temperature is reported for the first time. A series of intercalates were prepared to study the effect of changing the polymer concentration on the interlayer expansion, and to determine the optimal intercalation ratio. The intercalates with lower MEEP concentration showed electronic conductivity while those with higher MEEP concentration showed mixed (electronic and ionic) conductivity, which were in the range 10^{-4} to 10^{-6} Scm^{-1} at 35 °C. The nanocomposites were found to be dry i.e. they did not have any structural or adsorbed water molecules, as confirmed by thermogravimetric analysis. Therefore, the nanocomposites have high potential to be used as cathodes in a "vanadium-lithium" battery. Characterization of the new materials was done by powder X-ray diffraction, thermogravimetric analysis, differential scanning calorimetry, infrared spectroscopy, scanning electron microscopy, and energy-dispersive X-ray spectroscopy and elemental analysis. Conductivity properties of the nanocomposites were investigated using AC impedance spectroscopy.

6.1.1 X-ray diffraction

X-ray diffraction technique was mainly used to probe the successful intercalation of MEEP into $V_2O_5nH_2O$ and the identity of the as synthesized $V_2O_5nH_2O$. Detailed discussion on the identity of the as synthesized $V_2O_5nH_2O$ has been reported elsewhere.[97] The XRD patterns of $V_2O_5nH_2O$ xerogel, V_2O_5MEEP1:1, and V_2O_5MEEP1:3 are shown in Figure 6.1. Other nanocomposites show similar features. A summary of the XRD data for all nanocomposites prepared is provided Table 6.1.

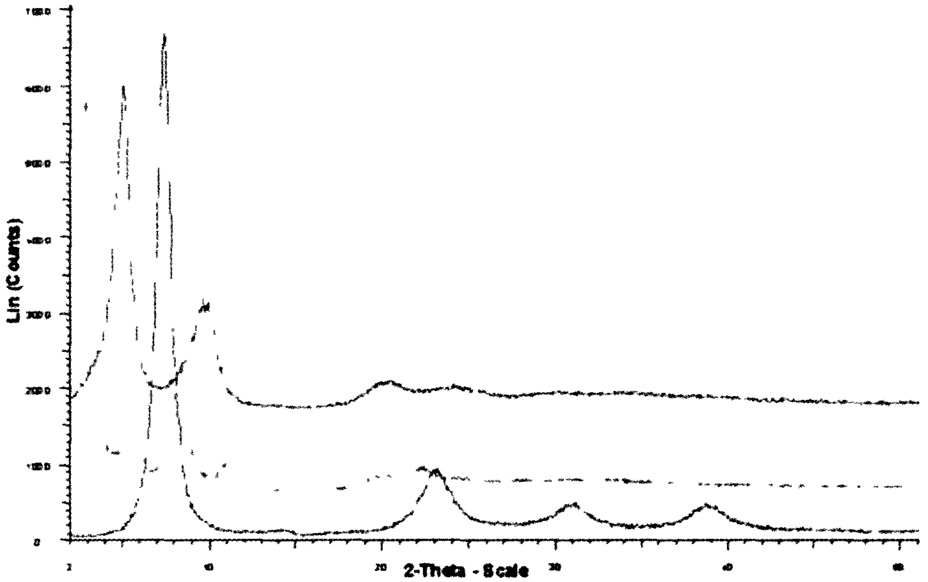

Figure 6.1: XRD for a) $V_2O_5nH_2O$, nanocomposite with mole ratio b) 1:1 and c) 1:3.

The XRD patterns of the nanocomposites show complete intercalation of MEEP into $V_2O_5nH_2O$, as judged by the absence of diffraction peaks of the pristine layered structure. Only (*00l*) reflections are observed which is indicative of highly oriented materials. It is clear from the diffraction patterns that increasing the amount of MEEP increases the net interlayer expansion. For example, the interlayer expansion for increasing the mole ratio from 1:1 to 1:2 is from 5.9 Å to 18.2 Å, respectively. However, there is no significant interlayer expansion when changing the mole ratio from 1:2 (18.2 Å) to 1:3 (19.8 Å). This observation indicates that an average interlayer

Table 6.1: XRD summary of interlayer expansions and average crystallite sizes of the nanocomposites.

Materials (mole ratios)	Observed d-spacing (Å)	Expansion Δd-spacing (Å)	Average Crystallite size(Å)
$V_2O_5nH_2O$	11.9	-----	73
V_2O_5MEEP (1:0.5)	17.9	6.0	79
V_2O_5MEEP (1:1)	17.8	5.9	83
V_2O_5MEEP (1:2)	30.1	18.2	138
V_2O_5MEEP (1:3)	31.7	19.8	132

expansion of 19.0 Å, corresponds to the optimum loading of MEEP into $V_2O_5nH_2O$.

The peak width of the diffraction peaks was observed to decrease with increasing amount of MEEP. Usually the peak width of a layered structure increases with increasing amount of an intercalated amorphous polymer due to a decrease in the crystallinity of the nanocomposite.[97] Therefore, this observation was opposite to what was expected: the crystallinity increased with increasing amount of MEEP in the V_2O_5 ribbons. To gain further insight, the average crystallite size of the nanocomposites was calculated using the Scherrer equation. The average crystallite size increased with increasing amount of intercalated MEEP as shown in Table 6.1. The increased crystallite size with increasing amount of MEEP is an interesting phenomenon, but is not currently well-understood. However, it does support the fact that a chemical reaction took place where the geometrical orientation of MEEP is strongly perturbed during the intercalation process.

6.1.2 Thermogravimetric analysis

Thermogravimetric analysis was used to further characterize the nanocomposites. The decomposition profiles (in air) of MEEP, $V_2O_5nH_2O$, V_2O_5MEEP1:1, and V_2O_5MEEP1:3 are shown in Figure 6.2. Other samples show similar features. A complete summary of the decomposition profiles (in air) of all nanocomposites, pure MEEP, and pristine $V_2O_5nH_2O$ are provided in Table 6.2. The decomposition profiles show that the nanocomposites do not exhibit any weight loss below 100 °C with the exception of one sample. The nanocomposite with mole ratio 1:0.5 shows a weight loss of 2.6% at around 40 °C. This weight loss corresponds to un-displaced water molecules due to insufficient amount of the polymer used. The absence of weight loss below 100 °C for the nanocomposites with mole ratio of 1:1 and higher ratios indicates that all the water molecules in $V_2O_5nH_2O$ are completely displaced upon intercalation of MEEP, and that the nanocomposites do not contain adsorbed water molecules or volatiles. This is a significant finding because the presence of water molecules in $V_2O_5nH_2O$ is one of the challenges hindering its use as an electrode material in a battery assembly. The V_2O_5MEEP nanocomposites have the advantage of being water free, thus enabling their handling in a moisture-free and air-sensitive environment, such as a dry box during battery assembly.

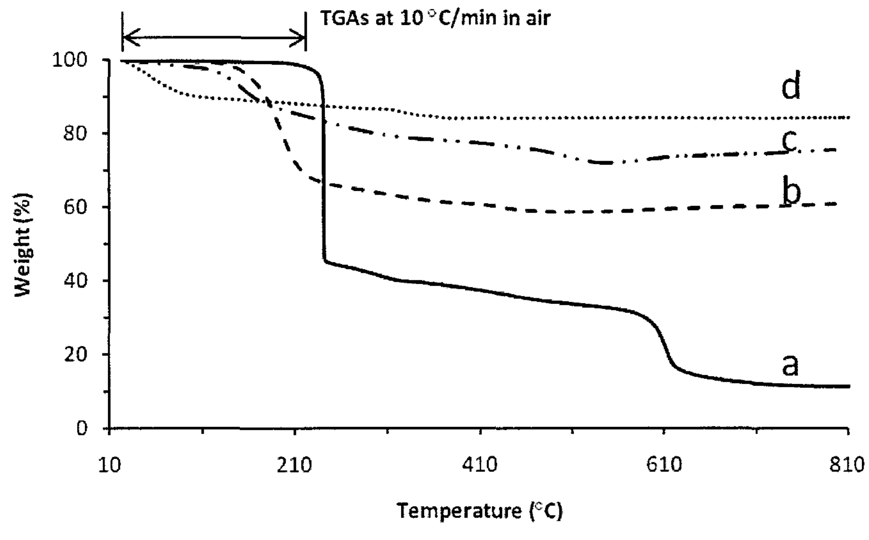

Figure 6.2: TGA for a) MEEP b) V_2O_5MEEP1:3 c) V_2O_5MEEP1:1 d) $V_2O_5nH_2O$.

The thermo-oxidative stability (in air) of MEEP is up to around 200 °C as shown in Figure 6.2 curve *a*. The decomposition of MEEP from the nanocomposites occurs

Table 6.2: TGA data of MEEP, $V_2O_5nH_2O$ and the nanocomposites in air.

Materials (mole ratios)	Decompositions in air		Residue (wt %)
	Weight (%)	Temp.(°C)	
MEEP	60 , 21	242, 613	11
$V_2O_5nH_2O$	10.3 , 2.5	49 , (321 , 364)	84.3
V_2O_5MEEP (1:0.5)	2.6 , 15.9, 3.7	40 , 161, 374	77.9
V_2O_5MEEP (1:1)	22.6, 4.9	153, 417	71.6
V_2O_5MEEP (1:2)	32.8, 3.6	180, 433	58.2
V_2O_5MEEP (1:3)	34.7, 2.3	194, 426	58.8

at lower temperatures as shown in the region indicated by the arrow in Figure 6.2, an indication that vanadium pentoxide acts as a combustion catalyst of the polymer. The residue percentage weights of the nanocomposites decrease with increasing amount of MEEP due to the dilution of the layered structure. TGA could not be used to calculate the composition of the intercalation compounds for the following reasons. As shown in Table 6.2, the decomposition of MEEP is incomplete, producing a residue of 11% by mass, which is derived from the inorganic (PNP) part of the polymer. In addition, the identity of this residue is not known. Furthermore, bubbling was observed during the intercalation of MEEP into $V_2O_5nH_2O$ xerogel, suggesting that the structure of the polymer may have been compromised.

6.1.3 Differential scanning calorimetry

Thermal transitions occurring in the nanocomposites were investigated using differential scanning calorimetry. The DSC spectra for V_2O_5Li-MEEP 1:1, V_2O_5MEEP1:2, and V_2O_5Li-MEEP1:3, are shown in Figure 6.3. Other samples show similar features. The glass transition temperature (T_g) for MEEP is below -80 °C. Upon intercalation of MEEP into $V_2O_5nH_2O$ xerogel, the T_g shifts to higher temperatures. For example, for the V_2O_5MEEP 1:1 and V_2O_5Li-MEEP 1:3 the T_g is at -23 °C and -60 °C, respectively. The shifting of T_g to higher temperatures provides evidence of an increase in the rigidity of the nanocomposites, and is also supporting evidence that the polymer is, in fact, intercalated. The DSC spectrum for the nanocomposite with mole ratio 1:2 is reproducible but does not show any noticeable T_g either with or without LiX. A possible explanation for this observation is that the 1:2 mole ratio is the optimum intercalation ratio in which all of the MEEP is intercalated into the xerogel. This interpretation is supported by the following observations. First, the sample with 1:2 ratio is a fine powder. Second, the sample with mole ratio 1:3 shows the presence of a T_g, which indicates that there is excess (externally lying) MEEP in the higher ratio nanocomposites. Finally, the 1:2 ratio is inferred to be the optimum intercalation ratio, since the interlayer expansion is not significant when the ratio is increased to 1:3; an increase of only 1.6 Å is observed.

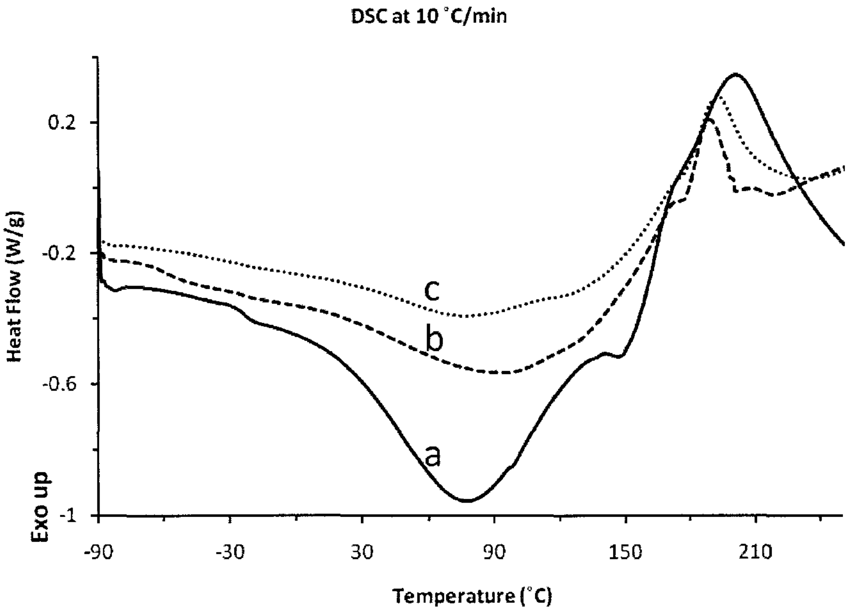

Figure 6.3: DSC for a) V_2O_5Li-MEEP1:1 b) V_2O_5Li-MEEP1:3 c) V_2O_5MEEP1:2.

The nanocomposites display a negative sloping baseline. This indicates a gradual heat flow into the sample. On the other hand, pure MEEP has a horizontal baseline indicating that it is at thermal equilibrium with the reference cell (empty aluminum pan). The nanocomposites degrade between 190°C and 204°C, as shown by the exothermic peaks in Figure 6.3. This interpretation is supported by thermogravimetric analysis, which shows the decomposition of the polymer at similar temperatures (see Figure 6.2).

6.1.4 Fourier transform infrared spectroscopy

Fourier transform infra-red (FTIR-ATR) spectroscopy was used to investigate the type of chemical bonds present in the nanocomposites, pure MEEP and pristine $V_2O_5nH_2O$. The infrared spectra for MEEP and V_2O_5MEEP1:2 are shown in Figure 6.4. Other nanocomposites show similar features to that of V_2O_5MEEP1:2. A summary of the major infrared bands observed and their assignments [76,98,99] for MEEP, $V_2O_5nH_2O$, and V_2O_5MEEP1:2 are provided in Table 6.3.

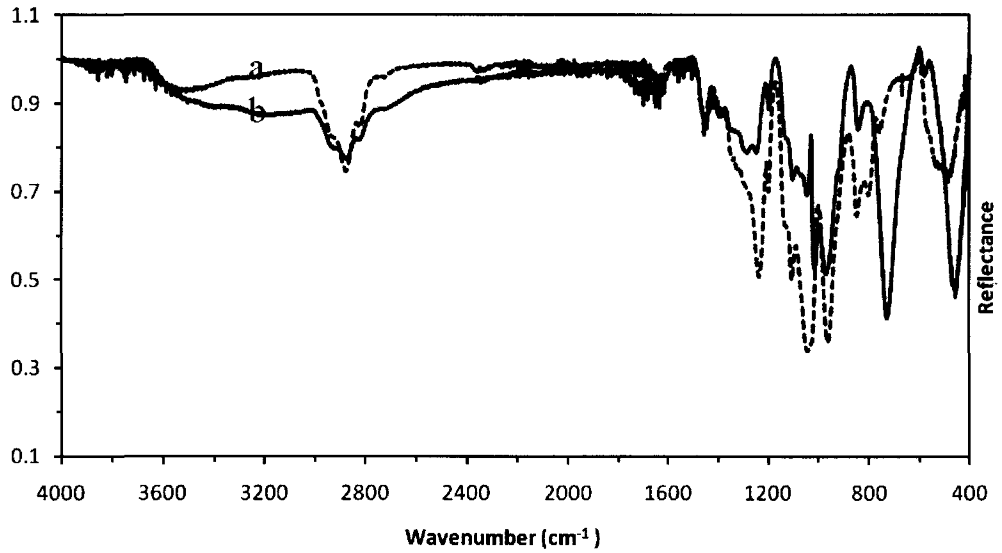

Figure 6.4: FTIR for a) MEEP and b) V_2O_5MEEP1:2.

The significant difference between the infrared spectra for MEEP and that of the nanocomposites is the splitting and shifting of the PNP band (1237 cm^{-1}) in MEEP into two bands, one at 1288 cm^{-1} and the other at 1251 cm^{-1} in the nanocompos-

Table 6.3: FTIR band assignments for MEEP, $V_2O_5nH_2O$, V_2O_5MEEP1:2, and V_2O_5LiMEEP1:2.

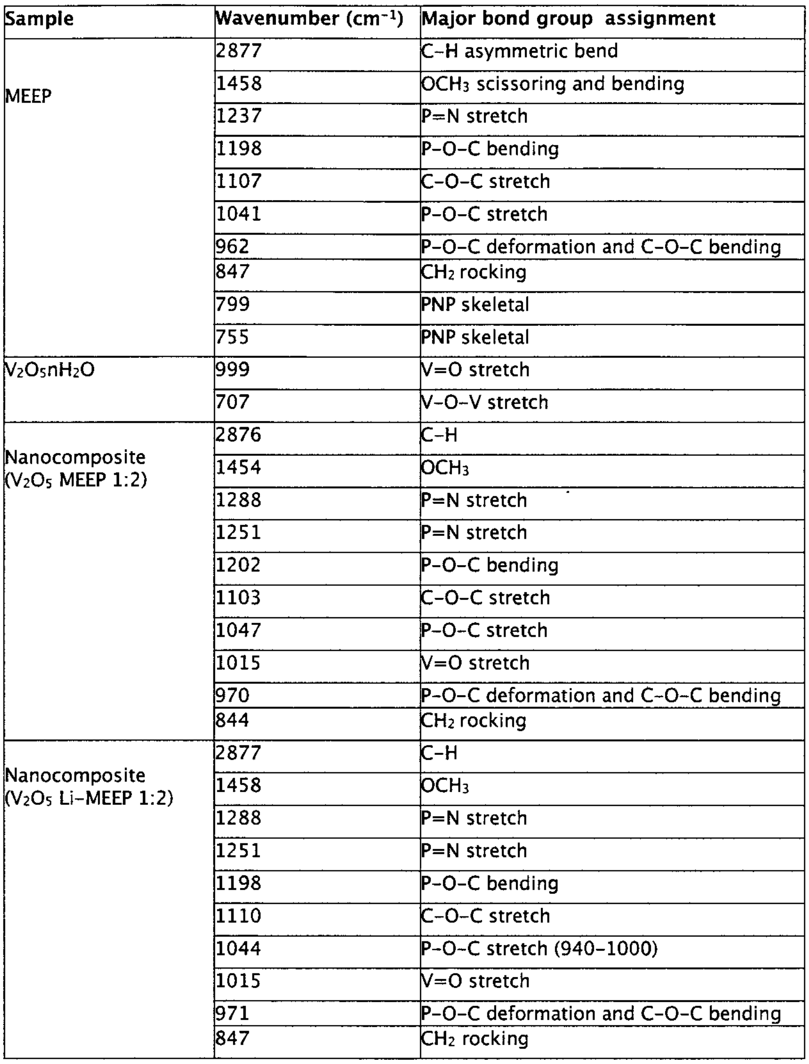

Sample	Wavenumber (cm^{-1})	Major bond group assignment
MEEP	2877	C-H asymmetric bend
	1458	OCH_3 scissoring and bending
	1237	P=N stretch
	1198	P-O-C bending
	1107	C-O-C stretch
	1041	P-O-C stretch
	962	P-O-C deformation and C-O-C bending
	847	CH_2 rocking
	799	PNP skeletal
	755	PNP skeletal
$V_2O_5nH_2O$	999	V=O stretch
	707	V-O-V stretch
Nanocomposite (V_2O_5 MEEP 1:2)	2876	C-H
	1454	OCH_3
	1288	P=N stretch
	1251	P=N stretch
	1202	P-O-C bending
	1103	C-O-C stretch
	1047	P-O-C stretch
	1015	V=O stretch
	970	P-O-C deformation and C-O-C bending
	844	CH_2 rocking
Nanocomposite (V_2O_5 Li-MEEP 1:2)	2877	C-H
	1458	OCH_3
	1288	P=N stretch
	1251	P=N stretch
	1198	P-O-C bending
	1110	C-O-C stretch
	1044	P-O-C stretch (940-1000)
	1015	V=O stretch
	971	P-O-C deformation and C-O-C bending
	847	CH_2 rocking

ites. Similarly, the doublet PNP skeletal vibrations of MEEP at 799 cm^{-1} and 755 cm^{-1} are replaced with a strong sharp band at 728 cm^{-1} in the nanocomposites. The other noticeable difference is the presence of a band at 1015 cm^{-1} in the nanocomposites, which is absent in pure MEEP. This band corresponds to the V=O stretching vibration in the V_2O_5 portion of the nanocomposite which has been shifted to a higher wavenumber in comparison to pure xerogel which shows a vibration peak at 999 cm^{-1}. This upward shift in wavenumber provides evidence that the MEEP and the xerogel are interacting with each other. It is interesting to note that the C-H, C-O-C stretching and OCH_3 scissoring bands in MEEP are not significantly shifted in the nanocomposites. This observation suggests that the chemical environment of the polymer is not affected upon intercalation. No significant shifts in wavenumbers are observed in the IR spectrum of the intercalated product of LiMEEP into the xerogel.

6.1.5 Scanning electron microscopy-energy dispersive X-ray spectroscopy

Scanning electron microscopy equipped with energy-dispersive X-ray spectroscopy (EDS) was used to obtain information on the morphology and elemental composition of the materials. The morphology of $V_2O_5nH_2O$ xerogel before and after intercalation with MEEP changed from a sheet-like structure to a smooth uniform surface as shown in Figure 6.5.

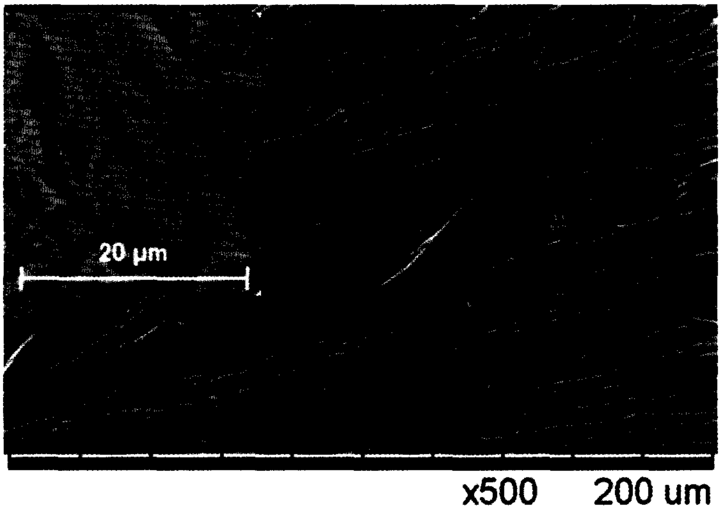

Figure 6.5: SEM image for $V_2O_5nH_2O$ film and V_2O_5MEEP1:1 (insert)

EDS was used to provide semi-quantitative information of the elements present in the nanocomposites. The EDS analysis for MEEP, $V_2O_5nH_2O$, V_2O_5Li-MEEP1:2, V_2O_5MEEP1:3, and V_2O_5Li-MEEP1:3 are shown in Figure 6.6. It is important to note that the EDS system used was not capable of detecting light elements below atomic number 7. For this reason hydrogen and Li-ions although present in the samples are not shown in Figure 6.6. Although EDS did not detect any nitrogen in the nanocomposites, quantitative elemental analysis[1] proved that nitrogen was present.

Bubbling was observed during the intercalation reaction and was thought to be due to the elimination of some of the nitrogen from MEEP in the form of ammonia gas (NH_3). This interpretation is proposed because the hydronium ions (H_3O^+) from $V_2O_5nH_2O$ (pH=3.2) could react with some of the nitrogen in MEEP. This phenomenon seems to have contributed to the lower nitrogen content in the nanocomposites than in MEEP to undetectable levels for EDS.

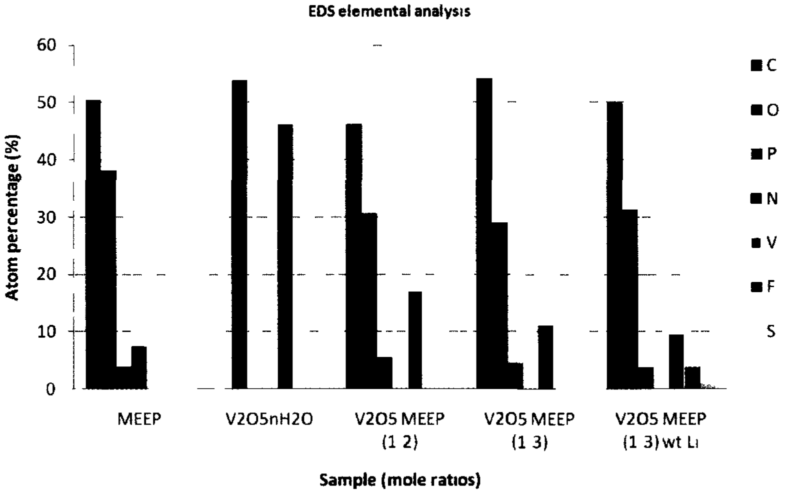

Figure 6.6: EDS for MEEP, $V_2O_5nH_2O$, V_2O_5MEEP1·2, V_2O_5MEEP1 3, and V_2O_5Li-MEEP1:3

6.1.6 Impedance spectroscopy

The conductivity of the nanocomposites was calculated from impedance plots, which were measured at different temperatures. The impedance complex plots for the nanocomposites V_2O_5 Li-MEEP1:1, V_2O_5 Li-MEEP1:2 and V_2O_5 Li-MEEP1:3 are shown in Figure 6.7 A. For comparison, the impedance complex plot for Li-MEEP (used as a control sample without $V_2O_5nH_2O$) is shown in Figure 6.7 B. The impedance

---

[1] Quantitative elemental analysis was done by Guelph Chemical Laboratories Ltd.

plots of imaginary (-Im Z) versus real (Re Z) parts were used to distinguish between electronic and ionic conductivities. For a sample with electronic conductivity (e.g. V_2O_5Li-MEEP1:1 in Figure 6.7 A plot *a*), the impedance complex plane plots are semicircles similar to plots for a simple parallel resistor capacitor (RC) circuit. This model was used to fit electronic conductor impedance plots. R represents the resistance of an electrically conducting sample and C being the cable capacitance in parallel with it. For an ionic conductor such as Li-MEEP (Figure 6.7 B), between blocking electrodes, the impedance plot displays a semicircle at higher frequencies, transitioning to a positively-sloped linear segment at low frequencies. The frequency decreases along the x-axis from left to right of the complex plot.

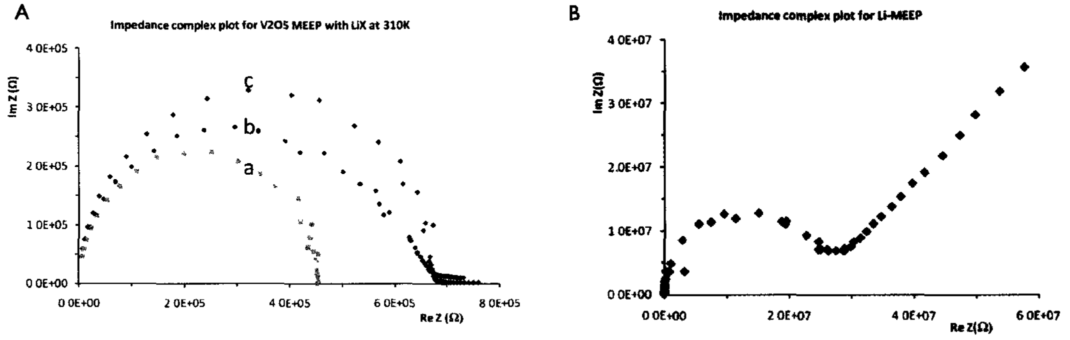

Figure 6.7: Complex plots (A) a) V_2O_5Li-MEEP1:1, b) V_2O_5Li-MEEP1:2 c) V_2O_5Li-MEEP1:3 and (B) Li-MEEP. The frequencies decrease from left to right along the curves (x-axis).

The type of conduction in V_2O_5Li-MEEP1:2 and V_2O_5Li-MEEP1:3 (Figure 6.7 A plot *b* and *c*) is less clear. Instead of the semicircle, terminating at a point on the real axis like an electronic conductor or rising at low frequencies like a purely ionic conductor there is a "tail" close to the real axis. This is most likely due to a combination of significant amounts of both types of conductivity. For frequencies high enough that the blocking electrodes have little effect, the graph is a semicircle tending toward RII, the parallel combination of the ionic and electronic resistances. In the low frequency limit, the ionic impedance diverges to infinity (Figure 6.7 B) leaving only the electronic contribution, so the curve "tails" off towards R_{el}, which is greater than R_{II}. Another possible explanation is that we have mainly ionic conduction, but also some electrochemical reaction at the sample/electrode interface that reduces or oxidizes the mobile ions. In this case, current can be carried ionically even at zero frequency - we no longer have blocking electrodes.

The resistance of the samples was determined from the impedance complex plots based on the type of conductivity they displayed. For an electric conductor, the resistance is the real part of the curve when the imaginary (-Im Z) part is zero at the lower frequency of the complex plot. For an ionic conductor, the resistance is approximately the real (Re Z) part of the impedance where the semicircle transitions into a positive slope usually referred to as the "dip" in the complex plot.[11] The positive sloping curves at low frequency for ionic conductors are due to the ionic blocking electrodes. The resistance values from the complex plots and the sample dimensions are used to calculate the resistivity (ρ) of the samples. The conductivity (σ) of the sample is the inverse of resistivity (ρ). The conductivity values of the nanocomposites are summarized in Table 6.4. The high uncertainty values (shown in Table 4) are due to the difficulties in measuring the dimensions of the sample films.

Table 6.4: Calculated conductivity values for the nanocomposites and control samples.

Materials (mole ratios)	Conductivity (Scm^{-1}) at 310 K	
	Without LiX	With LiX
MEEP	n/a	1.44E-03 ± 7.24E-04
$V_2O_5nH_2O$	3.72E-03 ± 1.27E-03	n/a
V_2O_5MEEP (1:1)	4.09E-05 ± 1.36E-05	7.42E-04 ± 3.71E-04
V_2O_5MEEP (1:2)	8.91E-06 ± 4.46E-06	8.47E-04 ± 4.26E-04[a]
V_2O_5MEEP (1:3)	2.22E-04 ± 1.11E-04	4.35E-04 ± 2.18E-04[a]

[a] Materials showed mixed conductivities.

7 De-intercalation of Na from $NaFeO_2$ *via* hydrolysis and intercalation of guests into the resulting aqueous extract

7.1 Results and discussion

De-intercalation of Na from α-$NaFeO_2$ by using water to produce α-$Na_{1\text{-}x}FeO_2$, where $x \approx 1$ is reported for the first time. This de-intercalation technique provides an excellent route to ion exchange Na with other metal ions in α-$NaFeO_2$. Interestingly, the extracted solution captures CO_2 from the atmosphere leading to the formation of layered sodium carbonate hydrate crystals. The lamellar structure of the hydrate crystals was confirmed by powder X-ray diffraction. The sodium carbonate hydrate obtained was found, through elemental analysis, to be deficient of Na compared to regular sodium carbonate. Intercalation of guest molecules such as polymers, alcohols, and inorganic ions into the gallery space of this sodium carbonate hydrate crystals is demonstrated by powder X-ray diffraction. The materials were also characterized by thermogravimetric analysis, differential scanning calorimetry, infrared spectroscopy, X-ray photoelectron spectroscopy, and scanning electron microscopy.

7.1.1 X-ray diffraction (XRD)

X-ray diffraction technique was used to investigate the structural phases of the materials synthesized. The XRD pattern of the extract, the residue, and pristine $NaFeO_2$ are shown in Figure 7.1. The indexed pattern for $NaFeO_2$ is included in Figure 7.1. The diffraction pattern of the extract exhibits three strong ($00l$) peaks with d values of 5.35 Å, 2.67 Å and 1.78 Å, respectively. The XRD pattern of the extract crystals can be indexed to a rhombohedra symmetry of $NaFeO_2$ with hexagonal unit cell (space group: $R-3m(166)$, $a = 3.0221$ Å, $b = 3.0221$ Å, $c = 16.0817$ Å, $\alpha = \beta = 90$ ° and $\gamma = 120$ ° ICDD card No. 82-1495).

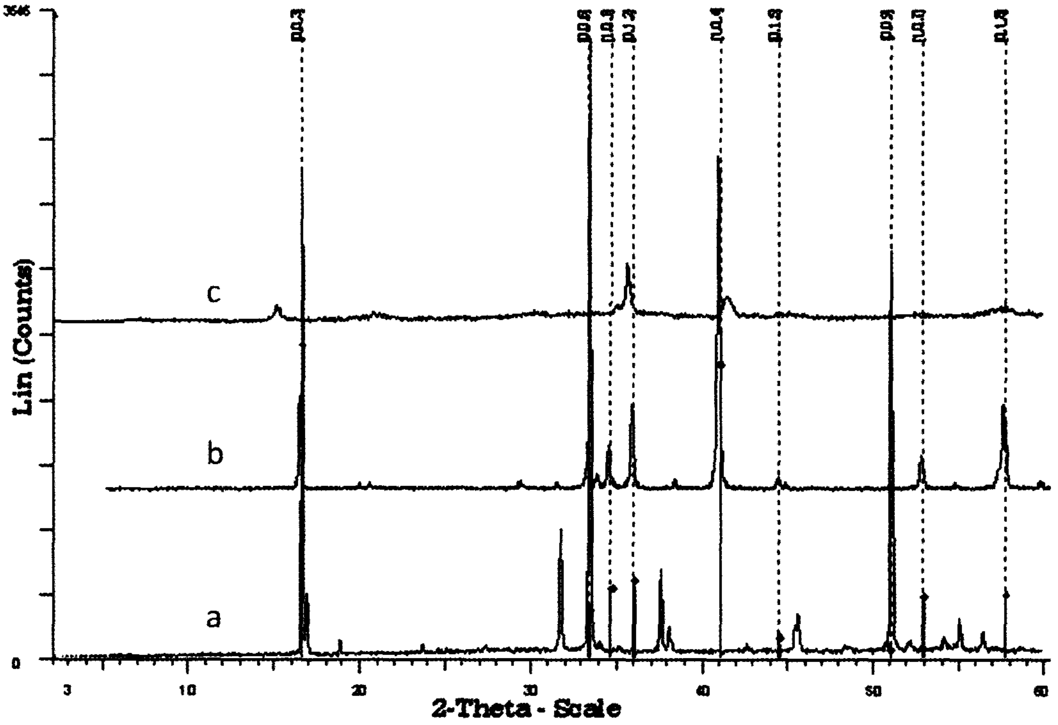

Figure 7.1: XRD of a) the extract b) $NaFeO_2$ and c) the residue. The indexed pattern shown is for hexagonal unit cell rhombohedra $NaFeO_2$.

The three (*00l*) peaks of the extract (matching the indexing of $NaFeO_2$ at 003, 006, and 009), indicates the formation of a lamellar structure. It seems like that the sandwiches[52] of O^{2-} - Na^{+} - O^{2-} from the α-$NaFeO_2$ structure, are retained in the extract, which is found to be sodium carbonate hydrate (no Fe is present, *videinfra*). The changes in intensity for the three strong (*00l*) reflections in the extract crystals would be due to the transparency of the intercalated water molecules instead of the strongly scattering FeO_2 sheets. This interpretation could explain the observation of the strong (009) reflection in the extract crystals which is weak in the XRD pattern of pristine $NaFeO_2$. When Takeda *et al.* [52] reported the hydrolysis of

$NaFeO_2$ at room temperature in air; they did not provide any experimental data for the hydrolysis products, which could have been used for comparison in this work.

For comparison, the XRD patterns of sodium carbonate powder (Na_2CO_3) dissolved in water and the extract crystals powder are shown in Figure 3. Surprisingly, the Na_2CO_3 powder dissolved in water did not show any needle-like crystals; instead the cast dried as a white powder. However, the diffraction pattern of the cast powder of Na_2CO_3 and the dry powder of the extract seem to have similar reflections, with the extract powder being more crystalline.

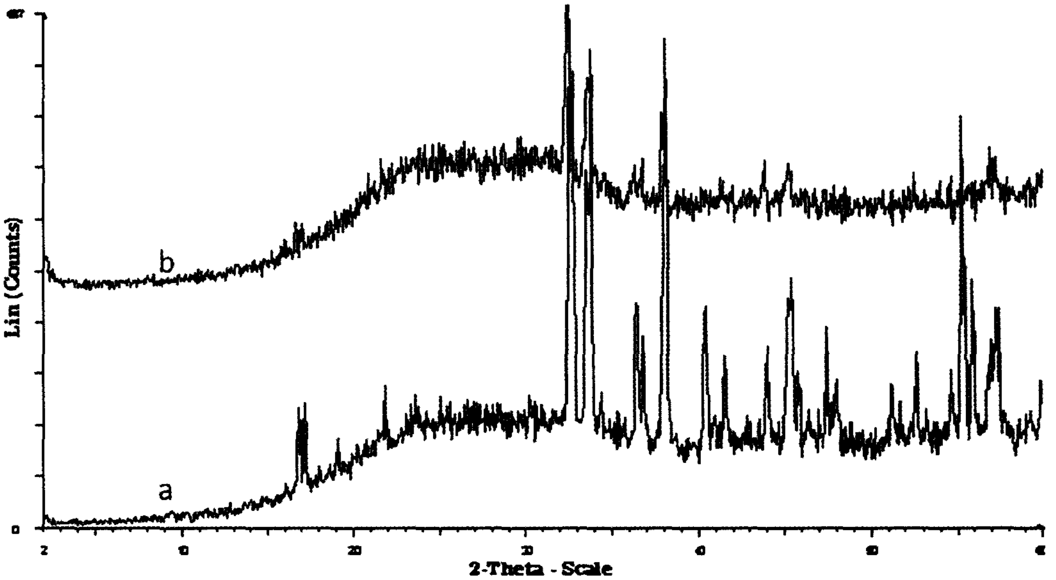

Figure 7.2: XRD of a) the extract powder and b) Na_2CO_3 powder.

It is important to note that re-dissolving the dry powder of the extract shows complete reversibility of the X-ray diffraction pattern up to the original three *(00l)* reflections (see Figure 7.4 b), an observation indicating that the process is topotactic. Therefore, it is clear that the water molecules are being intercalated and de-intercalated from the extract crystals. Attempts were made to substitute the water molecules with organic and inorganic guest molecules. These water substitution intercalation reactions were found to be successful. Figure 7.3 depicts XRD patterns of the extract intercalated with methanol, ethanol, and poly[bis-(2-methoxyethoxyethoxy)

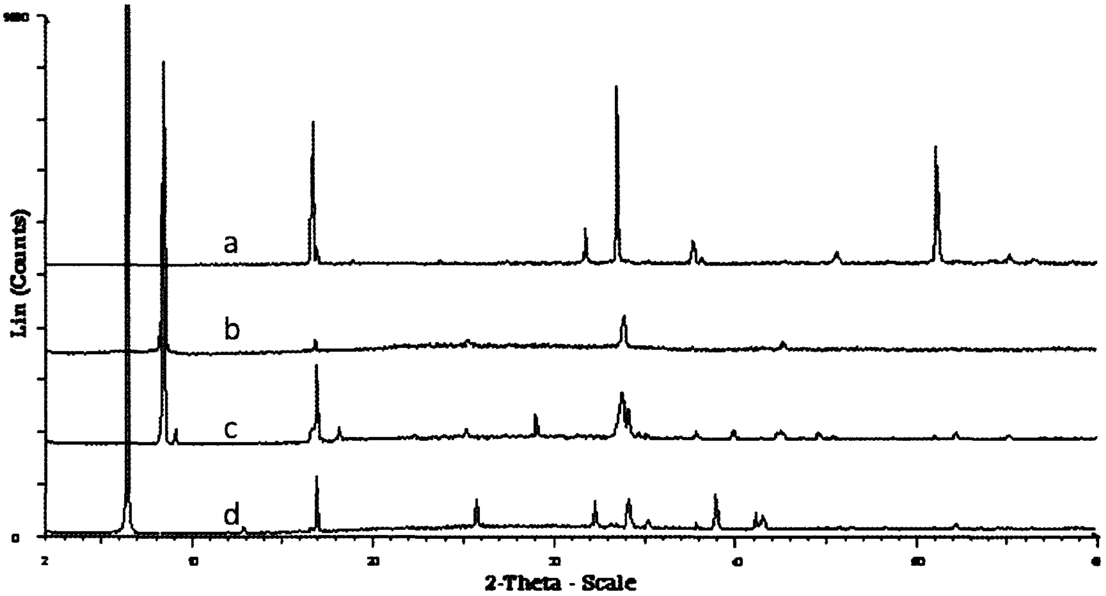

Figure 7.3: XRD of a) the extract and the extract intercalated with b) MEEP, c) methanol and d) ethanol.

phosphazene] (MEEP)[1]. Table 7.1 provides a summary of the interlayer expansions of all guest molecules that were successfully intercalated into the extract crystals.

Table 7.1: Summary of interlayer expansions for the extract nanocomposites.

Guest molecule	d-spacing (Å)	Δd-spacing (Å)
Extract crystals only	5.4	
Methanol	10.6	5.2
Ethanol	13.8	8.4
Cyclohexanol	17.0	11.6
Ammonium hydroxide	9.8	4.4
Carbon monoxide	10.7	5.3
MEEP	10.7	5.2
POMOE	10.6	5.3

A study was done to find out if the properties of the extract are specific to the method of preparation of the pristine $NaFeO_2$ material. With this line of thought, an alternate procedure for synthesizing $NaFeO_2$ was utilized. In this alternate method,

---

[1] MEEP was synthesized as reported in the literature[87,88]

sodium hydroxide pellets (NaOH) were used instead of sodium peroxide (Na_2O_2). More specifically, NaOH (1.1 g, 0.028 mol) was mixed with Fe_2O_3 (2.2 g, 0.014 mol) and quickly ground in air using a mortar and pestle. The resulting powder was transferred into a crucible and heated for 2 hours in a furnace set at 200 °C. The product was extracted and the XRD pattern of the extract solution looked similar to the extract obtained using the original Na_2O_2 method, showing only the three main (*00l*) peaks as shown in Figure 5a. Therefore, the other extra peaks in the XRD pattern of the extract from Na_2O_2 method are thought to be due to different orientations of the crystals in the cast film.

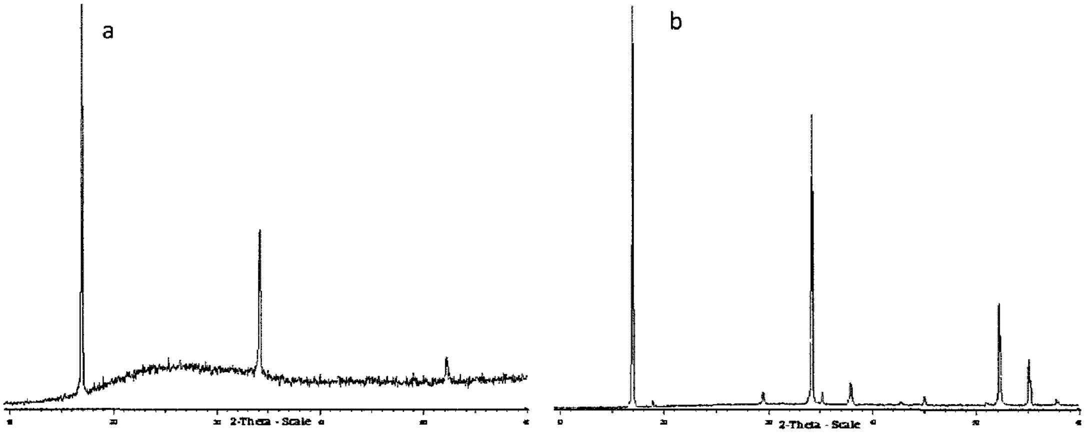

Figure 7.4: XRD of a) the extract cast from NaOH method b) cast of the extract powder from Na_2O_2 method dried at 100 °C and then re-dissolved in water.

The XRD pattern of the residue (Figure 7.1 curve *c*) has broad peaks, implying smaller crystallites or a lot of disorder than pristine $NaFeO_2$ but not amorphous as report by Takeda *et al.* [52] Scanning electron microscopy (SEM) confirms that the residue is actually layered similar to that of pristine $NaFeO_2$ as shown in Figure 7.5. Therefore, the layered nature of the FeO_2 sheets is retained upon de-intercalation of Na.

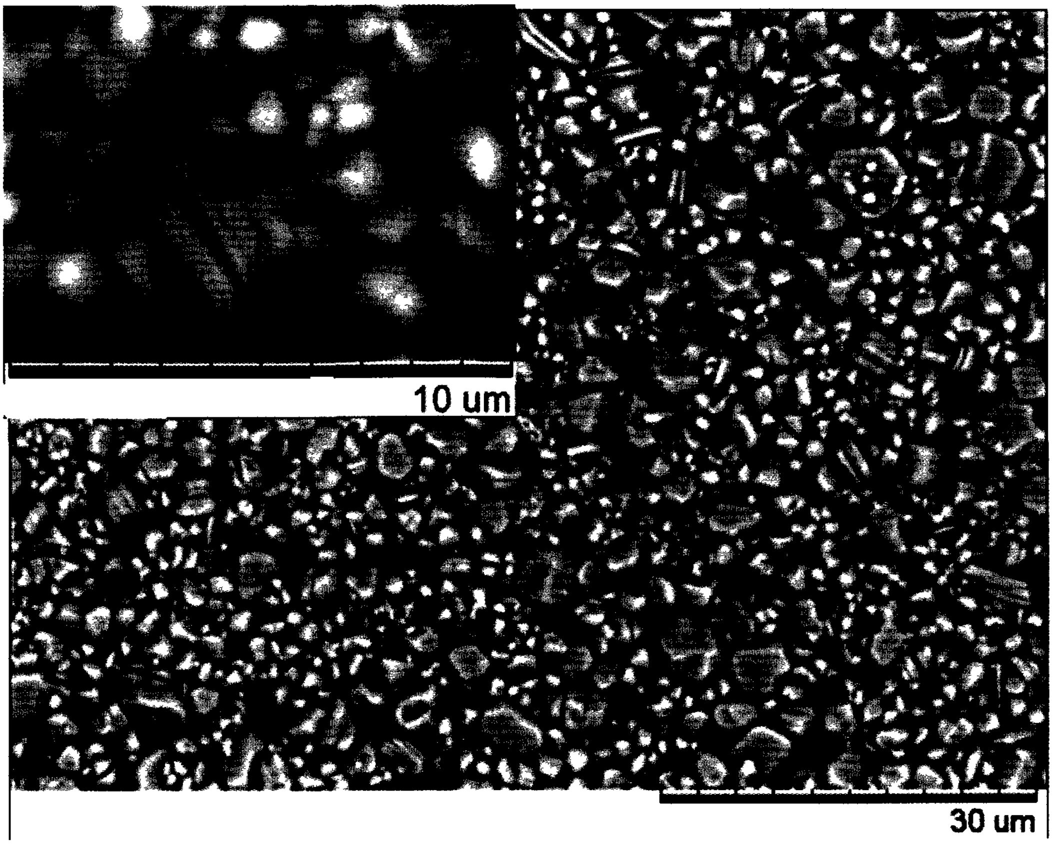

Figure 7.5: SEM of the residue and pristine $NaFeO_2$ (insert).

7.1.2 Thermogravimetric analysis

Thermogravimetric analysis was used to further characterize the extract, residue, and pristine $NaFeO_2$. It was found that the extract powders gave different thermograms depending on how the solution was dried. Figure 7.6 shows the TGA spectra of the extract dried at room temperature and two freeze-dried samples at different time intervals. The decomposition profiles show weight losses at 100 °C, which correspond to the evaporation of water molecules.

The extract dried at room temperature (Figure 7.6 curve *b*) loses around 14% weight at 100 °C. The freeze-dried and desiccated sample (Figure 7.6 curve *c*) shows a weight loss of 16% at 100 °C. Interestingly, the weight loss of the sample soon after freeze-drying (Figure 7.6 curve *a*) was significantly lower (shows only 6.5% weight

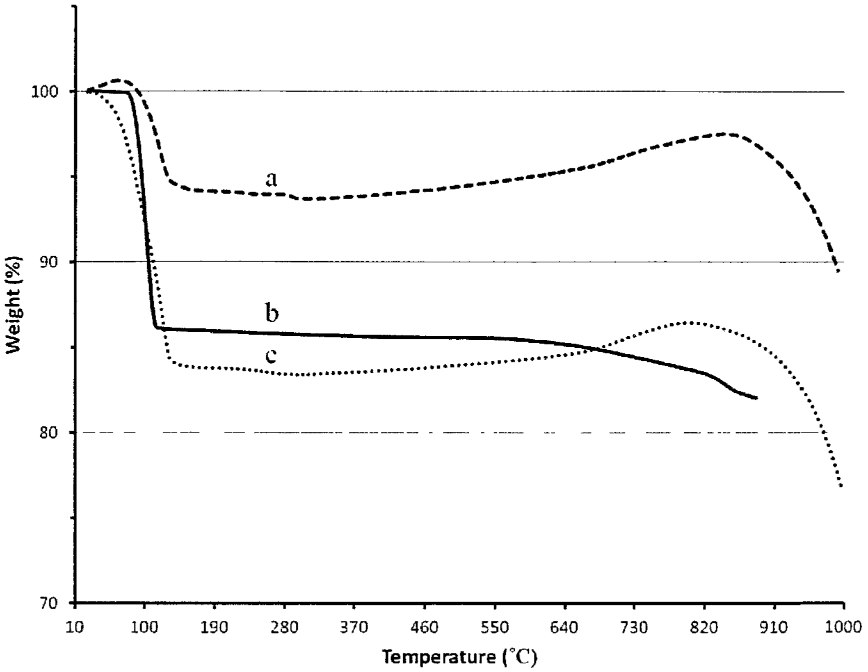

Figure 7.6: TGA of the extract a) soon after freeze-drying, b) dried at room temperature and c) freeze-dried and dessicated for seven days.

loss). The explanation for this difference is that the sample, which was freeze-dried without dessication, was first oxidized in air before decomposition. This interpretation is based on the observed weight increase below 100 °C. Therefore, the lower weight loss corresponds to the formation of a stable phase during the oxidation reaction. The freeze-dried samples (Figure 7.6 curve *a* and *c*), show a small weight loss step at around 284 °C, which corresponds to either strongly bound water molecules or loosely bound CO_2. Further decomposition of the samples above 810 °C indicates a collapse of the layered structure, and the evaporation of strongly bound CO_2.

The decomposition profiles of the residue were also studied based on the number of water extractions done. The thermograms provide some insights into the hydrolysis/extraction process. Figure 7.7 compares the thermogram of the residue obtained in one extraction versus five extractions.

The residue gradually loses weight up to around 310 °C. This is in contrast to the

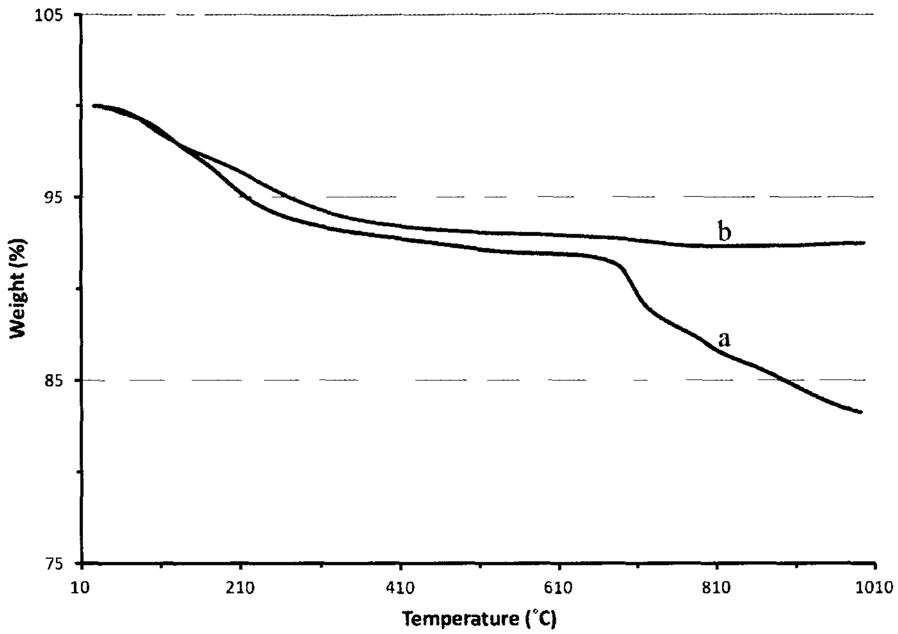

Figure 7.7: TGA of the residue after a) one extraction b) five extractions

extract powder, which loses water sharply at around 100 °C (see Figure 7.6). After five extractions, the weight loss at around 700 °C was eliminated. The weight loss at 700 °C in Figure 7.7 curve *a* is ascribed to adsorbed CO_2. This interpretation is based on EDS data which show the absence of carbon in the residue that underwent several extractions/washings. It was also noticed that the residue became softer after several extractions.

The TGA of pristine $NaFeO_2$ was done as a control to compare with the thermogram of the residue. Figure 7.8 shows the TGAs of pristine $NaFeO_2$ exposed to air at room atmosphere and a dessicated $NaFeO_2$ sample only exposed to air during handling.

It was found that the $NaFeO_2$ sample exposed to air loses less than 1% weight at 100 °C, a weight loss corresponding to the surface-adsorbed water molecules due to the hygroscopic nature of the $NaFeO_2$. The un-exposed sample does not show a sharp weight loss at 100 °C but rather a gradual weight loss is observed up to around 400 °C. A small weight loss of about 0.5% is also observed at around 500 °C, and then

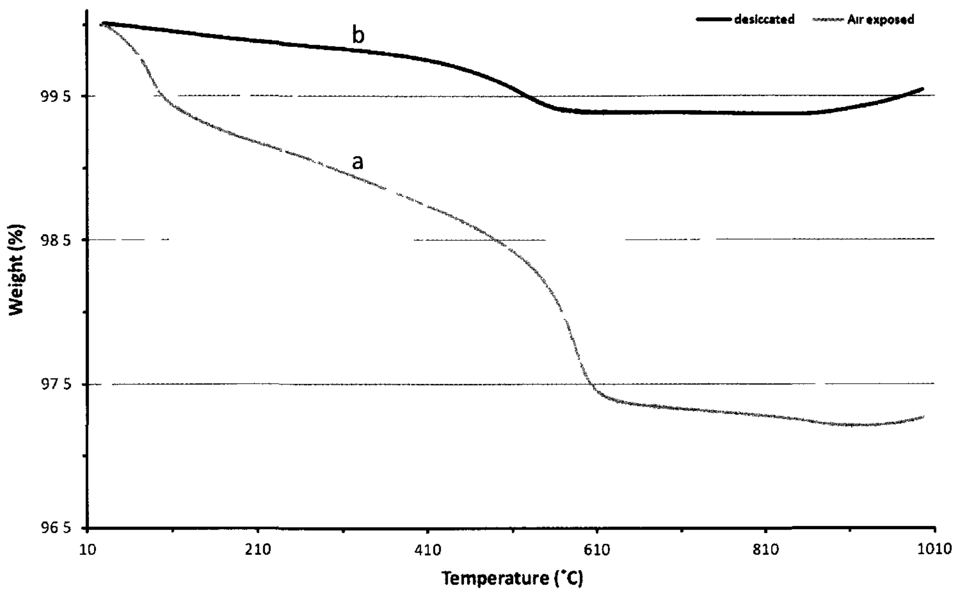

Figure 7.8: TGA of pristine a) $NaFeO_2$ exposed to air b) $NaFeO_2$ dried in a dessicator.

the sample gains weight at around 850 °C, due to oxidation. The weight loss at 500 °C corresponds to the evaporation of adsorbed CO_2, which is at a lower temperature compared to similar weight loss in the residue which occurs at 700 °C (see Figure 8 a). This means that upon hydrolysis of $NaFeO_2$ any adsorbed CO_2 in the residue is more strongly bound.

7.1.3 Differential scanning calorimetry

Differential scanning calorimetry was used to investigate any thermal phase transitions occurring in the materials. The thermal phase transitions observed in the extract crystals/or powders are dependent on the sample preparation methods, and the DSC data complement the TGA observations. Figure 7.9 shows the thermal phase transitions of the extract crystals, extract powder immediately after freeze-drying, and extract powder freeze-dried and dessicated for seven days.

The extract dried at room temperature shows three overlapping endothermic peaks in the temperature range 90-100 °C. The endothermic peaks are due to the release

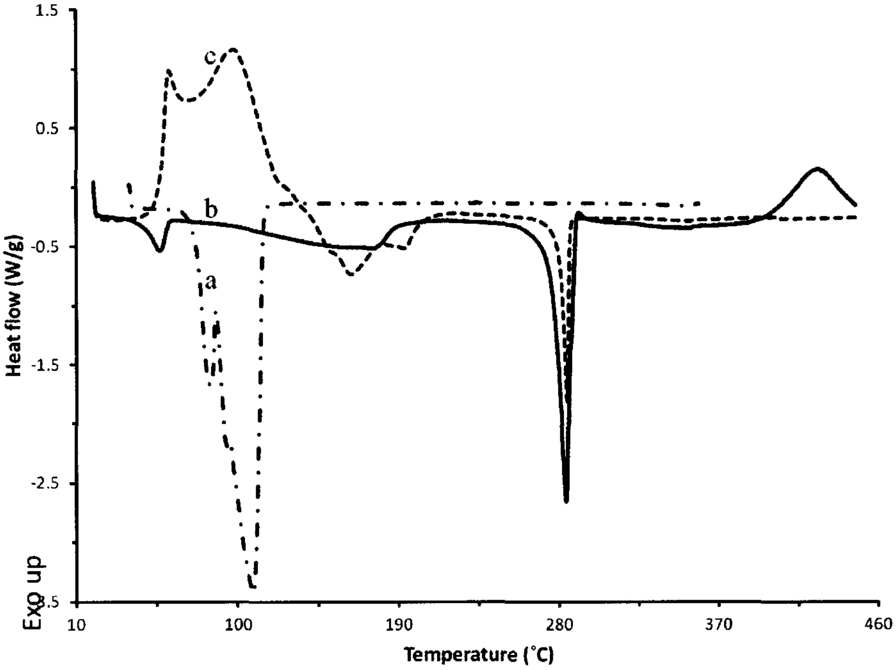

Figure 7.9: DSC of the extract a) dried at room temperature, b) soon after freeze-dried, and c) after freeze-dried and dessicated for seven days.

of water molecules from the crystals and are consistent with the TGA data. The three endothermic peaks provide further information with regards to the nature of the water molecules in the crystals. The peaks indicate that there are three different bond energies of the water molecules within the structure. The freeze-dried extracts on the other hand, show completely different phase transitions. The freeze-dried and desiccated sample (Figure 7.9 curve c) shows two overlapping exothermic peaks in the region 50-100 °C. The exothermic peaks are associated with crystallization phase transtions.[100] This indicates that upon freeze drying, the layered crystals are randomly oriented, however upon dessication, any remaining water molecules are removed without allowing the crystals to re-arrange themselves in a stable form. Hence upon heating, the crystals gain enough energy to re-organize themselves leading to the observed exothermic peaks in the region 50-100 °C. However, if the freeze-dried sample is heated immediately, any residual water is evaporated leading to the observed endothermic peak. The freeze-dried samples (Figure 7.9 curve *b* and *c*) also show an endothermic phase transition at 284 °C. This endothermic phase transition corresponds to the removal of either strongly bound water or loosely bound CO_2, consistent with the TGA data in Figures 7.6 curve *a* and *c*. This endothermic phase transition is absent in the extract crystals dried at room temperature, which suggests that there are structural differences between room temperature and freeze-dried extract crystals or powders. In contrast, the DSC of the residues showed broad endothermic peaks, which correspond to the evaporation of adsorbed water molecules.

7.1.4 Elemental analysis

The elemental composition of the extract crystals, the residue, and pristine $NaFeO_2$ was determined by various techniques. The techniques used were X-ray photoelectron spectroscopy (XPS), energy-dispersive X-ray spectroscopy (EDS) and volumetric titrimetry. The EDS[2] data of the three representative samples are summarized in Figure 7.10. EDS shows that iron is not present in the extract but it is actually higher in the residue compared to pristine $NaFeO_2$ (a difference of around 10%). On the other hand, the sodium content is higher in the extract compared to the residue. It was observed that after several extractions with water, the Na content in the residue diminishes. Interestingly, XPS does not show the presence of iron in the extract pow-

Table 7.2: XPS elemental analyses of the extract and $NaFeO_2$.

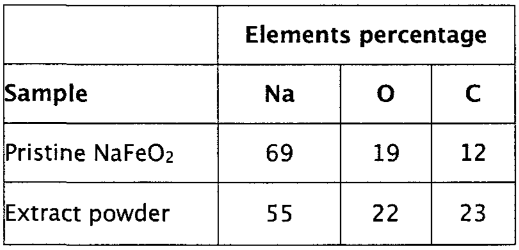

	Elements percentage		
Sample	**Na**	**O**	**C**
Pristine NaFeO2	69	19	12
Extract powder	55	22	23

---

[2] The EDS system used does not detect elements below atomic number 7. Therefore, though H is present in the form of water in the samples, it is not shown Figure 7.10.

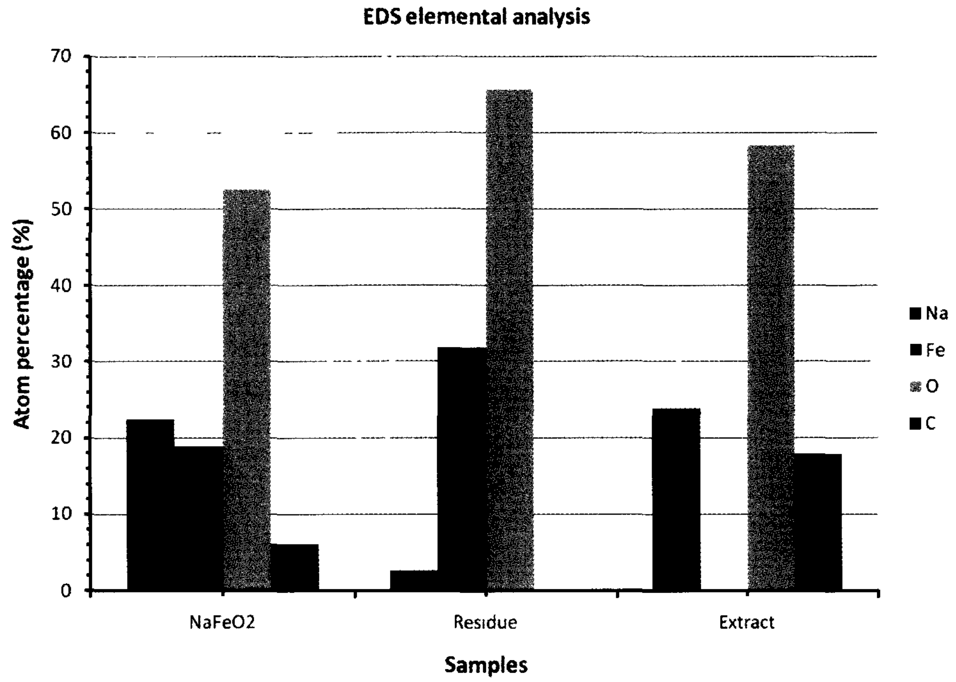

Figure 7.10: EDS elemental analyses of pristine $NaFeO_2$, the extract, and the residue.

der or pristine $NaFeO_2$. Table 7.2 provides a summary of the XPS data. The absence of iron especially in pristine $NaFeO_2$ by the XPS technique could be explained as follows. XPS is a surface technique, where the irradiated X-rays dislodge electrons from the surface of the sample (within 1 to 10 nm) and the kinetic energy and numbers of electrons are measured simultaneously.

From knowledge of the α-$NaFeO_2$ structure, the Na and Fe atoms are located in octahedral holes of cubic closest packed hexagonal layers of oxygen atoms.[52] The detection of Fe was suppressed due to the slight excess of Na_2O_2 used during the synthesis of $NaFeO_2$, which would mean saturation of the Na and O atoms, hence thickening the coating around the Fe atoms and preventing the escape of electrons.

Volumetric titrimetry was employed in order to confirm the presence or absence of iron in the extract powder, residue, and pristine $NaFeO_2$[3]. The results of the titration show that there is no iron present in the extract. The titration data reveal

---

[3] The method was adapted from reference[104].

that both pristine $NaFeO_2$ and the residue contain iron with an average value of 50% by mass and 60% by mass, respectively. The absence of Fe and presence of Na in the extract solution is strong evidence that the hydrolysis of α-$NaFeO_2$ leads to the de-intercalation of Na.

7.1.5 Fourier transform infrared spectroscopy

Infrared spectroscopy was used to further characterize the extract crystals, residue, and pristine $NaFeO_2$. The infrared spectrum of the extract is shown in Figure 7.11.

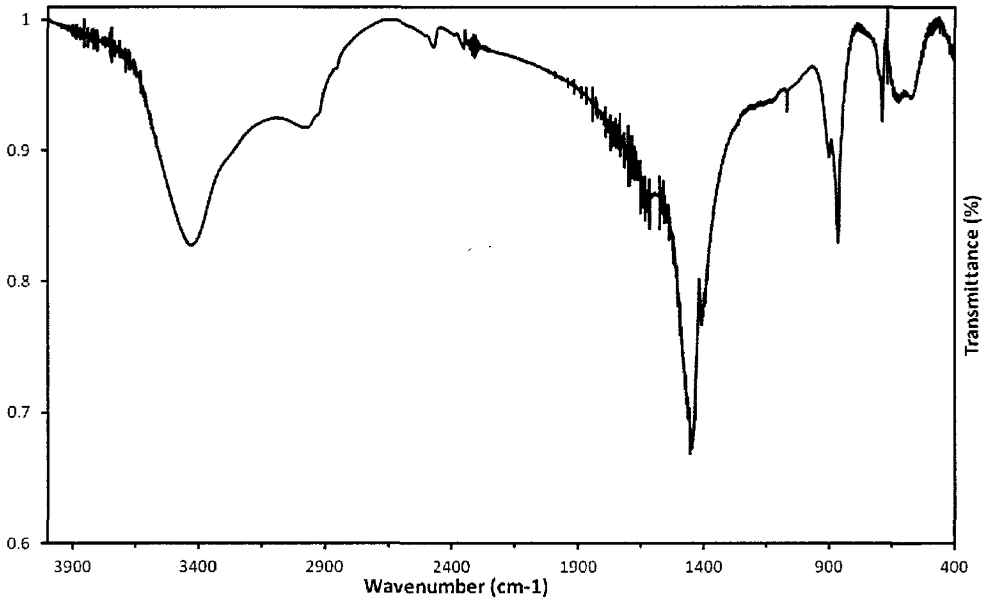

Figure 7.11: FTIR spectrum of the extract crystals.

The infrared spectrum of the extract shows absorption bands at 3437 cm^{-1} and 2992 cm^{-1}. These bands correspond to O-H and C-H stretches, respectively. The C-H bond is thought to come from the interaction of water molecules and the carbonate group in the crystals. These bands were absent in pristine $NaFeO_2$. A closer examination of the fingerprint region of the extract crystals and pristine $NaFeO_2$ reveals different absorption bands. However, there is a sharp band in both the extract and pristine $NaFeO_2$ occurring at 878 cm^{-1} and 883 cm^{-1}, respectively. This band is assigned to the Na-O bond, and the observed shift of this band is ascribed to differences in the chemical environment of the two materials.

The mechanism of the hydrolysis reaction leading to the formation of the sodium carbonate hydrate crystals was sought in order to further understand the system. First, a study was conducted, which involved degassing the water used for the extraction, by bubbling with nitrogen. A milky-white amorphous solid was obtained instead of clear needle-like crystals. Similar observations were noted when CO_2 gas was bubbled in deionized water before use. It was established from these findings that de-ionized water must be used "as is" in order to obtain the needle-like crystals from the extract solution. It was found in the literature that Huang *et al.* [101] had designed an experiment, which gave more insight into the mechanistic understanding of Na-Fe-O-H-C system. In their study, they carried out a theoretical simulation by using the thermodynamic computing code Thermo-Calc and MALT2 to investigate the influence of water vapor and CO_2 on the stability of Na-Fe oxides and Fe-Na_2O_2 mixture in high $H_2O + CO_2$ pressure conditions with flowing air. They made a comparison between the experimental and the calculated results. They reported that Na_2CO_3 was formed through the reaction of NaOH with CO_2 instead of the direct reaction between sodium ferrates (Na-Fe) and CO_2. They also reported that the reaction kinetics played an important role in the chemical behaviour of sodium ferrates in $H_2O + CO_2$ environment; i.e., the reaction speed of NaOH with CO_2 is much faster. Therefore, relating this finding to our system it means that during the hydrolysis of $NaFeO_2$, NaOH is first formed (by the interaction between Na^+ and H_2O) which then traps CO_2 from the atmosphere to form sodium carbonate. The pH of the extract solution was found to be greater than 12.0.

The composition of the extract crystals, residue, and pristine $NaFeO_2$ was calculated based on EDS and TGA data. The empirical formula[4] for the extract was estimated to be $NaCO_3(H_2O)_{0.8}$. It is clear from this calculation that although the extract crystals are referred as sodium carbonate hydrate, they have deficient Na ions. This deficiency could be contributing to the peculiar properties of the crystals. The empirical formula for the residue after five extractions was calculated to be $Na_{0.3}FeO_2$, and the empirical formula for pristine $NaFeO_2$ was calculated to be $Na_{1.17}FeO_2$.[81] The higher oxygen content in pristine $NaFeO_2$ could be due to two factors: the adsorbed CO_2 (trace of carbon was detected by EDS) due to exposure of the sample in air, and the slightly excess Na_2O_2 used during the synthesis. Therefore, it is reasonable to assume that the empirical formula for the pristine sodium iron oxide is $NaFeO_2$. The synthetic methodology developed in this work can be summarized as shown in the schematic below

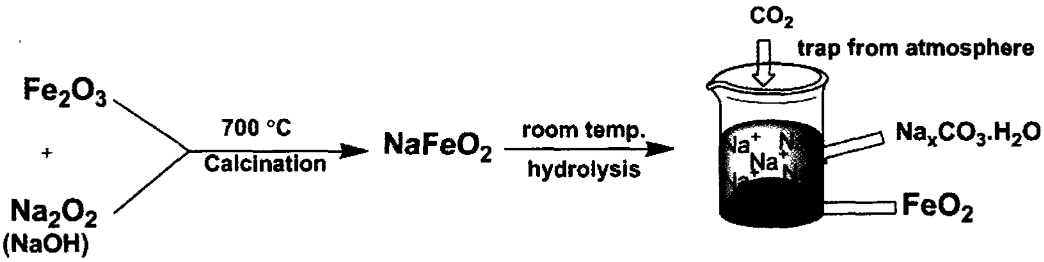

Figure 7.12: Methodology for de-intercalating Na from $NaFeO_2$ and the resulting products.

It is interesting to note that various forms of sodium carbonate hydrates have been reported and debated for decades. Pabst[102] described one form of sodium carbonate hydrate, which closely resembles what is reported here. However, single crystal crystallography was not performed in our work (owing to the difficulties in growing single crystals) to compare with his data. The sodium carbonate hydrate crystals that Pabst prepared were described to be several centimeters in length, needle-shaped, and often in a shear-like arrangement. The crystals were orthorhombic and showed a strong

---

[4] The water content was determined from TGA, while the Na, C, and O were calculated from EDS data. The exact ratio as determined from EDS was $Na_{1.34}CO_{3.28}$. The only discrepancy with this calculation is the value for O, because the EDS can not distinguish between oxygen from carbonate and water.

development of a prism zone with four or five faces. Pabst pointed out that the forms (110), (010), (101) and (011) were always present. Also, Blasdale[103] described similar sodium carbonate hydrate crystals as a salt that usually separates in the form of needles but occasionally as long 4-sided or flattened 8-sided prisms terminated by a single pair of planes intersecting at 134°. These descriptions provide evidence to conclude that sodium carbonate hydrates form various crystals depending on their method of preparation, which has not yet been fully explored in order to determine the fundamental principles behind this phenomenon.

8 Conclusions and Further work

8.1 Conclusions

In summary, two methodologies were developed in the course of this project. First, was a versatile method for intercalating POMOE, POEGO, MEEP and their lithiated complexes into $V_2O_5nH_2O$ at room temperature. Intercalation of POMOE and POEGO resulted into a bilayer loading of the polymer into vanadium pentoxide ribbons. The optimal intercalation mole ratio for $V_2O_5nH_2O$ to POMOE and POEGO was found to be around 1:1 and 1:2, respectively. The optimal intercalation ratio was selected from the lowest mole ratio resulting to a saturated bilayer expansion value of the nanocomposites. The bilayer loading of POMOE and POEGO chains is a significant finding because it means that more Li-ions could be intercalated into the resulting nanocomposites. The finding increased the prospect of the nanocomposites to be used as cathode materials in lithium ion batteries. However, ionic conductivity was not detected by our measurement technique for the POMOE and POEGO nanocomposite lithium complexes (based on optimal literature ratio of $[EO]/Li^+$). Some intercalates from POEGO were found to be amorphous in the battery operation temperature range (-30 °C to 100 °C). An intercalation mechanism, which can apply to PEO and its derivative polymers, was proposed. Hydrogen bonding is thought to play a key role in the formation of the nanocomposites.

MEEP nanocomposites were significantly different from those of POMOE and POEGO. For example, TGA showed that MEEP nanocomposites were dry without structural/adsorbed water molecules; the XRD showed that increasing the amount of MEEP increased the d-spacing of the nanocomposites. And most important was the detection of mixed (electronic and ionic) conductivity, in V_2O_5Li-MEEP1:2 and V_2O_5Li-MEEP1:3. These properties provide an appealing potential of using MEEP-$V_2O_5nH_2O$ nanocomposites in lithium/Li-ion batteries. Intercalation reaction between MEEP and $V_2O_5nH_2O$ was found to proceed *via* the interaction of hydronium ions (H_3O^+) from $V_2O_5nH_2O$ with the PNP parent-chain of MEEP. The interaction leads to the liberation of nitrogen from the nanocomposites as ammonia gas. The results from MEEP provide strong evidence for a potential solid-electrolyte and cathode materials for a "vanadium-lithium" battery.

The structural characteristics and conductivity properties observed from the nanocomposites reported here provide strong evidence that the methodology developed from this project could potentially be extended to other intercalation systems for the development of new materials. For example, it is important to determine the optimum intercalation ratios between the layered structure and the polymer. Similarly, the corresponding physical and chemical properties from different ratios could find diverse applications because of their varied properties.

The second methodology is for the de-intercalation of Na from α-$NaFeO_2$ using water. The conclusion to successful de-intercalation of Na from α-$NaFeO_2$ was based on the elemental analysis and SEM of the residue obtained after the hydrolysis of α-$NaFeO_2$ and separation of the products. The elemental analysis show that the Na content in the residue diminishes but the ratio of iron to oxygen is maintained. A discussion demonstrating that during α-$NaFeO_2$ hydrolysis, the Na ions are hydrolyzed with water molecules leading to the exfoliation of the layered structure is provided. The re-stacking of the "FeO_2" sheets is poor leading to loss of crystallinity as observed by XRD. The lamellar structure of the residue was confirmed by SEM. TGA/DSC analysis provides evidence that the structure of the extract crystals (sodium carbonate hydrate) were greatly influenced by the method used to remove the excess water such as slow evaporation at room temperature or freeze drying.

The extract crystals from α-$NaFeO_2$ have a layered structure. They can be intercalated with organic and inorganic guests. This is a double blessing for α-$NaFeO_2$ system because the two hydrolysis products (residue and extract) will have various scientific and economic applications. For example, we have shown the successful intercalation potentials of the extract. Through this project, a goal set by Takeda *et al.* [51] to "synthesize FeO_2" was achieved. Therefore, this was a significant breakthrough. The layered structure ($Na_{1-x}FeO_2$ where $x \approx 1$) which contains cheap iron instead of expensive cobalt, is now available for intensive study as an electrode material for secondary batteries. I believe that this methodology would lead to the development of new materials with unlimited applications ranging from energy storage to environmental remediation materials.

8.2 Further work

The next challenge is to study the effect of using different lithium salts for the optimally intercalated nanocomposites reported here. This is because the additional matrix from the salt may be contributing to the poor ionic conductivity detected. For example, LiI would be a good candidate because it has been reported to produce V_2O_5Li-PEO with the elimination of iodine gas hence excluding the anion matrix in the nanocomposites.[91] It would be of great interest to develope prototype cells using V_2O_5Li-MEEP nanocomposites as cathodes to explore further their mixed (ionic and electronic) conductivities.

Intensive study using $Na_{1-x}FeO_2$ as an electrode material instead of $LiCoO_2$ to develop prototype cells cannot be overstated. There are two ways of making these prototype cells. One method is to blend $Na_{1-x}FeO_2$ with graphite as the cathode and use lithium metal as the anode (charged state battery). The second method is to intercalate Li-ions into $Na_{1-x}FeO_2$ and use graphite as the anode (discharge state battery).

References

1 Z. Yang, J. Zhang, M. C. W. Kintner-Meyer, X. Lu, D. Choi, J. P. Lemmon and J. Liu, *Chem. Rev.*, 2011, **111**, 3577-3613.

2 M. Winter and R. Brodd, *Chem. Rev.,* 2004, **104**, 4245-4270.

3 F. Cheng, J. Liang, Z. Tao and J. Chen, *Adv. Mater.,* 2011, **23**, 1695-1715.

4 C. Liu, F. Li, L. Ma and H. Cheng, *Adv. Mater.,* 2010, **22**, E28-E62.

5 R. Marom, F. Amalraj, N. Leifer, D. Jacob and D. Aurbach, *J. Mater. Chem.,* 2011, **21**, 9938-9954.

6 M. S. Whittingham, *Chem. Rev.,* 2004, **104**, 4271-4301.

7 D. Berndt and D. Spahrbier, in *Ullmann's Encyclopedia of Industrial Chemistry,* ed. Wiley-VCH, Wiley-VCH, Berlin, German, 2001,.

8 H. Chen, T. Ngoc Cong, W. Yang, C. Tan, Y. Li and Y. Ding, *Prog. Nat. Sci.,* 2009, **19**, 291.

9 F. R. Gamble, J. H. Osiecki, M. Cais, R. Pisharody, F. J. DiSalvo and T. H. Geballe, *Science,* 1971, **174**, 493-497.

10 K. Mizushima, P. C. Jones, P. J. Wiseman and J. B. Goodenough, *Mater. Res. Bull.,* 1980, **15**, 783-789.

11 E. Barsoukov and J. R. Macdonald, *Impedance Spectroscopy: Theory, Experiment, and Applications,* John Wiley & sons, Hoboken, New Jersey, USA, 2005.

12 J. B. Goodenough, H. D. Abruña and M. V. Buchanan, *Basic Research Needs for Electrical Energy Storage,* USA Department of energy, 2007.

13 J. W. Fergus, *J. Power Sources,* 2010, **195**, 939-954.

14 V. S. Kolosnitsyn, G. P. Dukhanin, S. A. Dumler and I. A. Novakov, *Russ. J. Appl. Chem.,* 2005, **78**, 1-18.

15 F. M. Gray, *Solid Polymer Electrolytes: Fundamentals and Technological applications,* VCH, 1991.

16 J. R. MacCallum, *Polymer Electrolyte Reviews*, Elsevier Applied Science, 1987.

17 F. Croce, G. B. Appetecchi, L. Persi and B. Scrosati, *Nature,* 1998, **394**, 456.

18 E. Quartarone, P. Mustarelli and A. Magistris, *Solid State Ionics,* 1998, **110**, 1-14.

19 J. Schaefer, S. Moganty, D. Yanga and L. Archer, *J. Mater. Chem.*, 2011, **21**, 10094-10101.

20 H. Xiong, D. Liu, H. Zhang and J. Chen, *J. Mater. Chem.*, 2004, **14**, 2775-2780.

21 Y. Li and P. Fedkiw, *J. Electrochem. Soc.*, 2007, **154**, A1140-A1145.

22 S. Seki, Y. Ohno, Y. Kobayashi, H. Miyashiro, A. Usami, Y. Mita, H. Tokuda, M. Watanabe, K. Hayamizu, S. Tsuzuki, M. Hattori and N. Terada, *J. Electrochem. Soc.*, 2007, **154**, A173-A177.

23 H. Ye, J. Huang, J. Xu, A. Khalfan and S. Greenbaum, *J. Electrochem. Soc.*, 2007, **154**, A1048-A1057.

24 P. Birke, F. Salam, S. Döring and W. Weppner, *Solid State Ionics,* 1999, **118**, 149-157.

25 P. V. Wright, *Brit. Polym. J.*, 1975, **7**, 319.

26 M. B. Armand, J. M. Chabagno and M. Duclot, *Fast ion Transport in Solids. Electrodes and Electrolytes,* 1978.

27 F. Croce, R. Curini, A. Martinelli, L. Persi, F. Ronci, B. Scrosati and R. Caminiti, *J. Phys. Chem. B,* 1999, **103**, 10632-10638.

28 W. Müller-Warmuth and R. Schöllhorn, *Progress in intercalation research*, Kluwer Academic Publishers, US, 1994.

29 A. D. Pomogailo, *Polym. Sci.*, 2006, **48**, 85-111.

30 M. S. Whittingham and A. J. Jacobson, in *Intercalation Chemistry* ed. R. M. Barrer, Academic Press, 1983,.

31 L. Wu, H. Yao, B. Hu and S. Yu, *Chem. Mater.*, 2011, **23**, 3946-3952.

32 R. Baddour, J. P. Pereira-Ramos, R. Messina and J. Perichon, *J. Electroanal. Chem.*, 1990, **277**, 359-366.

33 C. G. Tsiafoulis, A. B. Florou, P. N. Trikalitis, T. Bakas and M. I. Prodromidis, *Electrochem. Commun.*, 2005, **7**, 781-788.

34 H. E. Toma, *Mater. Sci. Forum,* 2010, **636**, 729.

35 J. Livage, *Coord. Chem. Rev.*, 1998, **178-180**, 999-1018.

36 G. S. Zakharova and V. L. Volkov, *Russ. Chem. Rev.*, 2003, **72**, 311-325.

37 C. G. Wu and M. G. Kanatzidis, *Mater. Res. Soc. Symp. Proc.*, 1991, **210**, 429-442.

38 S. Passerini, D. Chang, X. Chu, D. Ba Le and W. Smyrl, *Chem. Mater.,* 1995, **7**, 780-785.

39 A. Marschilok, A. Subramanian, K. Takeuchi and E. Takeuchi, *Phys.Chem.Chem.Phys.,* 2011, **13**, 18047-18054.

40 A. C. R. Ditte, *Acad. Sci. Paris,* 1885, **101**, 698.

41 J. Livage, *Chem. Mater.,* 1991, **3**, 578-593.

42 W. Biltz, *Ber. Dtsch. Chem. Ges,* 1904, **37**, 1098.

43 G. Z. Wegelin, *Chem. Ind. Kolloide,* 1912, **11**, 25.

44 W. Prandtl and L. Z. Hess, *Anorg. Allg. Chem,* 1913, **103**.

45 W. Ostermann, *Wiss. Ind. Hamburg,* 1922, **1**, 17.

46 E. Z. Muller, *Chem. Ind. Kolloide,* 1911, **8**, 302.

47 N. Gharbi, C. RKha, D. Ballutaud, M. Michaud, J. Livage, J. P. Audiere and G. J. Schiffmacher, *J. Non Cryst. Solids,* 1981, **46**.

48 N. Gharbi, C. Sanchez, J. Livage, J. Lemerle, L. Nejem and J. Lefebvre, *J. Inorg. Chem.,* 1982, **21**, 2758.

49 M. Henry, J. P. Jolivet and J. Livage, *J. Struct. Bonding,* in press 1991.

50 V. Petkov, P. N. Trikalitis, E. S. Bozin, S. J. L. Billinge, T. Vogt and M. G. Kanatzidis, *J. Am. Chem. Soc.,* 2002, **124**, 10157-10162.

51 Y. Takeda, K. Nakahara, M. Nishijima, N. Imanishi, O. Yamamoto, M. Takano and R. Kanno, *Mater. Res. Bull.,* 1994, **29**, 659-666.

52 Y. Takenda, J. Akagi, A. Edagawa, M. Inagaki and S. Naka, *Mater. Res. Bull.,* 1980, **15**, 1167-1172.

53 S. Kikkawa, H. Ohkura and M. Koizumi, *Mater. Chem. Phys.,* 1987, **18**, 375-380.

54 S. Uchida, T. Sato and A. Okuwaki, *J. Mater. Sci.,* 1995, **14**, 633-634.

55 S. Uchida, H. Kashiwagi, T. Sato and A. Okuwaki, *J. Mater. Sci.,* 1996, **31**, 3827-3830.

56 D. E. Fenton, J. M. Parker and P. V. Wright, *Polymer,* 1973, **14**, 589-589.

57 W. Xu, J. Belieres and A. Angell, *Chem. Mater.,* 2001, **13**, 575-580.

58 H. R. Allcock, S. J. M. O'Connor, D. L. Olmeijer, M. E. Napierala and C. G. Cameron, *Macromolecules,* 1996, **29**, 7544-7552.

59 K. M. Abraham, H. S. Choe and D. M. Pasquariello, *Electrochim. Acta,* 1998, **43**, 2399-2412.

60 D. Wilms, M. Schömer, F. Wurm, M. I. Hermanns, C. J. Kirkpatrick and H. Frey, *Macromol. Rapid Commun.*, 2010, **31**, 1811.

61 S. Lee, M. SchoÌˆmer, H. Peng, K. A. Page, D. Wilms, H. Frey, C. L. Soles and D. Y. Yoon, *Chem. Mater.*, 2011, **23**, 2685-2688.

62 M. Forsyth, A. L. Tipton, D. F. Shriver, M. A. Ratner and D. R. MacFarlane, *Solid State Ionics,* 1997, **99**, 257.

63 K. Xu, T. Zhou, Z. H. Deng and G. X. Wan, *Chin. J. Polym. Sci.,* 1992, **10**, 223.

64 de Grotthuss, C. J. T., *Ann. Chim.*, 1806, **58**, 54.

65 W. H. Meyer, *Adv Mater,* 1998, **10**, 439-448.

66 C. V. Nicholas, D. J. Wilson, C. Booth and J. R. M. Giles, *Brit. Polym. J.,* 1988, **20**, 289-292.

67 D. Gallant, Master's Thesis, University of Prince Edward Island, 2002.

68 R. Bissessur, D. Gallant and R. Brüning, *Mater. Chem. Phys.*, 2003, **82**, 316-320.

69 R. Bissessur and S. F. Scully, *Solid State Ionics,* 2007, **178**, 877-882.

70 S. F. Scully and R. Bissessur, *Appl. Clay. Sci.,* 2010, **47**, 444-447.

71 R. Bissessur and H. Xu, *Mater. Chem. Phys.*, 2009, **117**, 335-337.

72 R. Bissessur and D. Schipper, *Mater Lett,* 2008, **62**, 1638-1641.

73 J. L. Bennett, A. A. Dembek, H. R. Allcock, B. J. Heyen and D. F. Shriver, *Chem. Mater.*, 1989, **1**, 14-16.

74 C. J. Nelson, W. D. Coggio and H. R. Allcock, *Chem. Mater.*, 1991, **3**, 786-787.

75 A. A. Argun, N. J. Ashcraft, M. K. Herring, D. K. Y. Lee, H. R. Allcock and P. T. Hammond, *Chem. Mater.*, 2010, **22**, 226-232.

76 C. H. Chen, B. Meester, Put,Paul J. J. M. van der and J. Schoonman, *Chem. Vap. Deposition,* 1998, **4**, 11-15.

77 K. M. Abraham and M. Alamgir, *Chem. Mater.*, 1991, **3**, 339-348.

78 S. F. Scully, R. Bissessur, K. W. MacLean and D. C. Dahn, *Solid State Ionics,* 2009, **180**, 216-221.

79 U. Schwertmann and R. M. Cornell, *Iron oxides in the laboratory :preparation and characterization*, VCH, New York, 1991.

80 I. Bruker AXS, *Diffrac Plus TOPAS User's Manual Version 2.1*, 2003.

81 J. Keeler, *Understanding NMR spectroscopy*, Wiley, Chichester, England; Hoboken, NJ, 2005.

82 B. S. Furniss, A. J. Hannaford, P. W. G. Smith and A. R. Tatchell, in , *Vogel's Textbook of Practical Organic Chemistry,* ed. Longman, Edinburgh Gate, England, 5th edn., 1996.

83 B. Wunderlich, *Thermal Analysis of Polymeric Materials*, Springer-Verlag Berlin Heidelberg, Berlin, Heidelberg, 2005.

84 D. A. Skoog, F. J. Holler and S. R. Crouch, *Principles of Instrumental Analysis*, David Harris, Canada, 2007.

85 K. P. Severin, *Energy Dispersive Spectrometry of Common Rocking Forming Minerals.*, Kluwer Academic, 2004.

86 J. R. Macdonald, http://www.jrossmacdonald.com/levminfo.html, **2011**.

87 P. M. Blonsky, D. F. Shriver, P. Austin and H. R. Allcock, *J. Am. Chem. Soc.,* 1984, **106**, 6854-6855.

88 H. R. Allcock, P. E. Austin, T. X. Neenan, J. T. Sisko, P. M. Blonsky and D. F. Shriver, *Macromolecules,* 1986, **19**, 1508-1512.

89 E. M. Guerra, K. J. Ciuffi and H. P. Oliveira, *J. Solid State Chem.,* 2006, **179**, 3814-3823.

90 G. M. Kloster, J. A. Thomas, P. W. Brazis, C. R. Kannewurf and D. F. Shriver, *Chem. Mater.,* 1996, **8**, 2418-2420.

91 M. G. Kanatzidis, Y. J. Liu, D. C. DeGroot, J. L. Schindler and C. R. Kannewurf, *Chem. Mater.,* 1991, **3**, 992-994.

92 Y. J. Liu, J. L. Schindler, D. C. DeGroot, C. R. Kannewurf, W. Hirpo and M. G. Kanatzidis, *Chem. Mater.,* 1996, **8**, 525-534.

93 E. Ruiz-Hitzky, P. Aranda and B. Casal, *J. Mater. Chem.* , 1992, **2**, 581-582.

94 S. De, A. Dey and S. K. De, *Solid State Commun.,* 2006, **137**, 662-667.

95 R. Bissessur, D. Gallant and R. Brüning, *J. Mater. Sci. Lett.,* 2003, **22**, 429.

96 F. J. Anaissi, G. J. Demets, E. B. Alvarez, M. J. Politi and H. E. Toma, *Electrochim. Acta,* 2001, **47**, 441-450.

97 E. Monyoncho, R. Bissessur, V. Trenton and D. Dahn, *Submitted,* 2011.

98 G. Nazri, D. MacArthur and J. Ogara, *Chem. Mater.,* 1989, **1**, 370-374.

99 S. G. Young, M. Kojima, J. H. Magill and F. T. Lin, *Polymer,* 1992, **33**, 3215-3225.

100 D. Dollimore, in *Encyclopedia of Physical Science and Technology,* ed. ed. Robert A. Meyers, Academic Press, New York, 2001.

101 J. Huang, T. Furukawa and K. Aoto, *J. Phys. Chem. Solids,* 2005, **66**, 388-391.

102 A. Pabst, *Am. Mineral.,* 1930, **15**, 69-73.

103 W. C. Blasdale, *J. Am. Chem. Soc.,* 1923, **45**, 2935-2946.

104 D. A. Skoog, D. M. West and F. J. Holler, *Analytical Chemistry: An Introduction*, Harcourt College Publishers, 2000.